RanBP2-dependent annulate lamellae drive nuclear pore assembly and nuclear expansion

Junyan Lin,[1,2,3,4] Arantxa Agote-Arán,[1,2,3,4,8] Yongrong Liao,[1,2,3,4] Mehdi Cloarec,[1,2,3,4] Leonid Andronov,[1,2,3,4,5,9] Rafael Schoch,[1,2,3,4,5] Paolo Ronchi,[6] Victor Cochard,[7] Rui Zhu,[1,2,3,4,5] Erwan Grandgirard,[1,2,3,4] Xiaotian Liu,[1,2,3,4] Marianne Victoria Lemée,[1,2,3,4] Charlotte Kleiss,[1,2,3,4] Christelle Golzio,[1,2,3,4] Marc Ruff,[1,2,3,4,5] Guillaume Chevreux,[7] Yannick Schwab,[6] Bruno P. Klaholz,[1,2,3,4,5] and Izabela Sumara,[1,2,3,4,*]

[1]Institute of Genetics and Molecular and Cellular Biology (IGBMC), Illkirch, France.
[2]Centre National de la Recherche Scientifique (CNRS), UMR 7104, Strasbourg, France.
[3]Institut National de la Santé et de la Recherche Médicale (INSERM), U964, Strasbourg, France.
[4]Université de Strasbourg, Strasbourg, France.
[5]Centre for Integrative Biology (CBI), Illkirch, France.
[6]European Molecular Biology Laboratory, Electron Microscopy Core Facility, Heidelberg, Germany.
[7]Université Paris Cité, CNRS, Institut Jacques Monod, F-75013 Paris, France.
[8]Current address: Institute of Biochemistry, Department of Biology, ETH Zürich, Zürich, Switzerland.
[9]Current address: Department of Chemistry, Stanford University, Stanford, CA 94305, United States

Contact: * To whom correspondence should be addressed: Izabela Sumara, Institute of Genetics and Molecular and Cellular Biology (IGBMC), Illkirch, France, Phone: +33 3 88 65 35 21, Fax: +33 3 88 65 32 01, Email: sumara@igbmc.fr

Abstract

Nuclear pore complexes (NPCs) enable nucleocytoplasmic transport. While NPCs primarily localize to the nuclear envelope (NE), they also appear in cytoplasmic endoplasmic reticulum (ER) membranes called annulate lamellae (AL). Though discovered in the mid-20th century, AL's function and biogenesis remain unclear. Previously considered exclusive to embryonic and malignant cells, we find AL in somatic mammalian cells. Under normal conditions, AL store pre-assembled NPCs (AL-NPCs) that integrate into the NE during G1 to support nuclear expansion. Upon pathological stimuli, AL transfer to the NE is impaired, leading to their cytoplasmic accumulation. RanBP2 (Nup358) is essential for AL biogenesis, with its phenylalanine-glycine (FG) repeats promoting AL-NPC scaffold oligomerization. ER-associated Climp63 (CKAP4) directs AL-NPCs to ER sheets and the NE. This AL-driven nuclear pore formation is complementary to the canonical routes, constituting a distinct NPC assembly pathway. Our work uncovers the biogenesis mechanism of AL and the nuclear function of this key cellular organelle.

Main

Annulate lamellae (AL) are specialized subdomains within the endoplasmic reticulum (ER), characterized by a variable array of parallel-arranged layers. These assemblies feature a regular distribution of pore structures embedded in the membranes, which closely resemble nuclear pore complexes (AL-NPCs)[1,2]. AL were commonly observed in rapidly developing, differentiating, germ and malignant cells[3–11]. Despite their early discovery by McCullough in 1952[12] and designation by Swift in 1956[13], and subsequent reports describing AL in specific

cell types[3,7,14–21], the universal and evolutionarily conserved function as well as direct biogenesis mechanisms of AL have remained enigmatic.

It could be hypothesized that AL might be utilized by rapidly growing cells to increase the pool of nuclear envelope (NE) NPCs (NE-NPCs) and sustain optimal levels of nucleocytoplasmic transport. This process is vital for normal cellular function, and abnormal expression or localization of nucleoporins (Nups), the building units of NPCs, have been observed in cancer and neurodegenerative disorders[22–25]. However, it is currently unknown if the Nups localization defects, often visualized by low-resolution microscopy techniques as foci or granules, are linked to the presence of AL and if AL regulate nuclear function under physiological conditions.

Here, we address this long-standing knowledge gap and uncover both the universal cellular function of AL and the direct mechanisms underlying their biogenesis. We demonstrate that AL are more abundant than previously recognized and are present in the cytoplasm of various somatic cells under normal physiological conditions. In normally proliferating cells, AL contain pre-assembled AL-NPCs that contribute to nuclear pore assembly and promote nuclear expansion during G1 phase, revealing a distinct NPC assembly pathway complementary to the two previously characterized routes[26]. Under pathological conditions or stress stimuli, this supply is disrupted, leading to the clustering and expansion of AL-NPCs in the cytoplasm. Importantly, the component of the NPC cytoplasmic filaments RanBP2 (also known as Nup358) is required for the formation of AL in normal cells and for their clustering under stress conditions. N-terminal unstructured FG-repeat region of RanBP2 promotes the oligomerization of NPC scaffold components, leading to AL-NPC formation in the cytoplasm. In addition, we identify the ER-resident protein Climp63 (CKAP4) that turns out to ensure the proper localization of AL-NPCs to ER sheets and their integration into the NE. Disrupting these biogenesis mechanisms inhibits AL-NE merging, nuclear pore assembly and nuclear expansion during G1 phase, underscoring the essential role of AL in normal cycling cells.

Results

Single molecule localization microscopy identifies AL in a variety of somatic mammalian cells

To determine whether cytoplasmic Nup foci observed in various stressed cells represent AL, we used cellular models that have linked microtubules (MTs), fragile X-related proteins (FXRPs) (FXR1, FXR2 and FMRP), and ubiquitin-associated protein 2-like (UBAP2L) to aberrant Nup accumulation in the cytoplasm. Indeed, previous findings demonstrated an important role of dynein-mediated MT-based transport as well as chaperoning proteins FXRPs and UBAP2L in the localized assembly of Nups at the NE during interphase[25,27,28]. Nup foci were also seen in the context of a human disease such as fragile-X syndrome (FXS)[25], which is characterized by the absence of FMRP and several other human disorders[14]. Although FXRPs-UBAP2L models do not capture all perturbations that generate cytoplasmic Nup foci, they provide a well-established framework for assessing whether these structures correspond to AL.

As expected, acute (90 minutes) MT depolymerization or deletion of UBAP2L in mCherry-Nup133 knock-in (KI) HeLa cells ((Extended Data Fig. 1a-d) led to the formation of cytoplasmic mCherry-Nup133 foci that also contained Nup62 ((Extended Data Fig. 1e). Correlative light and electron microscopy (CLEM) analysis showed these foci to be localized to parallel-aligned ER membrane structures containing stacked nuclear pore-like complexes, demonstrating that they are AL (Fig. 1a).

To overcome existing limitations in the microscopy analysis of AL, we utilized single molecule localization microscopy[29,30] (SMLM) to generate super-resolution images of the AL foci. In particular, we applied a multi-color variant based on a dichroic image splitter and spectral demixing (splitSMLM)[31]. Via the simultaneous imaging of multiple species of fluorophores, the method enables high-precision observations of the structural organization of NPCs and other

multi-component complexes, reaching a resolution of 20 nm[31]. In contrast to CLEM, this approach is easily applicable under various experimental conditions and can provide more details on the distribution and composition of AL. We confirmed the presence of highly organized cytosolic assemblies containing tightly packed NPC structures, likely corresponding to AL, upon disruption of the FXRPs-UBAP2L pathway (Fig. 1b, Extended Data Fig. 1f-h).

Surprisingly, small AL containing fewer NPCs (on average 1. 65) could be observed in the cytoplasm of wild-type (WT) HeLa cells (Fig. 1b-c, Extended Data Fig. 1i), whereas in cells treated with the MT depolymerizing agent nocodazole AL were larger (average of 13.8 NPCs) (Fig. 1c). Accordingly, when imaged with conventional (diffraction-limited) fluorescence microscopy, AL-foci also appeared smaller for WT HeLa interphase cells (average size 0.090 μm^2) compared to cells with depolymerized MTs (average size 0.213 μm^2) (Extended Data Fig. 2a-b). Similar small cytoplasmic Nup foci were previously postulated to represent AL in normal interphasic cells[32]. We observed a relatively broad distribution range of AL foci sizes (Extended Data Fig. 2a-b) in both WT and nocodazole-treated cells, confirming the reported diversity of AL morphologies and abundance[33]. Hereafter, AL foci that were considered “large” have a size bigger than 0.3 μm^2.

Importantly, small AL could be detected not only in a variety of common cancer cell lines including U2OS, DLD-1, HCT116, but also in the non-transformed cell lines such as RPE-1, FB789 and MRC5 (Extended Data Fig. 3a, 4a). Likewise, small AL structures were observed in normally proliferating human fibroblasts, while large AL were found in FXS patient-derived fibroblasts (Fig. 1d). Finally, AL structures were identified in human iPSCs-derived neurons (Fig. 1e, Extended Data Fig. 3a, 4a), corroborating our findings on the widespread existence of AL in somatic cells. Although AL abundance varied across different cell types (Fig. 1f), AL size consistently increased following nocodazole treatment (Extended Data Fig. 3b, 4b). These results illustrate the strength of splitSMLM as a powerful method to study AL and reveal a widespread existence of small AL in somatic, normally proliferating mammalian cells.

AL cluster and accumulate in the cytoplasm when exposed to pathological stimuli

Small and large AL-NPCs were composed of most of the tested Nups that form different subcomplexes, with the exception of the nuclear basket Nup153 and ELYS, under various analyzed conditions (Fig. 1g, Extended Data Fig. 2c-f). Interestingly, RanBP2 was localized symmetrically on both sides of AL-NPCs (Extended Data Fig. 1f), consistent with previous reports[28,34]. In Drosophila embryos, AL-NPCs contain ELYS, but not Nup153 and Nup62[7] and in Xenopus egg extracts, AL-NPCs did not contain ELYS, while Nup153 and Nup62 were identified[35,36]. These results suggest that the AL consist of pre-assembled NPCs, displaying composition variations across different species. Nucleocytoplasmic transport factors Exportin-1, Importin β, and Ras-related nuclear protein (Ran) likewise localized to AL foci (Extended Data Fig. 5a), as previously reported[16], suggesting that they may be involved in AL-mediated NPC assembly, analogous to the established roles of these factors in NPC assembly pathways[10,36]. NE-resident proteins SUN1 and SUN2, but not Lamin A, Lamin B1, Nesprin, Emerin, and Lap2b, co-localized with AL foci (Extended Data Fig. 5b).

Since AL exist in various sizes and acute MT disruption lead to large AL, we studied their possible dynamic nature. Spinning disk confocal live video microscopy of WT mEGFP-Nup107 HeLa cells, synchronized in interphase, revealed a progressive increase in size and cytoplasmic clustering of AL foci over time following MT depolymerization (Extended Data Fig. 5c and Supplementary Video 1). Similar clustering events were observed upon depletion of FXR1 or in UBAP2L knockout (KO) cells (Extended Data Fig. 5d, e). These results demonstrate that small AL present in normal cells form large AL and accumulate in the cytoplasm when exposed to specific stimuli or in pathological states such as FXS (Fig. 1d).

AL are highly dynamic and can fuse with the NE during G1 under normal conditions

Existence of small AL in normal cells prompted us to analyze their physiological role in normally proliferating cells and to address the question why pathological stimuli, such as MT

disruption, lead to cytoplasmic accumulation of AL. While the conserved role of AL remains unclear, early studies in Drosophila embryos demonstrated that AL integrate into the NE to supply additional membranes and NPCs to support rapid nuclear growth, representing the first indication of the functional role of AL in the context of development[7]. To determine whether the more widespread, herein described small AL serve a similar role in non-stressed somatic cells, we first examined the abundance of AL structures during different cell cycle stages. Analysis of phosphorylated retinoblastoma (p-Rb) (G1/S phase transition marker) and cyclin B (G2 marker) revealed that small AL foci are present throughout interphase, but predominantly in the G1 and S phases (Fig. 2a, b, Extended Data Fig. 6a-d). Large AL foci induced by acute MT disruption followed the same cell cycle distribution tendency (Extended Data Fig. 6e-j). It is therefore possible that nuclear growth during the G1 phase of somatic cells is supported by AL, which primarily exist during G1 (Fig. 2a, b, Extended Data Fig. 6a-d) and which could contribute to the incorporation of new NPCs into the NE.

A quantitative analysis of fixed cells estimated that AL-NPCs within the cytoplasmic AL account for approximately 3% of total nuclear NPCs, increasing to 10% following microtubule depolymerization (Fig. 2c), potentially challenging this hypothesis. However, a simple static comparison of the NPC numbers in two compartments cannot accurately determine the contribution of AL-NPC to the NE. A more time-resolved analysis of the putative dynamic nature of AL structures is required.

For this reason, we used super-resolution live-cell imaging with short time intervals between the acquisition points. We found that AL foci are highly dynamic under physiological conditions, undergoing frequent fusion and fission events (Fig. 2e, Supplementary Video 2, 3), unlike the continuous fusion observed upon microtubule depolymerization (Extended Data Fig. 5c and Supplementary Video 1). Notably, small AL foci fused more rapidly with the NE than large AL (33 and 192 seconds, respectively), and a subset of small AL originated through the fragmentation of large AL and subsequently fused with the NE (81 seconds) (Fig. 2d, e, and Supplementary Video 4). After contacting the NE, AL occasionally undergo multiple cycles of detachment and reattachment before ultimately fusing completely with the NE (Fig. 2d, e, and Supplementary Video 5).

In unstressed cells, each small AL-foci contains an average of 1.65 AL-NPCs (Fig. 1c). Given the observed net AL-NPC fusion frequency with the NE (14 events per 15 minutes) (Fig. 2d), we estimate that approximately 924 AL-NPCs are incorporated into the NE during single G1 phase of the cell cycle (10 hours). Considering that the total number of nuclear pores in HeLa cells accounts for 2000 to 4000[37], the contribution of AL may in fact be substantial, accounting for estimated 22-45% of total nuclear NPCs.

To provide additional evidence for the AL-dependent nuclear delivery of NPCs, we generated photoconvertible mEos2-Nup133 knock-in HeLa cells (Extended Data Fig. 6k-m). The mEos2 is a green-to-red photoconvertible fluorescent protein, although its green fluorescent state lacks sufficient photostability for long-term imaging[38], conversion of mEos2-Nup133 at the NE from green to red fluorescence at a defined interphase time point revealed no detectable diffusion of red signal from the NE into the cytoplasm (Extended Data Fig. 6n, and Supplementary Video 6). Interestingly, photoconversion of cytoplasmic AL-Nup mEos2-Nup133 foci resulted in progressive accumulation of a weak but detectable red signal at the NE (Fig.2f, g, and Supplementary Video 7), indicating that AL-NPCs can be incorporated into the nucleus. The weak nuclear signal can be likely due to progressive photobleaching of the fluorescence signal in the course of the experiment and dynamic remodeling of AL foci, which flattened and dispersed as a rim around the nuclei after migration towards NE (Fig. 2f). Future development of photoconvertible tags with improved long-term stability and brightness are required to investigate dynamics of NE incorporation events of AL in live cells in more detail. Nevertheless, taken together our data show that AL structures observed in normally proliferating cells can attach to the NE during G1.

AL-NPC insertion into the NE through NE-ER contacts supports nuclear expansion and pore formation

To provide morphological evidence for AL incorporation into the NE, we next used splitSMLM to examine the structural organization and composition of AL-NPCs. This analysis visualized symmetric AL-NPCs in the proximity of or directly attached to the NE containing asymmetric NE-NPCs in WT interphase cells (Fig. 3a panels 1-2). AL-NPCs fusion events into the NE were observed where symmetric AL-NPCs were positioned laterally onto the NE (Fig. 3a panels 2-4). Some fusion events were accompanied by the formation of lateral NE openings containing both AL-NPCs and NE-NPCs next to each other (Fig. 3a panels 5-6).

Analysis of nuclear lamina components Lamin A and B1 by splitSMLM revealed that despite the presence of these NE incisions, the underlying nuclear membrane scaffold remained intact (Fig. 3b). Importantly, the analysis of the ER marker PDI, confirmed that the sites of AL-NPC insertion within these NE openings precisely colocalized with the ER and ER-NE contact sites (Fig. 3c). Thus, the splitSMLM analysis confirms the observed AL structures in normal cells as specialized sub-compartments of the ER, which is known to be continuous with the outer NE and contribute to its formation[39]. These observations are also in agreement with a previously proposed model suggesting "*en bloc*" insertion of AL into the NE and remodeling of AL-NPCs by GTPase Ran to become asymmetric functional NPC structures in fly embryos[7,10,34], demonstrating evolutionary conservation of this process. Although 20 nm resolution images from splitSMLM analysis strongly suggest insertion of intact AL into NE, at this point we cannot formally exclude the possibility that AL-NPCs undergo local disassembly or that AL act solely as donors of NPC subcomplexes prior to their NE insertion.

Importantly, spinning disk confocal live video microscopy of the ER marker mScarlet-ER confirmed that AL foci move along the ER to merge with the NE in WT interphase cells (Fig. 3d, and Supplementary Video 8). MT depolymerization is predicted to modulate ER dynamics[40], damaging reticulated ER tubules and leading to vesiculation and thickening of cisternal sheets (Extended Data Fig. 7a), which could explain the inhibition of AL foci transfer to the NE and their clustering (Fig. 3d, Extended Data Fig. 5c and Supplementary Video 9). Interestingly, AL-NPCs were also often localized near microtubules (Extended Data Fig. 7b). Live-cell imaging further revealed a consistent spatial association between AL and the microtubule network (Supplementary Video 10), suggesting that they may utilize MT-ER interactions to merge with the NE and to increase the pool of NE-NPCs. Our results indicate that MT depolymerization in somatic cells disrupts ER dynamics, thereby impairing the transfer of AL-NPCs to the NE, resulting in their cytoplasmic accumulation. However, we cannot exclude the possibility that the transport of soluble Nups along microtubules also contributes to AL-NPC assembly. In support of this, studies in *Drosophila* oocytes have shown that microtubules mediate the delivery of distinct Nup condensates to AL-NPC assembly sites a process essential for efficient AL-NPC formation[10].

Since acute MT depolymerization inhibited AL-NPC transfer to the NE, we set out to analyze the physiological consequences of this inhibition. The density of NE-NPCs (Fig. 3e, f) and the level of Nups at NE (Extended Data Fig. 7c, d) decreased upon acute nocodazole treatment. The short treatment excluded any possible indirect effects of nocodazole on mitotic progression. Strikingly, when cells are arrested in the G1/S phase, the nucleus continues to grow beyond its normal size, and acute MT depolymerization inhibits nuclear growth in G1/S-arrested WT cells (Fig. 3g-j). Nuclear expansion is sustained by a constant supply of many proteins and lipids from the ER to the NE[41], a process which could also be disrupted by MT depolymerization. The insertion of AL-NPCs may support nuclear expansion by potentiating nucleocytoplasmic transport rates, or the supply of lipids and proteins required for NE expansion may occur simultaneously with AL insertion into the NE. Taken together, AL are more widespread than previously anticipated and exist in WT somatic cells. AL act to supply a relatively large pool of AL-NPCs (estimated 924) to the NE, thereby promoting the nuclear expansion specifically during G1 phase of the cell cycle. AL are inserted into the NE at the ER-NE junctions through ER dynamics, and this process requires an intact microtubule network.

These findings not only establish AL as functional determinants of nuclear architecture during normal mammalian cell proliferation but also indicate existence of an additional specialized pathway for NPC assembly during normal cell cycle progression.

RanBP2 is required for the clustering of small AL into large AL under stress conditions but does not regulate protein levels of Nups

Having demonstrated a cellular function of AL in normally growing cells, we next aimed to uncover the mechanisms driving AL biogenesis. The component of NPC cytoplasmic filaments RanBP2 (also known as Nup358) has been shown to localize to AL structures and it has been proposed to regulate a Nup condensate fusion mechanism supporting AL biogenesis during Drosophila oogenesis[10]. However, direct evidence for RanBP2's role in AL formation is missing. It is also unknown if the role of RanBP2 is conserved in somatic cells and in other species, and what the molecular basis for possible RanBP2 function on AL is. RanBP2 was required for the formation of large AL foci induced by MT depolymerization (Fig. 4a-c, Extended Data Fig. 7e-l) and by inactivation of FXRPs-UBAP2L-dynein pathway in several human cell lines tested (Extended Data Fig. 7m-r). Another component of NPC cytoplasmic filaments, Nup214, was not required for the formation of large AL foci (Extended Data Fig. 8a-c). Higher eukaryotes utilize two NE-NPC assembly pathways, each associated with different cell cycle stages: the postmitotic and the interphase pathway[26]. We found that downregulation of ELYS (required for postmitotic NE-NPC assembly), or Nup153 or POM121 (driving interphase NE-NPC assembly) did not inhibit AL foci formation when induced by acute nocodazole treatment Extended Data Fig. 8a-f). In contrast, defects in NE-NPC biogenesis were reported to induce AL[24] and as expected, downregulation of ELYS or Nup153 led to the formation of large AL foci in untreated cells (Extended Data Fig. 8a, d, g). Downregulation of RanBP2 strongly inhibited the formation of large AL foci induced by Nup153 or ELYS depletion (Fig. 4d-i), suggesting its universal and widespread role in AL clustering.

Is RanBP2 also required for the maintenance of the AL structures? Downregulation (Extended Data Fig. 9a-f) or auxin-inducible depletion (Extended Data Fig. 9g-k) of RanBP2 [42] after nocodazole treatment severely decreased the number of large AL foci and their clustering observed upon MT depolymerization. Thus, RanBP2 is required for the formation and the maintenance of large AL. This process is likely to be independent of reported NPC degradation mechanisms involving autophagy[43,44], since RanBP2 downregulation inhibited large AL foci formation also in the presence of lysosomal inhibitors (Extended Data Fig. 10a-h).

Previous studies have shown that RanBP2 knockdown reduces translation of reporter constructs[45], whereas we show that deletion or downregulation of RanBP2 did not alter the protein levels of multiple Nups across various cell lines (Extended Data Fig. 10i-k). Notably, the use of auxin-inducible RanBP2 depletion minimizes the confounding effects of chronic translational defects (Extended Data Fig. 10k). Therefore, the observed reduction in AL is unlikely to result from global translational regulation of Nups by RanBP2 under these conditions. The RanBP2 function on AL could also not be explained by possible effects on levels of FXR1 and UBAP2L, the factors driving spatial assembly of Nups during early interphase[28], as they were not affected by auxin-inducible deletion of RanBP2 in DLD-1 (Extended Data Fig. 10l) and in HTC116 cells (Extended Data Fig. 10m). Thus, RanBP2 is required for the clustering of small AL into large AL and for AL maintenance but does not regulate protein levels of Nups or Nup-interacting factors.

RanBP2 is required for biogenesis of small AL and their nuclear function during G1 in non-stressed cells

Is RanBP2 also required for the formation and function of small AL that we identified under normal growing conditions? The splitSMLM analysis revealed a relatively broad distribution of the number of NPC complexes in a single AL-NPC structure (Fig. 4j-l) and as expected, acute MT depolymerization increased both the number of individual AL-NPCs in single AL foci as well as the total number of AL-NPCs per cell relative to WT cells (Fig. 4j-l). Importantly,

RanBP2 was required for the formation of individual AL-NPCs, as well as their clustering both in WT and in nocodazole-treated cells (Fig. 4j-l). AL-NPCs were reported to lack nuclear basket components[7,35,36], whereas RanBP2 appears to be localized symmetrically on both sides of AL-NPCs[28] (Fig. 3a, b, Extended Data Fig.1f) and RanBP2 can oligomerize to form multimers[45], providing a possible explanation for its ability to cluster individual AL-NPCs. In accordance with its role in AL-NPC biogenesis, RanBP2 was required for the formation of small AL foci in WT cells from G1 to S-phase but not in G2 stage (Fig. 4m, Extended Data Fig. 11a) and RanBP2 downregulation by siRNA decreased levels of Nups at the NE (Extended Data Fig. 11b, c). Small AL foci and the levels of Nups at the NE during interphase also decreased using auxin-inducible deletion of RanBP2 (Extended Data Fig. 11d-h), suggesting that RanBP2-mediated formation of small AL is a prerequisite for their merging with NE and increasing the pool of NE-NPCs. Short-term deletion of RanBP2 reduced levels of several Nups in isolated nuclear fractions and increased their abundance in the cytoplasm in DLD-1 (Fig. 4n) and HTC116 cells (Fig. 4o), consistent with the idea that RanBP2 does not regulate the total protein levels of Nups (Extended Data Fig. 10i-k) but their localization to the NE. Indeed, RanBP2 deletion resulted in reduced NE-NPC density (Fig. 4p, 4r).

Can RanBP2 also contribute to the nuclear pore function? We analyzed the gradient of endogenous Ran, a guanine nucleotide triphosphatase, as previously reported[28,46], owing to the fact that Ran protein is actively imported to the nucleus with the help of transport factors where it then detaches from its cargo and is swiftly exported to begin the cycle again. Downregulation of RanBP2 (Extended Data Fig. 12a, 12b) increased the nuclear-cytoplasmic (N/C) ratio of Ran, suggesting defects in the nuclear export rate of Ran protein. Acute RanBP2 depletion likewise increased the nuclear-to-cytoplasmic (N/C) ratio of Ran and these defects were stronger in G1 cells than in G2 cells (Extended Data Fig. 12c,12e), indicating that AL- and RanBP2-dependent NPC assembly is particularly important in early interphase. Defects generated by 24-hour RanBP2 depletion were stronger in G2 cells than in G1 cells, reflecting the cumulative effect of defects (Extended Data Fig. 12d,12e). Importantly, in wild-type cells the N/C ratio of Ran was lower in G2 than in G1, suggesting an increase in the nuclear export rate of Ran as the cell cycle progresses and a hypothesis that nucleocytoplasmic transport properties change as the nucleus grows. The use of the light-inducible nuclear export system (LEXY)[47], confirmed the export defects upon acute depletion of RanBP2 (Extended Data Fig. 12f,12g).

Our data in normally proliferating cells demonstrated a role for AL in supplying the NE-NPC pool, thereby supporting the nuclear expansion during early interphase. Since RanBP2 was required for AL-NPC formation in WT cells, we next analyzed the role of RanBP2 in nuclear function. Importantly, short-term depletion of RanBP2 was sufficient to reduce nuclear size (Fig. 4q, 4s), expanding our observations in nocodazole-treated cells (Fig. 3g-i). We conclude that RanBP2-mediated AL-NPC assembly can preserve nuclear pore density as well as nuclear growth during interphase, confirming the critical role of cytosolic NPCs in the nuclear function. Collectively, RanBP2 plays direct and widespread roles in AL, being essential for the biogenesis of single AL-NPCs, their clustering and AL maintenance in multiple stressed and normally proliferating somatic cells.

FG repeats within the N-terminal domain of RanBP2 are required for the assembly of AL and their nuclear function

Next, we set out to study the precise molecular mechanisms of RanBP2-mediated AL biogenesis. First, to understand if the function of RanBP2 on AL is specific and which functional domains of this large protein (Fig. 5a) are required for AL formation, we performed rescue experiments using RanBP2 fragments. The full-length (FL) (aa 1-3224) and the N-terminal (NT) fragment of RanBP2 (aa 1-1171) efficiently reversed the inhibition of nocodazole-induced large AL foci observed upon downregulation of RanBP2, and the phenylalanine-glycine (FG) repeat region (832-1171) was essential for RanBP2 AL clustering function (Fig. 5a-e). The effects of auxin-inducible deletion of RanBP2 on AL formation could also be efficiently rescued

364 by NT fragment of RanBP2 (aa 1-1171) but not by the version missing the FG repeat region
365 (1-832) (Extended Data Fig. 13a-e).
366 Importantly, full-length RanBP2 with a deletion of the FG region, which is not expected to affect
367 other cellular functions of RanBP2, failed to restore large AL foci in RanBP2-depleted cells by
368 either auxin-inducible degron (Fig. 5f-i) or RanBP2-specific siRNAs (Extended Data Fig. 13f-
369 i), confirming an essential role of RanBP2 FG repeats in AL accumulation. In contrast, mutation
370 of the LIQIML motif, which is important for RanBP2 targeting to the NE and its function on NE-
371 NPCs assembly[45], inhibited efficient NE localization of full-length RanBP2 leading to its nuclear
372 and cytoplasmic localization, as expected, but successfully rescued AL defects observed
373 under both RanBP2-deleting experimental approaches (Fig. 5f-l, Extended Data Fig. 13f-i).
374 These results further support the conclusion that FG region of RanBP2 regulates AL formation
375 independently of other known cellular functions of this protein and identify a mutant form of
376 RanBP2 which can separate its functions at the NE and on AL.
377 These findings enabled us to further assess the role of AL in nuclear expansion in untreated
378 WT cells. Full-length WT and RanBP2 LIQIML mutant, but not full-length RanBP2 without FG
379 region, successfully rescued the nuclear expansion defect caused by RanBP2 depletion by
380 auxin-inducible degron or siRNA (Extended Data Fig. 13j-l, Fig. 5j-k). Taken together, these
381 results demonstrate the important and specific role of the FG region of RanBP2 in AL formation
382 and AL-driven nuclear function.
383
384 **RanBP2 promotes oligomerization and assembly of AL-NPCs scaffold components**
385 **through its N-terminal domain**
386 To corroborate the role of the NT region of RanBP2, we set out to study its molecular
387 interactions relevant for AL biology. Ectopic expression of NT RanBP2 (aa 1-1171) (Extended
388 Data Fig. 14a-d) but not of FL Nup85 or FL Nup133 (Extended Data Fig. 14e, 14f), induced
389 AL foci where multiple Nups, with the exception of ELYS and Nup153 (Extended Data Fig.
390 14c), could co-localize, relative to controls. CLEM analysis (Fig. 6a) and splitSMLM (Fig. 6b)
391 confirmed that these foci represent AL. Ectopic expression of NT RanBP2 increased the
392 number of individual AL-NPCs per cell and the size of AL (Fig. 6b-d). We conclude that
393 elevated levels of NT RanBP2 fragment can induce AL under normal growth conditions.
394 Since RanBP2 was required for the assembly of small AL foci and individual AL-NPCs in the
395 cytoplasm (Fig. 4j-l), we next asked how RanBP2 NT regulates this crucial function at the
396 molecular level. Interestingly, structural analysis of the NPC demonstrated that N-termini of
397 five RanBP2 and one Nup93 molecules bind to the overlapping region of two Y complexes
398 (also named Nup107-Nup160 complexes) in the scaffold's outer ring[45], and deletion of
399 RanBP2 resulted in an outer ring that lacked Y complexes on the cytoplasmic side[48]. To test
400 if RanBP2 can promote the oligomerization state of scaffold components of AL-NPCs in a
401 similar fashion, we analyzed separated cytoplasmic and nuclear cellular fractions by gel-
402 filtration chromatography (Extended Data Fig. 14g). Deletion of RanBP2 inhibited the
403 formation of oligomers of Y complexes and Nup96-labelled scaffold in the cytoplasm (Fig. 6f)
404 but not in the nucleus (Extended Data Fig. 14h).
405 Intrinsically disordered FG repeats have been reported to stabilize subcomplexes within NE-
406 NPC[49], therefore we examined if similar interactions between the RanBP2 NT fragment (aa 1-
407 1171) and other Nups could play a role in AL-NPC assembly. The outer ring of the NPC is
408 mainly composed of the evolutionarily conserved Y complex. We found that the N-terminal
409 fragment of RanBP2 could bind the Y complex, as well as Nup205 and Nup93 (Fig. 6e), which
410 belong to the inner ring and have recently been reported to also reside on the cytoplasmic face
411 of NPCs[45]. The interaction between these Nups with NT RanBP2 was dependent on the FG
412 repeat domain (Fig. 6e), suggesting that it facilitates the assembly of single AL-NPCs. Deletion
413 of RanBP2 did not affect the formation of the Y complex (Extended Data Fig. 15a) both in the
414 cytoplasm and in the nucleus (Extended Data Fig. 15b), but it restricted the binding of the Y
415 complex to Nup93 (Fig. 6g, Extended Data Fig. 15c) specifically in the cytoplasm (Fig. 15c).
416 This suggests that RanBP2 may stabilize interactions between the outer and inner rings of AL-

417 NPCs in agreement with reported high-resolution NPC structures[45], and thereby promote AL-
418 NPC assembly in the cytoplasm. Indeed, Nup93 was required for the formation of large AL-
419 foci (Extended Data Fig. 15d-f), and the increase of AL foci abundance by ectopic expression
420 of NT RanBP2 was dependent on Nup93 (Extended Data Fig. 15g, 15h, 15j, 15k ,15m).
421 Downregulation of Nup93 also led to the formation of Nup62-positive nuclear foci (Extended
422 Data Fig. 15j), which did not co-localize with other Nups, suggesting that they may not
423 represent AL. Co-localization of NT RanBP2 with Nup133 (Extended Data Fig. 15i) and Nup62
424 (Extended Data Fig. 15l) in the cytoplasm required Nup93, in line with reports showing that
425 Nup93 helps to connect the central channel to the NPC scaffold[50]. We conclude that the
426 function of the NT part of RanBP2 on AL-NPCs can be attributed to its interactions with Nup93
427 and its ability to stabilize connections between NPC subcomplexes. Taken together, these
428 results identify the precise molecular mechanism of AL-NPC formation and show that RanBP2
429 directly drives the interaction between the Y complex and Nup93, as well as the
430 oligomerization of scaffold AL-NPC components.
431
432 **Climp63 facilitates the localization of AL-NPCs to ER sheets and their integration with**
433 **the NE**
434 Our findings on the molecular mechanism of AL-NPC assembly and the direct role of RanBP2
435 in this process create a unique opportunity to identify additional factors involved in AL biology,
436 in particular those facilitating AL-NPCs insertion into the ER membranes. Since the NT
437 RanBP2 fragment can induce the formation of AL (Fig. 6a-d), we analyzed the proteins
438 interacting with HA-tagged NT RanBP2 (aa 1-1171) compared to HA-tag only, using liquid
439 chromatography-mass spectrometry (LC-MS). Of total 97 proteins specifically bound to NT
440 RanBP2, 20 were associated with the NPC, as expected. Additionally, numerous ER-
441 associated proteins were also identified Extended Data Fig. 16a-c). Among them, Climp63
442 (also known as CKAP4), a type II membrane protein, emerged as an interesting candidate for
443 the regulation of AL because it has been implicated in maintaining ER morphology, being
444 important for the biogenesis of ER sheets and regulation of their width, and for coordinating
445 the formation and dynamics of ER nanoholes[51,52]. Moreover, its N-terminus binds to MTs,
446 linking the ER to the cytoskeleton[53]. Thus, it is particularly interesting that we indeed detected
447 an interaction between the HA-tagged NT RanBP2 and endogenous RanBP2 and Climp63
448 (Fig. 6h-i, Extended Data Fig. 17a). Since stringent cell lysis conditions were used for these
449 experiments and several other ER-resident proteins were not found to interact with RanBP2,
450 this argues against nonspecific co-purification of bulk ER membranes and supports a more
451 specific association between RanBP2 and Climp63. In contrast to the interaction of RanBP2
452 with Nups (Fig. 6e), our current data do not allow us to determine whether the association of
453 Climp63 depends on the FG-rich region of the NT part of RanBP2, and mapping the direct
454 Climp63-RanBP2 binding sites therefore represents an important avenue for future work.
455 In interphase cells, RanBP2-labeled AL foci preferentially localized to ER regions positive for
456 Climp63 (Extended Data Fig. 17e-g, 17i, j), residing closer to the nucleus relative to the entire
457 ER network (Extended Data Fig. 17h). These Climp63-positive regions likely correspond to
458 ER sheets, in line with published findings[52]. This suggests that, under normal growth
459 conditions, AL may primarily reside within sheet-like regions of the ER rather than in its tubules.
460 The tendency of the ER sheets to localize close to the nucleus may facilitate AL merging with
461 the NE under physiological conditions.
462 Downregulation of Climp63 (Fig. 6j-o) led to the dispersion of ER sheets throughout the
463 cytoplasm (Fig. 6j), in accordance with previous reports[52], and strongly altered the morphology
464 and distribution of AL foci. AL foci increased in both abundance (Fig. 6j, 6l) and size (Fig. 6m),
465 relocating to the cell periphery, regions that originally corresponded to ER tubules (Fig. 6j), in
466 Climp63 downregulated cells. Depletion of several ER-shaping and ER-associated proteins
467 including RTN4, ATL1, ATL3, LNPK, KTN1 or P180 did not reproducibly affect AL formation
468 (Extended Data Fig. 17b-d). Instead, their knockdown resulted in highly variable AL
469 phenotypes, likely reflecting general perturbations of ER morphology rather than a specific role

470 in AL biology. Thus, Climp63, and possibly a restricted subset of ER factors, but not ER-
471 associated proteins in general, are specifically involved in the AL pathway.
472 Additionally, the nuclear intensity of RanBP2 was reduced upon Climp63 downregulation (Fig.
473 6n). SplitSMLM analysis confirmed that Nup foci in Climp63 downregulated cells correspond
474 to AL (Fig. 6o). One can speculate that the reported Climp63 ability to connect ER to MTs
475 could explain the observed phenotype and Climp63 absence would inhibit MT-mediated
476 transport of AL towards NE. Alternatively, Climp63-mediated regulation of ER dynamics and
477 nanomorphology could explain these effects. These observations also suggest that RanBP2-
478 mediated biogenesis of AL-NPCs in the cytosol can be separated from their proper localization
479 at ER membranes, a process directly dependent on Climp63 and that in the absence of
480 Climp63, cells attempt to compensate these defects by increasing the formation of AL-NPCs.
481 Irrespective of the underlying mechanisms, which could be a topic for future investigations,
482 downregulation of Climp63 decreased Nup levels at the NE (Fig. 6j, 6n) and inhibited nuclear
483 expansion (Fig. 6p, 6q), suggesting that Climp63-mediated ER dynamics is an important
484 prerequisite for the integration of AL-NPCs into the NE in normal cells. Taken together, our
485 results identify the molecular mechanism of AL biogenesis in normal cells, where RanBP2 is
486 crucial for the formation of AL-NPCs in the cytoplasm and Climp63 acts as a factor targeting
487 AL-NPCs to the proper membrane compartment, the ER sheets. These mechanisms ensure
488 nuclear pore assembly and function as well as nuclear growth specifically during G1 phase of
489 the cell cycle.
490

491 **AL-dependent NPC assembly is additive to canonical nuclear pore assembly pathways**
492 What is the relationship of the AL-dependent nuclear pore assembly to the canonical assembly
493 pathways acting during two stages of the cell cycle?
494 Indeed, the postmitotic and the interphase pathways have been primarily described to drive
495 NPC assembly at the NE[26]. Interestingly, in contrast to RanBP2, downregulation of essential
496 upstream components ELYS (postmitotic pathway) or Nup153 (interphase pathway) did not
497 inhibit AL formation but instead strongly induce them (Extended Data Fig. 8d-f)[24]. Our
498 measurements in G1 cell cycle stage estimated that the contribution of AL to pore assembly
499 is substantial, accounting for 22-45% of total nuclear NPCs, suggesting that somatic cells may
500 utilize an additional assembly pathway governed by RanBP2.
501 To test this hypothesis, we analyzed the complementarity of RanBP2-driven AL pathway with
502 the two canonical NPC assembly pathways. Downregulation of ELYS or Nup153 reduced NE-
503 associated Nup levels and NPC density in the nucleus (Fig. 7a-e) in HeLa cells, as expected.
504 Strikingly, additional knockdown of RanBP2 further exacerbated these effects (Fig. 7a-e). The
505 same results were obtained in DLD-1 cells where RanBP2 was depleted for only 4 hours using
506 auxin-inducible degradation (Fig. 7f-j). These findings suggest that RanBP2-dependent AL do
507 not act redundantly with the classical NPC assembly pathways but instead contribute
508 independently to the biogenesis of a substantial pool of NPCs at the NE. Taken together,
509 mammalian somatic cells may utilize three distinct nuclear pore assembly pathways, in
510 contrast to the two previously described [26,54–56].
511

512 ## Discussion

513 **Annulate lamellae (AL) exist in somatic cells under normal growth conditions**
514 In this study, we demonstrated a universal function and direct biogenesis mechanism of
515 Annulate Lamellae, a mysterious cellular structure known for decades to exist in the
516 cytoplasm[12,13] (Fig. 7k). Using splitSMLM[31], an advanced super-resolution microscopy and
517 spectral demixing method for colocalization and image analysis, we show that AL are more
518 abundant than previously anticipated and exist in the cytoplasm of a variety of somatic cells
519 under physiological conditions. Our analysis provides unique insights into the biogenesis of
520 AL, which is a key cellular organelle involved in the regulation of nuclear function. Compared
521 to healthy state, dysregulation of AL biogenesis occurs in diseased cells, where AL accumulate
522 and cluster in the cytoplasm as exemplified by our data in the fragile-X syndrome patient-

523 derived samples (Fig. 1e). Under physiological conditions during the G1 cell cycle stage, AL
524 merge with the NE and supply it with pre-formed NPCs, a process that is particularly active
525 during periods of rapid nuclear growth (Fig. 7k). Inhibition of AL merging with the NE, either by
526 blocking their MT-based movement (Fig. 3d-f) or by interfering with AL biogenesis through
527 RanBP2 deletion (Fig. 4n-s) or by preventing their Climp63-mediated localization to ER
528 membranes (Fig. 6j-q), reduces the density of nuclear pores and inhibits nuclear expansion
529 during G1. These findings identify a specific physiological situation that drives the use of AL in
530 normal cells, which were not amenable to AL analysis previously.
531 Our data may also explain why, in the past, AL have been commonly observed in rapidly
532 developing, cancerous, or challenged cells, which are likely to depend more crucially on rapid
533 nuclear growth [3–11]. Under these conditions, cells might actively increase their cytoplasmic AL
534 pool by upregulating RanBP2-dependent mechanisms. In addition, our findings show that AL
535 vary widely in size and abundance and are highly dynamic undergoing continuous fusion and
536 fission prior to the merging with the NE (Fig. 2d, 2e). This dynamic behavior may further explain
537 why previous static analyses failed to detect AL in somatic cells. Given variable abundance of
538 AL in different cell types (Fig. 1f), we cannot exclude the possibility that they may rely on the
539 AL pathway to varying degrees.
540
541 **AL-dependent NPC assembly during G1 constitutes a distinct pathway in somatic cells**
542 Blocks of AL structures inserted into the NE have been previously observed in *Drosophila*
543 embryos[7], while our study demonstrates that this process is evolutionarily conserved and
544 operates in somatic cells in general. AL have been also implicated in merging with the NE in
545 postmitotic cells[15], however, in contrast to our work, this phenomenon seemed independent of
546 ER membranes, and rather involved direct interactions with decondensing chromosomes
547 during late anaphase. Time-resolved analysis of AL dynamics allowed us to estimate the net
548 contribution of AL-NPCs to the NE that accounts for more than 900 new pores per one G1
549 phase of the cell cycle, representing a substantial portion (22-45%) of the total present NE-
550 NPCs (Fig. 2d, 2E). Analysis of the NPC assembly kinetic revealed that postmitotic NPC
551 assembly is completed within 15 minutes, rapidly adding around two thousand NPCs, while by
552 contrast, interphase NPC assembly is slower and more sporadic, plateauing after 100 minutes,
553 with unknown NPC assembly rate[57]. In comparison, our AL-NPC insertion data show a
554 continuous rate of 1.5 NPCs per minute throughout entire G1, as supported by the persistent
555 presence of AL foci from early G1 through mid-to-late G1/S (Fig. 2a, 2b) and by
556 photoconversion experiments (Fig. 2f, 2g). Thus, although slower than the postmitotic
557 assembly, AL-NPC insertion occurs at a rate comparable to canonical interphase assembly
558 and represents a kinetically significant and sustained mechanism of NPC addition.
559 Strikingly, AL-driven NPC assembly acts complementarily to the two canonical NPC assembly
560 pathways and the effects on pore density observed upon simultaneous depletion of RanBP2
561 and ELYS (postmitotic pathway) or Nup153 (interphase pathway) are additive (Fig. 7a-j). Thus,
562 RanBP2- and AL-dependent NPC increase occurs through an independent mechanism (Fig.
563 7a-j). Supporting this, our data identify a RanBP2 mutant (ΔFG region mutant) that clearly
564 separates its AL-specific function from its other roles at the NE and in the cytoplasm. Taken
565 together, our study positions the AL-insertion mechanism as a distinct, possibly third NE-NPC
566 biogenesis pathway that operates specifically during interphase and acts complementarily to
567 the two well-described pathways in higher eukaryotes[26,54–56]. In the future, it will be important
568 to understand why downregulation of factors responsible for postmitotic and interphase NPC
569 assembly results in the accumulation of AL and how these defects are linked to the regulation
570 of RanBP2.
571 Our findings on the existence of small AL structures represent an important first step toward
572 future studies aimed at understanding how normal somatic cells acquire pre-assembled AL-
573 NPCs during nuclear growth. During development, the simultaneous insertion of numerous
574 AL-NPCs (arranged within several parallel ER membranes in the cytoplasm) into the nuclear
575 envelope (NE) involves the formation of large NE openings[7], which likely serve to avoid

topological constraints associated with AL insertion. It is unknown if a similar mechanism operates in somatic cells. Studies by Otsuka and Ellenberg[58] indicate that the reforming NE is fenestrated at mitotic exit and largely seals by early G1, however, a small fraction of openings may plausibly persist into G1. Such residual discontinuities could, in principle, serve as entry sites for AL-derived NPCs or for membrane fusion events contributing to NE growth, which should be studied in the future.

Our splitSMLM analysis reveals that small, symmetric AL-NPCs laterally merge with asymmetric NE-NPCs. Some of these fusion events are accompanied by the formation of small NE openings containing ER membranes, with both AL-NPCs and NE-NPCs positioned adjacent to each other, without disrupting the underlying lamina components (Fig. 3a-c). While a recently proposed model suggests that the GTPase Ran remodels AL-NPCs into asymmetric, functional NPCs in fly embryos[34], it will be crucial in future work to define the exact remodeling steps that occur during AL membrane insertion into the NE in somatic cells, ideally using high-resolution ultrastructural approaches. Although our data support the insertion of intact AL structures into the NE, we cannot yet rule out the possibility that AL-NPCs undergo partial disassembly prior to insertion, or that AL act primarily as donors of NPC subcomplexes rather than inserting as complete structures.

Interestingly, the bleb-like AL-NE intermediates observed on the NE by our splitSMLM analysis may resemble NE herniations described in *Saccharomyces cerevisiae* and in human cells carrying mutations in Brl1/6 or TorsinA[59–63]. These factors have been implicated in interphase NPC assembly, possibly through roles in membrane fusion and lipid homeostasis at the NE. Whether Brl1/6 or TorsinA also contribute to AL insertion into the NE and the regulation of AL-NPCs remains an important avenue for future research.

Yet, our work not only demonstrates that small AL are clearly beneficial for cellular homeostasis by preserving nuclear function during G1, but also lays a solid foundation for important future studies on molecular topology of nuclear pore formation to the NE.

The molecular mechanisms of AL biogenesis in somatic cells

In addition to elucidating the universal cellular function of AL during G1, the direct molecular mechanisms of AL formation identified in our study explain how AL-NPCs are made and how they could localize to the proper compartment of the ER (Fig. 7k). We show that RanBP2 is indispensable for the assembly of cytosolic AL-NPCs across cell types and conditions, serving as an assembly platform that specifically regulates the oligomerization of Y complexes within the AL-NPC scaffold. While this process may involve other structurally important Nups, such as Nup93 (Extended Data Fig. 15), the N-terminal region of RanBP2 containing FG repeats is required for AL biogenesis. Intrinsically disordered FG repeats have been shown to stabilize subcomplexes within NE-NPC[49], providing a possible explanation for their function on AL-NPCs. The role of cohesive FG repeats could also help to understand previous observations in fly embryos, where RanBP2 and intact microtubules were implicated in recruiting various condensed precursor Nup particles, predicted to lead to AL biogenesis[10]. Although we occasionally observe cytoplasmic RanBP2 foci under normal conditions (Fig. 3c), we are unable to clearly classify them as membrane-free. Interestingly, our results reveal a spatial association of AL to the microtubule network (Extended Data Fig. 7b) and RanBP2 has previously been reported to stabilize MT bundles and recruit dynein motor protein[64,65]. Whether RanBP2 mediates the interaction between AL and microtubules and if this process involves the formation of Nup condensate particles that facilitate AL assembly in somatic cells, remain important questions for the future. Here, we provide direct evidence for the role of RanBP2 in AL biogenesis and clarify the detailed molecular requirements for AL-NPC formation that is functionally analogous but mechanistically distinct from that described in fly oocytes.

On the membrane side, we identify Climp63 as a key factor localizing AL-NPCs to ER sheets proximal to the nucleus, a process important for their subsequent integration into the NE and nuclear expansion. To our knowledge, this is the first evidence directly linking AL to specific ER substructure so far. By analysing the interaction and function of several other ER factors,

we support the idea that Climp63, and possibly a restricted subset of ER proteins, but not ER-associated factors in general, is specifically involved in the AL pathway. Since Climp63 was shown to ensure not only the formation of ER sheets but also the biogenesis of ER nanoholes[51,52], which were discussed to be similar in size to that of nuclear pores[51], it would be exciting to study the roles of ER dynamics and nanomorphology in AL biogenesis. It would also be important to understand if the reported role of Climp63 in connecting ER to MTs could explain its role in positioning AL in proximity to the NE.

One of the most abundant proteins in the AL proteome belongs to the RGPD family (Extended Data Fig. 16a), which shares significant sequence similarity with the N-terminal domain of RanBP2. Although RGPD proteins are predicted to localize to the Golgi apparatus, they may retain MT-binding capacity[66] and it will be interesting to study this protein family in the context of AL biology. Likewise, a possible role of NE-resident proteins SUN1 and SUN2, which we found to co-localize with AL foci (Extended Data Fig. 5b) and which are components of LINC complexes[67], could be during early steps of NPC interphase assembly[68], which opens possibilities for future investigations.

Undoubtedly, our findings not only clarify the fundamental mechanisms of AL biogenesis but also create an important ground for future investigations aiming to identify AL-specific factors, which could be utilized by pathologically challenged cells such as during malignancy. Indeed, maintaining NPC function is crucial for normal cellular physiology, as disruptions in nucleocytoplasmic transport, mis-localization of Nups, and elevated levels of AL have been observed in various diseased and infected cells[23,25,46,69–74]. The biological principles of AL biology identified by our study may create a basis for future approaches to restore NPC homeostasis in human diseases such as fragile-X syndrome and numerous other neurological and neurodegenerative diseases as well as cancer [14].

Acknowledgements

We thank members of the Sumara, I. and Ricci, R. laboratories for helpful discussions on the manuscript and IGBMC facilities for their help. We are grateful to Valérie Doye, Bernhard Hempoelz and participants of the “Rembo” workshop for stimulating discussions on data interpretation. We are grateful to Arnaud Echard and Anakine Prizins for helpful support on photoconversion experiments and comments on the manuscript. We acknowledge the Virus and Molecular Biology platform of the IGBMC for the lentivirus production. We acknowledge the IGBMC imaging center, member of the national infrastructure France-BioImaging supported by the French National Research Agency (ANR-10-INBS-04).

Lin, J. Liu X. and Liao, Y. were supported by PhD fellowships from the China Scholarship Council (CSC). Agote-Aran, A., was supported by PhD fellowship from the IMCBio graduate school and a fellowship from the “Ligue Nationale Contre le Cancer”. Cloarec M. was supported by PhD fellowship from the doctoral school University of Strasbourg.

Andronov, L., Schoch, R. and Klaholz, B. P. acknowledge support by Institut National du Cancer (INCa) and by the French Infrastructure for Integrated Structural Biology (FRISBI) ANR-10-INSB-05-01, Instruct-ERIC and iNEXT-Discovery. Golzio, C. is a permanent INSERM investigator. Lemée, M.V. is a doctoral fellow supported by EUR IMCBio funds and Fondation de France (WB- 2022-45868). This work was funded by Agence Nationale de la Recherche under the projects (ANR-22-CE12-0011). Research in Sumara, I. laboratory was supported by the grant ANR-10-LABX-0030-INRT, a French State fund managed by the Agence Nationale de la Recherche (ANR) under the frame program Investissements d’Avenir ANR-10-IDEX-0002-02, IGBMC, CNRS, ARC, INCa (PLBIO 2022-082), ANR (AAPG2022, NICE4Nups) and AFM-Telethon.

Author contributions

The role of RanBP2 in human cytosolic NPCs was initially discovered by A.A.A. and confirmed by J.L., and the research plan and the conceptualization of the results were based on

discussions between J.L. and I.S.. J.L. performed most of the experiments and analyzed the data. Y.L. helped with experiments on UBAP2L, L.A. and R.S. helped with splitSMLM analyses, P.R. helped with CLEM, R.Z. helped with gel-filtration chromatography, M.V. L generated the hiPSC derived neurons, E. G. helped with photoconversion experiment, X.L and M.C. helped with FB789 and MRC5 cell lines and M.C. helped with experiments on Climp63. C.K. helped with the reagents and materials. M.R., Y.S., C.G. and B.P.K. helped with the design of the experiments and supervision. I.S. supervised the project and J.L. and I.S. wrote the manuscript with input from all authors.

Competing interest

The authors declare no competing interests.

Additional information

The supplementary materials consist of Supplementary Table 1, Supplementary Videos 1-10 and Extended Data Figures 1-17.

References

1. Kessel, R. G. Annulate lamellae: a last frontier in cellular organelles. *Int Rev Cytol* **133**, 43–120 (1992).
2. Kessel, R. G. The annulate lamellae--from obscurity to spotlight. *Electron Microsc Rev* **2**, 257–348 (1989).
3. Rawe, V. Y., Olmedo, S. B., Nodar, F. N., Ponzio, R. & Sutovsky, P. Abnormal assembly of annulate lamellae and nuclear pore complexes coincides with fertilization arrest at the pronuclear stage of human zygotic development. *Hum Reprod* **18**, 576–582 (2003).
4. Zybina, E. V. & Zybina, T. G. Modifications of nuclear envelope during differentiation and depolyploidization of rat trophoblast cells. *Micron* **39**, 593–606 (2008).
5. Caruso, R. A. *et al.* Modifications of nuclear envelope in tumour cells of human gastric carcinomas: an ultrastructural study. *Anticancer Res* **30**, 699–702 (2010).
6. Gil-Perotín, S. *et al.* Adult neural stem cells from the subventricular zone: a review of the neurosphere assay. *Anat Rec (Hoboken)* **296**, 1435–1452 (2013).
7. Hampoelz, B. *et al.* Pre-assembled Nuclear Pores Insert into the Nuclear Envelope during Early Development. *Cell* **166**, 664–678 (2016).
8. Underwood, J. M., Becker, K. A., Stein, G. S. & Nickerson, J. A. The Ultrastructural Signature of Human Embryonic Stem Cells. *J Cell Biochem* **118**, 764–774 (2017).
9. Grandi, G., Astolfi, G., Chicca, M. & Pezzi, M. Ultrastructural investigations on spermatogenesis and spermatozoan morphology in the endangered Adriatic sturgeon, Acipenser naccarii (Chondrostei, Acipenseriformes). *J Morphol* **279**, 1376–1396 (2018).
10. Hampoelz, B. *et al.* Nuclear Pores Assemble from Nucleoporin Condensates During Oogenesis. *Cell* **179**, 671-686.e17 (2019).
11. Dymek, A. M., Pecio, A. & Piprek, R. P. Diversity of Balbiani body formation in internally and externally fertilizing representatives of Osteoglossiformes (Teleostei: Osteoglossomorpha). *J Morphol* **282**, 1313–1329 (2021).
12. McCulloch, D. Fibrous structures in the ground cytoplasm of the Arbacia egg. *J. Exp. Zool.* **119**, 47–63 (1952).
13. Swift, H. The fine structure of annulate lamellae. *J Biophys Biochem Cytol* **2**, 415–418 (1956).
14. Lin, J. & Sumara, I. Cytoplasmic nucleoporin assemblage: the cellular artwork in physiology and disease. *Nucleus* **15**, 2387534 (2024).
15. Ren, H. *et al.* Postmitotic annulate lamellae assembly contributes to nuclear envelope reconstitution in daughter cells. *J Biol Chem* **294**, 10383–10391 (2019).

16. Raghunayakula, S., Subramonian, D., Dasso, M., Kumar, R. & Zhang, X.-D. Molecular Characterization and Functional Analysis of Annulate Lamellae Pore Complexes in Nuclear Transport in Mammalian Cells. *PLoS One* **10**, e0144508 (2015).
17. Patterson, J. R., Wood, M. P. & Schisa, J. A. Assembly of RNP granules in stressed and aging oocytes requires nucleoporins and is coordinated with nuclear membrane blebbing. *Dev Biol* **353**, 173–185 (2011).
18. Sahoo, M. R. *et al.* Nup358 binds to AGO proteins through its SUMO-interacting motifs and promotes the association of target mRNA with miRISC. *EMBO Rep* **18**, 241–263 (2017).
19. Rawe, V. Y., Olmedo, S. B., Nodar, F. N., Ponzio, R. & Sutovsky, P. Annulate lamellae assembly in non-inseminated and failed fertilized human oocytes. *Fertility and Sterility* **78**, S163 (2002).
20. Boulware, M. J. & Marchant, J. S. Nuclear pore disassembly from endoplasmic reticulum membranes promotes Ca2+ signalling competency. *J Physiol* **586**, 2873–2888 (2008).
21. Boulware, M. J. & Marchant, J. S. IP3 receptor activity is differentially regulated in endoplasmic reticulum subdomains during oocyte maturation. *Curr Biol* **15**, 765–770 (2005).
22. Jühlen, R. & Fahrenkrog, B. From the sideline: Tissue-specific nucleoporin function in health and disease, an update. *FEBS Letters* **597**, 2750–2768 (2023).
23. Coyne, A. N. & Rothstein, J. D. Nuclear pore complexes - a doorway to neural injury in neurodegeneration. *Nat Rev Neurol* **18**, 348–362 (2022).
24. Kuiper, E. F. E. *et al.* The chaperone DNAJB6 surveils FG-nucleoporins and is required for interphase nuclear pore complex biogenesis. *Nat Cell Biol* **24**, 1584–1594 (2022).
25. Agote-Aran, A. *et al.* Spatial control of nucleoporin condensation by fragile X-related proteins. *EMBO J* **39**, e104467 (2020).
26. Weberruss, M. & Antonin, W. Perforating the nuclear boundary - how nuclear pore complexes assemble. *J Cell Sci* **129**, 4439–4447 (2016).
27. Agote-Arán, A., Lin, J. & Sumara, I. Fragile X-Related Protein 1 Regulates Nucleoporin Localization in a Cell Cycle-Dependent Manner. *Front Cell Dev Biol* **9**, 755847 (2021).
28. Liao, Y. *et al.* UBAP2L ensures homeostasis of nuclear pore complexes at the intact nuclear envelope. *Journal of Cell Biology* **223**, e202310006 (2024).
29. Andronov, L., Vonesch, J.-L. & Klaholz, B. P. Practical Aspects of Super-Resolution Imaging and Segmentation of Macromolecular Complexes by dSTORM. *Methods Mol Biol* **2247**, 271–286 (2021).
30. Lelek, M. *et al.* Single-molecule localization microscopy. *Nat Rev Methods Primers* **1**, 39 (2021).
31. Andronov, L., Genthial, R., Hentsch, D. & Klaholz, B. P. splitSMLM, a spectral demixing method for high-precision multi-color localization microscopy applied to nuclear pore complexes. *Commun Biol* **5**, 1100 (2022).
32. Davis, L. I. & Blobel, G. Identification and characterization of a nuclear pore complex protein. *Cell* **45**, 699–709 (1986).
33. Kessel, R. G. The structure and function of annulate lamellae: porous cytoplasmic and intranuclear membranes. *Int Rev Cytol* **82**, 181–303 (1983).
34. Sachweh, J. *et al.* The small GTPase Ran defines Nuclear Pore Complex Asymmetry. Preprint at https://doi.org/10.1101/2024.10.10.617378 (2024).
35. Rasala, B. A., Ramos, C., Harel, A. & Forbes, D. J. Capture of AT-rich chromatin by ELYS recruits POM121 and NDC1 to initiate nuclear pore assembly. *Mol Biol Cell* **19**, 3982–3996 (2008).
36. Walther, T. C. *et al.* RanGTP mediates nuclear pore complex assembly. *Nature* **424**, 689–694 (2003).
37. Maul, G. G. *et al.* Time sequence of nuclear pore formation in phytohemagglutinin-stimulated lymphocytes and in HeLa cells during the cell cycle. *J Cell Biol* **55**, 433–447 (1972).

38. McKinney, S. A., Murphy, C. S., Hazelwood, K. L., Davidson, M. W. & Looger, L. L. A bright and photostable photoconvertible fluorescent protein. *Nat Methods* **6**, 131–133 (2009).
39. De Magistris, P. & Antonin, W. The Dynamic Nature of the Nuclear Envelope. *Current Biology* **28**, R487–R497 (2018).
40. Chen, S., Novick, P. & Ferro-Novick, S. ER structure and function. *Current Opinion in Cell Biology* **25**, 428–433 (2013).
41. Deolal, P., Scholz, J., Ren, K., Bragulat-Teixidor, H. & Otsuka, S. Sculpting nuclear envelope identity from the endoplasmic reticulum during the cell cycle. *Nucleus* **15**, 2299632 (2024).
42. Aksenova, V., Arnaoutov, A. & Dasso, M. Analysis of Nucleoporin Function Using Inducible Degron Techniques. *Methods Mol Biol* **2502**, 129–150 (2022).
43. Tomioka, Y. *et al.* TORC1 inactivation stimulates autophagy of nucleoporin and nuclear pore complexes. *J Cell Biol* **219**, e201910063 (2020).
44. Lee, C.-W. *et al.* Selective autophagy degrades nuclear pore complexes. *Nat Cell Biol* **22**, 159–166 (2020).
45. Bley, C. J. *et al.* Architecture of the cytoplasmic face of the nuclear pore. *Science* **376**, eabm9129 (2022).
46. Zhang, K. *et al.* The C9orf72 repeat expansion disrupts nucleocytoplasmic transport. *Nature* **525**, 56–61 (2015).
47. Niopek, D., Wehler, P., Roensch, J., Eils, R. & Di Ventura, B. Optogenetic control of nuclear protein export. *Nat Commun* **7**, 10624 (2016).
48. Von Appen, A. *et al.* In situ structural analysis of the human nuclear pore complex. *Nature* **526**, 140–143 (2015).
49. Onischenko, E. *et al.* Natively Unfolded FG Repeats Stabilize the Structure of the Nuclear Pore Complex. *Cell* **171**, 904-917.e19 (2017).
50. Vollmer, B. & Antonin, W. The diverse roles of the Nup93/Nic96 complex proteins – structural scaffolds of the nuclear pore complex with additional cellular functions. *Biological Chemistry* **395**, 515–528 (2014).
51. Schroeder, L. K. *et al.* Dynamic nanoscale morphology of the ER surveyed by STED microscopy. *Journal of Cell Biology* **218**, 83–96 (2019).
52. Shibata, Y. *et al.* Mechanisms Determining the Morphology of the Peripheral ER. *Cell* **143**, 774–788 (2010).
53. Klopfenstein, D. R. Ch., Kappeler, F. & Hauri, H.-P. A novel direct interaction of endoplasmic reticulum with microtubules. *The EMBO Journal* **17**, 6168–6177 (1998).
54. Otsuka, S. & Ellenberg, J. Mechanisms of nuclear pore complex assembly - two different ways of building one molecular machine. *FEBS Lett* **592**, 475–488 (2018).
55. Penzo, A. & Palancade, B. Puzzling out nuclear pore complex assembly. *FEBS Letters* **597**, 2705–2727 (2023).
56. Dultz, E., Wojtynek, M., Medalia, O. & Onischenko, E. The Nuclear Pore Complex: Birth, Life, and Death of a Cellular Behemoth. *Cells* **11**, 1456 (2022).
57. Otsuka, S. *et al.* A quantitative map of nuclear pore assembly reveals two distinct mechanisms. *Nature* **613**, 575–581 (2023).
58. Otsuka, S. *et al.* Postmitotic nuclear pore assembly proceeds by radial dilation of small membrane openings. *Nat Struct Mol Biol* **25**, 21–28 (2018).
59. Vitale, J., Khan, A., Neuner, A. & Schiebel, E. A perinuclear α-helix with amphipathic features in Brl1 promotes NPC assembly. *Mol Biol Cell* **33**, ar35 (2022).
60. Kralt, A. *et al.* An amphipathic helix in Brl1 is required for nuclear pore complex biogenesis in S. cerevisiae. *Elife* **11**, e78385 (2022).
61. Mondal, S., Neuner, A., Khan, A., Vitale, J. & Schiebel, E. Multifunctional Roles of Brr6 and Brl1 in Nuclear Envelope Fusion During Nuclear Pore Complex Biogenesis. Preprint at https://doi.org/10.1101/2025.07.22.665954 (2025).

838 62. Rampello, A. J. *et al.* Torsin ATPase deficiency leads to defects in nuclear pore biogenesis
839 and sequestration of MLF2. *J Cell Biol* **219**, e201910185 (2020).
840 63. Kim, S. *et al.* TorsinA is essential for neuronal nuclear pore complex localization and
841 maturation. *Nat Cell Biol* **26**, 1482–1495 (2024).
842 64. Joseph, J. & Dasso, M. The nucleoporin Nup358 associates with and regulates interphase
843 microtubules. *FEBS Lett* **582**, 190–196 (2008).
844 65. Cui, H. *et al.* Adapter Proteins for Opposing Motors Interact Simultaneously with Nuclear
845 Pore Protein Nup358. *Biochemistry* **58**, 5085–5097 (2019).
846 66. Ciccarelli, F. D. *et al.* Complex genomic rearrangements lead to novel primate gene
847 function. *Genome Res* **15**, 343–351 (2005).
848 67. Hetzer, M. W. The nuclear envelope. *Cold Spring Harb Perspect Biol* **2**, a000539 (2010).
849 68. Talamas, J. A. & Hetzer, M. W. POM121 and Sun1 play a role in early steps of interphase
850 NPC assembly. *Journal of Cell Biology* **194**, 27–37 (2011).
851 69. Eymieux, S., Blanchard, E., Uzbekov, R., Hourioux, C. & Roingeard, P. Annulate lamellae
852 and intracellular pathogens. *Cellular Microbiology* **23**, (2021).
853 70. Lin, Y.-C. *et al.* Interactions between ALS-linked FUS and nucleoporins are associated
854 with defects in the nucleocytoplasmic transport pathway. *Nat Neurosci* **24**, 1077–1088
855 (2021).
856 71. Gleixner, A. M. *et al.* NUP62 localizes to ALS/FTLD pathological assemblies and
857 contributes to TDP-43 insolubility. *Nat Commun* **13**, 3380 (2022).
858 72. Suhr, S. T. *et al.* Identities of sequestered proteins in aggregates from cells with induced
859 polyglutamine expression. *J Cell Biol* **153**, 283–294 (2001).
860 73. Grima, J. C. *et al.* Mutant Huntingtin Disrupts the Nuclear Pore Complex. *Neuron* **94**, 93-
861 107.e6 (2017).
862 74. Pappas, S. S., Liang, C.-C., Kim, S., Rivera, C. O. & Dauer, W. T. TorsinA dysfunction
863 causes persistent neuronal nuclear pore defects. *Hum Mol Genet* **27**, 407–420 (2018).
864 75. Zouiouich, M. *et al.* MOSPD2 is an endoplasmic reticulum-lipid droplet tether functioning
865 in LD homeostasis. *J Cell Biol* **221**, e202110044 (2022).
866 76. Ran, F. A. *et al.* Genome engineering using the CRISPR-Cas9 system. *Nat Protoc* **8**,
867 2281–2308 (2013).
868 77. Chou, Y.-Y. *et al.* Inherited nuclear pore substructures template post-mitotic pore
869 assembly. *Dev Cell* **56**, 1786-1803.e9 (2021).
870 78. Mossink, B. *et al.* Human neuronal networks on micro-electrode arrays are a highly robust
871 tool to study disease-specific genotype-phenotype correlations in vitro. *Stem Cell Reports*
872 **16**, 2182–2196 (2021).
873 79. Andronov, L., Genthial, R., Hentsch, D. & Klaholz, B. P. splitSMLM, a spectral demixing
874 method for high-precision multi-color localization microscopy applied to nuclear pore
875 complexes. *Commun Biol* **5**, 1100 (2022).
876 80. Andronov, L., Lutz, Y., Vonesch, J.-L. & Klaholz, B. P. SharpViSu: integrated analysis and
877 segmentation of super-resolution microscopy data. *Bioinformatics* **32**, 2239–2241 (2016).
878 81. Andronov, L. *et al.* 3DClusterViSu: 3D clustering analysis of super-resolution microscopy
879 data by 3D Voronoi tessellations. *Bioinformatics* **34**, 3004–3012 (2018).
880 82. Mastronarde, D. N. Automated electron microscope tomography using robust prediction
881 of specimen movements. *J Struct Biol* **152**, 36–51 (2005).
882 83. Kremer, J. R., Mastronarde, D. N. & McIntosh, J. R. Computer visualization of three-
883 dimensional image data using IMOD. *J Struct Biol* **116**, 71–76 (1996).
884 84. Paul-Gilloteaux, P. *et al.* eC-CLEM: flexible multidimensional registration software for
885 correlative microscopies. *Nat Methods* **14**, 102–103 (2017).
886 85. de Chaumont, F. *et al.* Icy: an open bioimage informatics platform for extended
887 reproducible research. *Nat Methods* **9**, 690–696 (2012).
888 86. van der Walt, S. *et al.* scikit-image: image processing in Python. *PeerJ* **2**, e453 (2014).
889 87. Boni, A. *et al.* Live imaging and modeling of inner nuclear membrane targeting reveals its
890 molecular requirements in mammalian cells. *J Cell Biol* **209**, 705–720 (2015).

88. Miura, K. Measurements of Intensity Dynamics at the Periphery of the Nucleus. in *Bioimage Data Analysis Workflows* (eds. Miura, K. & Sladoje, N.) 9–32 (Springer International Publishing, Cham, 2020). doi:10.1007/978-3-030-22386-1_2.

Methods

Antibodies

The following primary antibodies were used: rabbit monoclonal anti-Nup133 (Abcam, ab155990), mouse monoclonal anti-Nup133 (E-6) (Santa Cruz Biotechnology, sc-376763), mouse monoclonal anti-Nucleoporin p62 (BD Biosciences, 610497), rabbit polyclonal anti-RanBP2 (Abcam, ab64276), rabbit polyclonal anti-Nup214 (Abcam, ab70497), rabbit polyclonal anti-Nup85 (Bethyl, A303-977A), mouse monoclonal anti-Pericentrin 1 (D-4) (Nup85) (Santa Cruz Biotechnology, sc-376111), rabbit monoclonal anti-SEC13 (R&D systems, MAB9055), rabbit polyclonal anti- ELYS (Bethyl, A300-166A), mouse monoclonal Nup205 (H-1) (Santa Cruz Biotechnology, sc-377047), mouse monoclonal anti-Nup93 (E-8) (Santa Cruz Biotechnology, sc-374399), rabbit monoclonal anti-Nup98 (C39A3) (Cell Signaling Technology, 2598), rabbit polyclonal anti-Nup96 (Bethyl, A301-784A), rabbit polyclonal anti-POM121 (GeneTex, GTX102128), rabbit polyclonal anti-Nup153 (Abcam, ab84872), rabbit polyclonal anti-CRM1/Exportin 1 (Novus, NB100-79802), mouse monoclonal anti-NTF97/Importin beta (Abcam, ab2811), mouse monoclonal anti-Ran (BD Biosciences, 610340), rabbit monoclonal anti-SUN1 (Abcam, ab124770), rabbit monoclonal anti-SUN2 (Abcam, ab124916), rabbit polyclonal anti-Lamin A (C-terminal) (Sigma, L1293), rabbit polyclonal anti-Lamin B1 (Abcam, ab16048), rabbit monoclonal anti-Nesprin1 (Abcam, ab192234), rabbit polyclonal anti-Emerin (Abcam, ab40688), rabbit polyclonal anti-LAP2 (Proteintech, 14651-1-AP), rabbit polyclonal anti-Phospho-Rb (Ser807/811) (Cell Signaling Technology, 9308), mouse monoclonal anti-Cyclin B1 (G-11) (Santa Cruz Biotechnology, sc-166757), rabbit polyclonal anti-Cyclin B1 (GeneTex, GTX100911), rat monoclonal anti-HA (Roche, 11867423001), rabbit polyclonal anti-GAPDH (Sigma, G9545), mouse monoclonal anti-β-Actin (Sigma, A2228), mouse monoclonal anti-mCherry (4B3) (Thermo Scientific, MA5-32977), rabbit polyclonal anti-UBAP2L (Abcam, ab138309), mouse monoclonal anti-FXR1 (Millipore, 03-176), rabbit polyclonal anti-α-Tubulin (Abcam, ab18251), mouse monoclonal anti-α-Tubulin (Sigma, T9026), mouse monoclonal anti-Nuclear Pore Complex Proteins (mAb414) (Abcam, ab24609), rabbit polyclonal anti-LC3B (Novus biological, NB100-2220SS), rabbit polyclonal anti-LC3A (Novus biological, NB100-2331), rabbit polyclonal anti-p62 (GeneTex, GTX100685), rat monoclonal anti-GFP (3H9) (ChromoTek, 3h9-100), rabbit polyclonal anti-GFP (Abcam, ab290), rabbit polyclonal anti-Aurora B (Abcam, ab2254), rabbit polyclonal anti-cyclin A (H-432) (Santa Cruz Biotechnology, sc-751), mouse monoclonal anti-PDI (Abcam, ab2792), mouse monoclonal anti-Climp63 (Enzo, ALX-804-604), rabbit polyclonal anti-CKAP4 (Proteintech, 16686-1-AP), rat monoclonal α-tubulin-conjugated to Alexa Fluor® 647 (Abcam, ab195884), rabbit polyclonal anti-RTN4/NOGO (Proteintech, 10950-1-AP), rabbit polyclonal anti-RRBP1 (Proteintech, 22015-1-AP), rabbit polyclonal anti-KTN1 (Proteintech, 19841-1-AP), rabbit polyclonal anti-ATL1(OriGene, ta332595), rabbit polyclonal anti-ATL3 (Proteintech, 16921-1-AP), rabbit polyclonal anti-LNPK (Atlas Antibodies, HPA014205).

Secondary antibodies used were the following: goat anti-mouse IgG antibody (HRP) (GeneTex, GTX213111-01), goat anti-rabbit IgG antibody (HRP) (GeneTex, GTX213110-01) and goat anti-rat IgG antibody (HRP) (Cell Signaling Technology, 7077S), goat polyclonal anti-mouse AF647 (Thermo Fisher Scientific, A-21236), goat polyclonal anti-mouse AF568 (Thermo Fisher Scientific, A-11031), goat polyclonal anti-mouse AF555 (Thermo Fisher Scientific, A-21424), goat polyclonal anti-mouse AF488 (Thermo Fisher Scientific, A-11029), goat polyclonal anti-rabbit AF647 (Thermo Fisher Scientific, A-21245), goat polyclonal anti-rabbit AF568 (Thermo Fisher Scientific, A-11036), goat polyclonal anti-rabbit AF555 (Thermo Fisher Scientific, A-21429), goat polyclonal anti-rabbit AF488 (Thermo Fisher Scientific, A-11034), goat polyclonal anti-mouse CF680 (Sigma, SAB4600199), goat polyclonal anti-

947 chicken CF660C (Sigma, SAB4600458), goat polyclonal anti-rat CF660C (Sigma,
948 SAB4600193).

949 **Plasmid and siRNA transfections**

950 The following plasmids were used: pX330-P2A-EGFP/RFP and pUC57 was a generous gift
951 from Zhirong Zhang (Romeo Ricci laboratory IGBMC). pQCXIP-mScarlet-ER was a generous
952 gift from Julie EICHLER [75] (Catherine-Laure Tomasetto laboratory IGBMC). pEF-HA-MCS2,
953 pEF-HA-RanBP2 (1-3224), pEF-HA-RanBP2 (1-2448), and pEF-HA-RanBP2 (1-1171) were
954 generous gifts from Ralph Kehlenbach (University of Göttingen). pEF-HA-RanBP2 (1-832) and
955 pEF-HA-RanBP2 (FL without FG repeat) was obtained by inserting the target sequence,
956 obtained by PCR using pEF-HA-RanBP2 as a template, into pEF-HA-MCS2. pCDNA 3.1
957 3XHA NUP358 FL (LIQIML) was generous gifts from André Hoelz (California Institute of
958 Technology). The siRNA-resistant RanBP2 plasmid was obtained by PCR and DpnI (Thermo)
959 treatment. NLS-mCherry-LEXY (pDN122) (Plasmid #72655) and mEos2-N1 (Plasmid #54662)
960 was purchased from Addgene. The primers used for plasmid generation are provided in the
961 Supplementary Table 1.

962 The following siRNA oligonucleotides were used: Non-targeting individual siRNA
963 (Dharmacon), FXR1 siRNA (Dharmacon), UBAP2L siRNA (Dharmacon), RanBP2 siRNA
964 (Dharmacon), Nup153 siRNA (Dharmacon), ELYS siRNA (Dharmacon), POM121 siRNA (Life
965 Technologies), Nup214 siRNA (Eurogenetec), Nup93 siRNA (Horizon), CLIMP-
966 63(Dharmacon), RTN4 (Horizon), p180/RRBP1 (Horizon), KTN1 (Horizon), ATL1 (Horizon),
967 ATL3 (Horizon), LNPK (Horizon). The sequences of siRNA are provided in the Supplementary
968 Table 1.

969 X-tremeGENE™ 9 DNA Transfection Reagent (Roche) was used to perform transient plasmid
970 transfections according to the manufacturer's instructions. Lipofectamine™ RNAiMAX
971 Transfection Reagent (Invitrogen) was used to deliver siRNAs for gene knock-down (KD)
972 according to the manufacturer's instructions.

973

974 **Generation of cell lines and cell culture**

975 HeLa Kyoto (human cervix carcinoma) cells and U2OS (human bone osteosarcoma) cells
976 were purchased from ATCC. HeLa Kyoto GFP-Nup107 derived stable cell were purchased
977 from CSL cell bank. AID-NUP358 DLD-1 (colorectal adenocarcinoma epithelial cells) cells and
978 AID-NUP358 HTC116 (human colon cancer cells) cells were generous gifts from Mary Dasso
979 (National Institutes of Health). hTERT-RPE1 (Human retinal pigment epithelial-1) cells was a
980 generous gift from Juliette Godin (IGBMC). FB789 (Human Fibroblast) cells was a generous
981 gift from PROIETTI Luca (IGBMC). MRC5 (Human Fibroblast) cells was a generous gift from
982 SEROZ Thierry (IGBMC).Control human fibroblasts and FXS patient-derived fibroblasts were
983 previously reported[25].

984 mCherry-Nup133 and mEos2-Nup133 knock-in HeLa Kyoto cell lines were generated using
985 CRISPR/Cas9 genome editing system as described previously[76]. The guide RNAs (gRNA)
986 were designed as described previously[77], and cloned into pX330-P2A-EGFP through ligation
987 using T4 ligase (New England Biolabs). The donor constructs used as templates for
988 homologous recombination to repair the Cas9-induced double-strand DNA breaks were
989 generated by cloning the Nup133 DNA fragments upstream and downstream of the CRISPR
990 target sequences and the sequence for mCherry or mEos2, assembled using ExonucleaseIII
991 (Takara) method, into a pUC57 vector. HeLa Kyoto cells were transfected for 24h and GFP
992 positive cells were collected by FACS (BD FACS Aria II), cultured for 2 days and seeded with
993 FACS into 96-well plates. Single-cell clones of mCherry-Nup133 knock-in or mEos2-Nup133
994 knock-in were validated by Western blot and sequencing of PCR-amplified targeted fragment

995 by Sanger sequencing (GATC). The sequences of gRNA and the primers used for plasmid
996 generation are provided in the Supplementary Table 1.

997 UBAP2L knock-out (KO) in mCherry-Nup133 knock-in HeLa Kyoto cell lines were generated
998 using CRISPR/Cas9 genome editing system as described previously[76]. Two guide RNAs
999 (gRNA) were designed using the online software Benchling (https://www.benchling.com/), and
1000 cloned into pX330-P2A-EGFP/RFP through ligation using T4 ligase (New England Biolabs).
1001 mCherry-Nup133 knock-in HeLa Kyoto cells were transfected for 24h and GFP and RFP
1002 double positive cells were collected by FACS (BD FACS Aria II), cultured for 2 days and
1003 seeded with FACS into 96-well plates. UBAP2L KO single-cell clones were validated by
1004 Western blot and sequencing of PCR-amplified targeted fragment by Sanger sequencing
1005 (GATC). The sequences of gRNA are provided in the Supplementary Table 1.

1006 All cell lines were cultured at 37°C in 5 % CO2 humidified incubator. HeLa Kyoto and its derived
1007 cell lines were cultured in Dulbecco's Modified Eagle Medium (DMEM) (4.5 g/L glucose)
1008 supplemented with 10 % fetal calf serum (FCS), 100 U/ml Penicillin + 100 µg/ml Streptomycin.
1009 U2OS cell lines were cultured in DMEM (1 g/L glucose) supplemented with 10 % FCS, Non-
1010 Essential Amino Acids + Sodium Pyruvate 1 mM + Gentamicin 40 µg/mL. DLD-1 cell lines
1011 were cultured in DMEM (1 g/L glucose) supplemented with 10 % FCS, 100 U/ml penicillin, and
1012 100 µg/ml streptomycin. HTC116 cell lines were cultured in McCoy's 5A medium + 10 % FCS
1013 + 100 U/ml penicillin, and 100 µg/ml streptomycin. hTERT-RPE1 cells were cultured in
1014 Dulbecco's modified Eagle medium (DMEM) F-12 supplemented with 10% FCS, 0.01 mg/ml
1015 hygromycin B. FB 789 cell lines were cultured in MEM w/Earles's salts supplemented with 15 %
1016 FCS, + Vitamines + AANE + Gentamicine 40 µg/ml + Penicillin 100 UI/ml + Streptomycin 100
1017 µg/ml. MRC5 cell lines were cultured in DMEM (1 g/L glucose) supplemented with 10 % FCS,
1018 + Gentamicine 40 µg/ml.

1019

1020 **Culture and differentiation of hiPSCs into neurons**
1021 Human induced pluripotent stem cells (hiPSCs, GM8330-8; kindly given by M. E. Talkowski)
1022 were cultured in mTeSR1, following the manufacturer's instructions, and maintained on
1023 Cultrex-BME. hiPSCs were cultured at 37°C with 5% CO_2 under humidified conditions.
1024 Colonies were passaged every 3 to 4 days by manual cutting.
1025 For the generation of inducible rtTA/Ngn2 hiPSC lines, Lentiviral vectors (PCW57) containing
1026 the human NGN2 gene cassette under the control of the TRE promoter, along with a
1027 puromycin resistance gene linked to rTetR via a T2A sequence under a constitutive promoter,
1028 were used to transduce hiPSCs. The construct was cloned and packaged into lentiviruses by
1029 the Molecular Biology Platform of the IGBMC, hereafter named TetO-NGN2 lentivirus.
1030 hiPSCs were dissociated using Accutase and seeded in 12-well plates at a density of 6×10^4
1031 cells per well in mTeSR1 supplemented with 10 µM Rocki (STEMCell), and incubated
1032 overnight at 37°C. The next day, the medium was removed, and the cells were incubated for
1033 6 hours in DMEM/F12 containing 8 µg/ml Polybrene, 10 µM Rocki, and 4×10^4 TU of TetO-
1034 NGN2 lentivirus. After 6 hours, cells were washed with DPBS (Thermo Fisher) and returned
1035 to mTeSR1 at 37°C and 5% CO_2. Puromycin selection began on day 1 post-transduction, with
1036 0.5 µg/ml from day 1 to 2, 1 µg/ml from day 3 to 4, and then 0.5 µg/ml again from day 5 to 7,
1037 with daily medium changes using mTeSR1. Selected hiPSC colonies were subsequently
1038 expanded in new Cultrex-BME-coated plates after Accutase dissociation and maintained
1039 under standard conditions.
1040
1041 For the differentiation of rtTA/Ngn2 hiPSCs into induced neurons, the differentiation was
1042 adapted from reported protocol without addition of astrocytes[78]. On day 0, TetO-NGN2 hiPSCs
1043 were dissociated with Accutase and seeded at a density of 4×10^5 cells/cm² on Poly-L-
1044 Ornithine (50 µg/cm²) + Laminin (7 µg/cm²)-coated petri dishes and in mTeSR1 supplemented
1045 with 10 µM Rocki and 3 µg/ml doxycycline. On day 1, media was replaced with DMEM/F12 +

1046 Glutamax 1X + NEAA 1X + B27 1X + N2 1X + doxycycline 3 µg/ml. On day 3, media was
1047 replaced with Neurobasal + Glutamax 1X + NEAA 1X + B27 1X + NT-3 (10 ng/mL) + BDNF
1048 (10 ng/mL) + doxycycline 3 µg/ml + cytosine β-D-arabinofuranoside (AraC) 5 µM. From day 5
1049 to day 20, media was half-changed each 3-4 days with Neurobasal + Glutamax 1X + NEAA
1050 1X + B27 1X + NT-3 (10 ng/mL) + BDNF (10 ng/mL) + doxycycline 3 µg/ml. Doxycycline was
1051 maintained until day 14 of differentiation. Neurons were fixed/immunostained at 20 DIV.

1052

1053 **Cell treatments and cell cycle synchronization**
1054 To induce the formation of the cytoplasmic AL foci by microtubule depolymerization, cells were
1055 incubated with 10 µM nocodazole (Sigma M1404-50MG) in culture media for 90 min at 37°C.
1056 To inhibit autophagy, cells were incubated with 30 nM Bafilomycin (Sigma, B1793-10UG) in
1057 culture media for 12h at 37°C. Cells were synchronized in early G1 by the addition of thymidine
1058 (Sigma, T1895) at 2 mM for 16h. For cell cycle synchronizations double thymidine block and
1059 release (DTBR) protocol was used. Cells were treated with 2 mM thymidine for 16h, washed
1060 out (three times with warm thymidine-free medium), then released in fresh thymidine-free
1061 culture medium for 8h, treated with 2 mM thymidine for 16h again, washed out, and then
1062 released in fresh thymidine-free culture medium for 9h (mitosis) or 12 hours early G1 phase.

1063

1064 **Immunofluorescence**
1065 Cells were plated on 9-15 mm glass coverslips (Menzel Glaser) in 12- or 24- well tissue culture
1066 plates. For immunofluorescence, cells were washed twice with PBS before being fixed with 4
1067 % paraformaldehyde (PFA, Electron Microscopy Sciences 15710) in PBS for 15-20 min at
1068 room temperature. Cells were washed three times for 5 min in PBS before permeabilization
1069 for 5 min with 0.5 % NP-40 (Sigma) in PBS. Cells were washed three times for 5 min in PBS
1070 before blocking for 1h at room temperature with 3 % BSA in PBS-Triton 0.01 % (Triton X-100,
1071 Sigma, T8787). Cells were then incubated with primary antibody in blocking buffer (3 % BSA
1072 in PBS-Triton 0.01 %) for 1h at room temperature. Cells were washed three times with PBS-
1073 Triton 0.01 % gently shaking for 10 min before incubated with secondary antibody in blocking
1074 buffer for 1h at room temperature in the dark. After incubation, cells were washed 3 times with
1075 PBS-Triton 0.01 % for 10 min each time with gentle shaking in the dark, and then glass
1076 coverslips were mounted on glass slides using MOWIOL containing 0.75 µg/ml DAPI
1077 (Calbiochem) and imaged with 100X, 63X or 40X objectives using Zeiss epifluorescence
1078 microscope or confocal microscope Leica Spinning Disk Andor/Yokogawa.

1079

1080 **Live-cell imaging**
1081 For live-cell microscopy, cells were grown on 35/10 mm 4 compartment glass bottom dishes
1082 (Greiner Bio-One, 627871) or µ-Slide 8 well glass bottom (Ibidi, 80827). Before photography,
1083 cells were treated with SiR-DNA (Spirochrome, SC007) according to the manufacturer's
1084 instructions. Live cell microscopy was performed using a confocal microscope
1085 Leica/Andor/Yokogawa spinning disc, Leica CSU-W1 spinning disc, or Nikon PFS spinning
1086 disc with a 40X or 63X objectives with Live Data Mode equipped with automated temperature.

1087 In particular, for AL foci' dynamics assays under normal growth conditions, HeLa Kyoto GFP-
1088 Nup107 were analyzed by Leica CSU-W1 spinning disk (63X NA 1.4 oil objective) for 9h. Z-
1089 stacks (10 µm range, 1 µm step) were acquired every 5 min and Videos were made with
1090 maximum intensity projection images for every time point shown at speed of 7 frames per
1091 second. For AL foci' dynamics assays after microtubule depolymerization, HeLa Kyoto GFP-
1092 Nup107 cell were arrested in S phase by thymidine block and microtubule depolymerization
1093 and nucleoporin aggregation were induced by 10 µM nocodazole addition. For AL foci'

1094 dynamics assays under FXR1 knockdown (KD) or UBAP2L KD conditions, HeLa Kyoto GFP-
1095 Nup107 derived stable cell were treated with the indicated siRNAs for 48 h before imaging.

1096 For rapid super-resolution live-cell imaging, HeLa Kyoto GFP-Nup107 were analyzed by Nikon
1097 PFS spinning disk (100X NA1.4 oil objective) for 15 min using Live-SR mode. Z-stacks (7 µm
1098 range, 1 µm step) were acquired every 3 s and Videos were made with maximum intensity
1099 projection images for every time point shown at speed of 7 frames per second. For AL foci and
1100 microtubules dynamics assays, cells were treated with SiR-tubulin (Spirochrome, SC002)
1101 according to the manufacturer's instructions.

1102 For AL foci and ER' dynamics assays, HeLa Kyoto GFP-Nup107 were transfected with the
1103 pQCXIP-mScarlet-ER for 24 h and analyzed by Nikon PFS spinning disk (100X NA1.4 oil
1104 objective) for 5h where images were acquired every 20s (without Z-stacks) or were analyzed
1105 for 9h where images were acquired every 2 min (without Z-stacks).

1106 For photoactivatable nucleocytoplasmic shuttling, AID-NUP358 DLD-1 were transfected with
1107 the NLS-mCherry-LEXY (pDN122) for 24h and analyzed by Leica Sp5 confocal inverted
1108 microscope (DMI6000) system (40X NA1.3 oil objective). The circular region of interest (ROI;
1109 ~38 µm2) was placed onto single, selected cells. The ROI was scanned with a 458-nm laser
1110 beam for 10 min following a 20-min dark-recovery phase. The mCherry signal was imaged in
1111 parallel every 10s for 30 min using the 561-nm laser line for excitation.

1112 For photoconversion assays, HeLa Kyoto mEos2-Nup133 were analyzed by Nikon PFS
1113 spinning disk (100X NA1.4 oil objective). The modular part developed by the GATACA system
1114 was used to set the acquisition of the selected area to be photoconverted with applied repeats
1115 of blue light for a period of 200 seconds (typical value, depending on the size of the area) by
1116 the 500 mW laser diode at 100%. A 30-second acquisition pre-sequence and with acquisition
1117 every 10 seconds in the green and red channels has been perfomrmed. Two post sequences
1118 are carried out after acquisition, the first for 30 seconds with an interval every 10 seconds in
1119 order to quickly observe the effect of photoconversion and the second sequence for 12 hours
1120 every 15 minutes to see the effect over a longer period. The software was set up to use
1121 spinning with the 491 nm 50 mW laser diode at 20% power with an acquisition time of 150 ms
1122 for the green channel and the 561 nm 50 mW laser diode at 30% power with 150 ms exposure
1123 time for the red channel.

1124

1125 **Single molecule localization microscopy**
1126 For super-resolution imaging using single molecule localization microscopy (SMLM), cells
1127 were plated on 35 mm glass bottom dish with 14 mm micro-well #1.5 cover glass (Cellvis).
1128 Samples were prepared as described above for immunofluorescence but were not mounted
1129 using MOWIOL and were stored in PBS.

1130 The imaging was performed as previously described, using the splitSMLM method[79] for multi-
1131 color single molecule localization microscopy (SMLM) based on a dichroic image splitter. In
1132 brief, the immunolabeled samples were mounted in imaging buffer containing 200 U/ml
1133 glucose oxidase (G2133, Sigma), 1000 U/ml catalase (C1345, Sigma), 10 % w/v glucose, 200
1134 mM Tris-HCl pH 8.0, 10 mM NaCl, 50 mM MEA (30080, Sigma), with addition of 2 mM COT
1135 (138924, Sigma). The buffer optimizes the performance of the fluorophores AF647, CF660C
1136 and CF680, for three-color direct stochastic optical reconstruction microscopy (dSTORM).
1137 Imaging was then performed on a modified Leica SR GSD system, with a HCX PL APO
1138 160X/1.43 Oil CORR TIRF PIFOC objective. The acquisitions began with a pumping phase,
1139 during which the sample was illuminated with the 642 nm 500 mW fiber laser (MBP
1140 Communication Inc.) but the fluorescence was not recorded due to a very high density of
1141 fluorophores in a bright state. The image collection started when the density of fluorophores
1142 dropped to a level that allowed observation of individual molecules and in case of emitter

depletion, the sample was additionally illuminated with a 405 nm diode laser (Coherent Inc.) to increase the emitter density (back-pumping). The resulting emission was split with an Optosplit II (Cairn Research) image splitter, attached to a camera port of the microscope, and containing a Chroma T690LPXXR dichroic mirror. This creates a long and short wavelength channel on the Andor iXon Ultra 897 EMCCD camera attached to the image splitter. Each fluorophore thus shows a characteristic brightness ratio between the two channels, enabling the separation of spectrally different fluorophore species (i.e., spectral demixing)[79]. Localization of the single molecules in both channels was performed using the Leica LAS X software with the "direct fit" fitting method. The localization tables were then exported and further processed using the SharpViSu software[29,80,81] and the SplitViSu plugin[79]. This accounts for spectral demixing, correction of chromatic errors, drift-correction, and the reconstruction of super-resolution images. A pixel size of 10 nm was used to reconstruct the super-resolution images from 2D-histograms of single-molecule coordinates. For the single-color imaging without image-splitter, the images were recorded with an Andor iXon + EMCCD camera, attached to the second camera port of the microscope. Data was then processed as already described, using the Leica LAS X and SharpViSu software, while omitting the spectral demixing steps in the SplitViSu plugin.

The NPCs area enlarged in the article uses Bilinear interpolation for better observation.

Correlative light and electron microscopy

Cells were grown on carbon coated sapphire disks (3 mm diameter, 50 mm thickness, Wohlwend GmbH, art. 405) and high pressure frozen (HPM010, AbraFluid) in their culture medium. Freeze substitution was performed in a Leica EM-AFS2 with 0.1 % uranyl acetate in dry acetone for 24h at -90°C. The temperature was then raised to -45°C over 9h (slope 5 degrees / hour) and the samples were further incubated at this temperature for 5h to increase electron contrast. After rinsing in acetone, the samples were infiltrated with increasing concentrations of Lowicryl HM20 (Polysciences Inc.), while raising the temperature to -25°C. Finally, the blocks were polymerized using UV light. After removal of the sapphire disks from the block surface, 300 nm sections were cut parallel to the block surface using an ultramicrotome (UC7, Leica Microsystems). The sections were collected on carbon coated mesh grids (S160, Plano).

Fluorescence imaging of the sections was carried out with a widefield microscope (Olympus IX81), equipped with a 100X 1.40 NA Plan-Apochromat objective, placing the grids in water in a glass bottom dish (Mattek). After light microscopy acquisition, the grids were post-stained with 2 % uranyl acetate in 70 % methanol and Reynold's lead citrate. Electron microscopy (EM) was performed using a Tecnai F30 transmission electron microscope (Thermo Fisher) at 300kV acceleration voltage. The grid squares that were previously imaged at the light microscope (LM) were mapped at low mag. After registration with the LM image, TEM tomography was performed on the areas of interest using the software package SerialEM[82]. Tomograms were reconstructed with IMOD[83]. Correlation between LM and EM images was done with the plugin ec-CLEM[84] of the software platform Icy[85], using features of the samples that could be identified in both imaging modalities.

Image analysis

Image quantification analysis was performed using ImageJ or CellProfiler software. In particular, the presence of Nups AL foci was confirmed by eyes by two individuals.
For nuclear size or nuclear envelope intensity analysis of Nups, CellProfiler software was used. Briefly, the Prewitt Edge Finder method was used to enhance the edges in a DAPI image, and then a nucleus size threshold is set to automatically identify nuclei. This allowed identification

1192 and measurement of nuclei area, morphology factor and mean nuclear intensity for the desired
1193 channel. The software's parameter measurements were exported to an Excel file and
1194 statistically analyzed.

1195 For the size of Nups foci, ImageJ software was used. In brief, the Nups channel was
1196 thresholded in ImageJ and then the size of the Nups foci was calculated by analyzing particles
1197 (size 1-100). AL foci that were considered “large” had a size bigger than 0,3 μm^2.

1198 For co-localization analysis of RanBP2 and Nups in cytoplasm, CellProfiler software was used.
1199 The Prewitt Edge Finder method was used to enhance the edges in a DAPI image, and then
1200 nuclei, RanBP2 and different Nups were identified according to the corresponding channels.
1201 The cytoplasmic fraction of RanBP2 and Nups was identified using MaskObjects module. Co-
1202 localization analysis of RanBP2 and Nups in cytoplasm was conducted by
1203 MeasureObjectOverlap module. The software's parameter measurements were exported to
1204 an Excel file and statistically analyzed. For nuclear envelope or cytoplasm intensity of Ran,
1205 ImageJ was used. The ROI of cell and nuclei were selected based on tubulin and DAPI
1206 channels, and the ROI of cytoplasm was selected by XOR of cell and nuclei. Finally, the mean
1207 gray value of the nuclei and cytoplasm was measured.

1208 For AL-NPCs analysis in the cytoplasm, AL-NPCs were recognized by Nup133 signal
1209 surrounding Nup62 signals. The number of AL-NPCs was counted visually by two individuals.

1210 For the measurement of NPCs density on the nuclear membrane, ImageJ software was used.
1211 Briefly, the images of the Nup62 channel were converted to 32 bits using ImageJ and then
1212 filtered using Gaussin blur (2). The nuclear region was manually selected and then find
1213 maxima (10) was performed to obtain the area of the selected region and the number of AL-
1214 NPCs.

1215 For protein import and export assay analysis, ImageJ software was used. Briefly, the ROI
1216 within uniform distribution of NLS-mCherry-LEXY signal was selected in the nuclear region,
1217 and the measurement of the mean gray value of the same ROI in each frame (time
1218 sequentially) was performed by multi-measure option.

1219 For calculation of the mean fluorescence intensity of Nups as a function of distance from the
1220 nucleus a custom Python script was used with help of the scikit-image module[86]. The nucleus
1221 and the nuclear envelope were identified using the RanBP2 channel following well-established
1222 procedures[87,88]. Similarly, the region corresponding to the ER was determined from the
1223 mScarlet-ER channel. Regions corresponding to RanBP2 foci were detected using the scikit-
1224 image method blob_log for blob detection. The analyzed region for Climp63 and mScarlet-ER
1225 corresponded to the ER region excluding the nucleus. The analyzed region for the RanBP2
1226 foci corresponded to the blob regions that fall within the ER region excluding the nucleus. For
1227 each pixel in the analyzed regions, the minimum Euclidean distance to any nuclear envelope
1228 pixel was taken as the distance from the nucleus. Given the intensity-distance pairs for each
1229 pixel, the pixels were binned for the distance and the mean pixel intensity determined for each
1230 bin. The obtained histograms were finally normalized for purpose of comparison.

1231 For Colocalization analysis, to assess pixel colocalization/correlation, we used correlation
1232 measurement within CellProfiler. Briefly, we used the "MaskImage" module to obtain Climp63,
1233 mScarlet-ER, and RanBP2 located in the cytoplasm. “Measure Colocalization” modules were
1234 used to study the colocalization and correlation between intensities in different images
1235 (different color channels) on a pixel-by-pixel basis across an entire image. The number of cells
1236 measured per condition was listed in the corresponding figure’s legend.

1237 For nuclear height measurement, confocal microscopy was used to perform z-sampling of the DAPI
1238 channel of the sample, with a z-step of 0.5 µm. Finally, Fiji analysis was used to obtain an
1239 approximate nuclear height based on the Z-Extent.

1240

1241 **Protein sample preparation and Western blotting**
1242 After centrifugation at 250 g for 3 minutes at 4°C, cells were washed twice with cold PBS, and
1243 lysates were prepared using cell lysis buffer (50 mM Tris-HCl pH 7.5, 150 mM NaCl, 0.5 %
1244 sodium deoxycholate, 0.1% SDS, 0.5% sodium deoxycholate, 1 % Triton X-100, 1 mM EDTA,
1245 1 mM EGTA, 2 mM Sodium pyrophosphate, 1 mM Na3VO4 and 1 mM NaF) supplemented
1246 with protease inhibitor cocktail (Roche) and incubated on ice for 30-60 min. After centrifugation
1247 at 16 000 g for 15 min at 4°C, the supernatant was transferred to the new clean Eppendorf
1248 tubes, and the total protein concentration was measured with a Bio-Rad Protein Assay kit (Bio-
1249 Rad). Separation of cytoplasmic and nuclear fractions was done using the NE-PER nuclear
1250 and cytoplasmic extraction reagent kit (Thermo Scientific™, 78833). Protein samples were
1251 boiled for 10 min at 95°C in 1X Laemmli buffer (LB) with β-Mercaptoethanol (BioRad,
1252 1610747).

1253 SDS-PAGE of proteins was done using pre-cast 4-12 % Bis-Tris gradient gels (Thermo
1254 Scientific, NW04120BOX) or pre-cast NuPAGE™ 3-8 % Tris-Acetate gradient Gels (Thermo
1255 Scientific, EA0378BOX). Proteins were transferred to a polyvinylidene difluoride (PVDF)
1256 membrane (Millipore, IPFL00010) using wet transfer modules (BIO-RAD Mini-PROTEAN®
1257 Tetra System). Membranes were blocked in 5 % bovine serum albumin (BSA, Millipore,
1258 160069), or 5% non-fat milk powder mixed with 3 % BSA resuspended in TBS-T for 1h at room
1259 temperature, followed by incubation with primary antibodies diluted in TBS-T 5 % BSA/5 %
1260 milk overnight at 4°C or 1h at room temperature and secondary antibodies diluted in TBS-T 5
1261 % BSA/5 % milk at room temperature. Membranes were imaged using SuperSignal West Pico
1262 (Pierce, Ref. 34580). Western blotting images were acquired by GE Healthcare_Amersham
1263 Imager 600 or Invitrogen iBright 1500. The grayscale value of protein bands was quantified
1264 using ImageJ software.

1265

1266 **Immunoprecipitation**
1267 Cell lysates were prepared for immunoprecipitations (IP) as described above. Lysates were
1268 adjusted to equal volume and concentration. For endogenous IP experiments, lysates were
1269 incubated with IgG or target-specific antibodies overnight at 4°C with rotation, and then
1270 incubated with protein G sepharose 4 Fast Flow beads (GE Healthcare Life Sciences) for 4h
1271 at 4°C with rotation. Before using, beads were blocked with 3 % BSA diluted in 1X cell lysis
1272 buffer and incubated for 2h at 4°C with rotation. The incubated IgG/ specific antibodies-
1273 samples-beads were washed with washing buffer (25 mM Tris-HCl pH 7.5, 300 mM NaCl, 0.5
1274 % Triton X-100, 0.5 mM EDTA, 0.5 mM EGTA, 1 mM Sodium pyrophosphate, 0.5 mM Na3VO4
1275 and 0.5 mM NaF) or TBS-T 4 to 6 times.

1276 For GFP-IP/HA-IP experiments, GFP-Trap A agarose beads (Chromotek) or Pierce™ anti-HA
1277 Magnetic Beads (Thermo Scientific 88836) were used. Cells expressing GFP- or HA-tagged
1278 plasmids for at least 24h before lysis were used. Lysates were incubated with beads for 4h at
1279 4°C with rotation, and then washed with washing buffer (25 mM Tris-HCl pH 7.5, 300 mM
1280 NaCl, 0.5 % Triton X-100, 0.5 mM EDTA, 0.5 mM EGTA, 1 mM Sodium pyrophosphate, 0.5
1281 mM Na3VO4 and 0.5 mM NaF) or TBS-T 4 to 6 times.

1282

1283 **Gel fractionation**
1284 To calibrate the Superose 6 Increase 3.2/300 column, the gel filtration standard (Bio-Rad,
1285 Catalog # 1511901) was rehydrated and diluted to 1.5 mg/mL according to the instruction of
1286 the manufacturer. The column was equilibrated using buffer comprising 15 mM pH 7.5 Tris,
1287 15 mM NaCl, 60 mM KCl, 340 mM sucrose, 0.15 mM spermine, 0.5 mM spermidine, 0.5 %
1288 Triton X-100, 1 mM NaF, 10 mM DTT. The standard sample (50 µL) was separated by a flow

1289 rate of 0.015 ml/min. Kav values for the standards were calculated. The calibration curve of
1290 Kav versus the logarithm of their molecular weights was determined as follows:

1291 $$K_{av} = \frac{Ve - Vo}{Vt - Vo}$$

1292 where Ve= elution volume of the protein

1293 Vo= column void volume = 0.8 mL

1294 Vt = total bed volume = 2.4 mL

1295 HeLa cell cytosolic and nuclear fractions were prepared as described above. For the gel
1296 filtration of the HeLa cell cytosol extraction sample, a 2.4-mL Superose 6 Increase 3.2/300
1297 column (Cytiva) was equilibrated using buffer comprising 15 mM pH 7.5 Tris, 15 mM NaCl, 60
1298 mM KCl, 340 mM sucrose, 0.15 mM spermine, 0.5 mM spermidine, 0.5 % Triton X-100, 1 mM
1299 NaF, 10 mM DTT. For the gel filtration of the HeLa cell nuclear fraction sample, a 2.4-ml
1300 Superose 6 Increase 3.2/300 column (Cytiva) was equilibrated using buffer comprising 50 mM
1301 Tris 7.5, 1 % NP-40, 150 mM NaCl, 1mM EDTA, 0.1 % SDS, 0.5 % sodium deoxycholate. The
1302 cytosolic and nuclear fractions (typically 1~3 mg/ml) were clarified by centrifugation for 15
1303 minutes at 12,000 X g before loading to the equilibrated gel filtration column. Samples were
1304 separated by a flow rate of 0.017 ml/min, and 50 µL fractions were collected for Western blot
1305 analysis (typically collects from 1.2mL to 2.4mL).

1306

1307 **LC-MS/MS analysis**
1308 MS grade Acetonitrile (ACN), MS grade H2O and MS grade formic acid (FA) were from
1309 ThermoFisher Scientific (Waltham, MA, USA). Sequencing-grade trypsin/Lys C mix was from
1310 Promega (Madison, WI, USA). Trifluoroacetic acid (TFA) and ammonium bicarbonate
1311 (NH4HCO3) were from Sigma-Aldrich (Saint-Louis, MO, USA).

1312 For sample preparation prior to LC-MS/MS analysis beads from immunoprecipitation
1313 experiments were incubated overnight at 37°C with 20 µL of 50 mM NH4HCO3 buffer
1314 containing 1 µg of sequencing-grade trypsin/Lys C mix. The digested peptides were loaded
1315 and desalted on evotips provided by Evosep (Odense, Denmark) according to manufacturer's
1316 procedure before LC-MS/MS analysis. For LC-MS/MS acquisition samples were analyzed on
1317 a timsTOF Pro 2 mass spectrometer (Bruker Daltonics, Bremen, Germany) coupled to an
1318 Evosep one system (Evosep, Odense, Denmark) operating with the 30SPD method developed
1319 by the manufacturer. Briefly, the method is based on a 44-min gradient and a total cycle time
1320 of 48 min with a C18 analytical column (0.15 x 150 mm, 1.9µm beads, ref EV-1106)
1321 equilibrated at 40°C and operated at a flow rate of 500 nL/min. H2O/0.1 % FA was used as
1322 solvent A and ACN/ 0.1 % FA as solvent B. The timsTOF Pro 2 was operated with a DIA-
1323 PASEF method comprising 12 pydiAID frames with 3 mass windows per frame resulting in a
1324 cycle time of 0.975 seconds as described in Bruker application note LCMS 218.

1325 For data analysis MS raw files were processed using Spectronaut 18 (Biognosys, Switzerland).
1326 Data were searched against the SwissProt Homo Sapiens database (downloaded 07 2023,
1327 20423 entries). Specific tryptic cleavages were selected and a maximum of 2 missed
1328 cleavages were allowed. The following post-translational modifications were considered for
1329 identification: Acetyl (Protein N-term) and Oxidation (M) as variables. Identifications were
1330 filtered based on a 1 % precursor and protein Qvalue cutoff threshold. The protein LFQ method
1331 was set to automatic and the quantity was set at the MS2 level with a cross-run normalization
1332 applied. Multivariate statistics on protein measurements were performed using Qlucore Omics
1333 Explorer 3.9 (Qlucore AB, Lund, SWEDEN). A positive threshold value of 1 was set to allow a
1334 log2 transformation of abundance data for normalization i.e. all abundance data values below

1335 the threshold are replaced by 1 before transformation. The transformed data were finally used
1336 for statistical analysis i.e. the evaluation of differentially present proteins between two groups
1337 using a bilateral Student's t-test. A p-value better than 0.05 was used to filter differential
1338 candidates.

1339

1340 **Experimental design, data acquisition and statistical analysis**
1341 All experiments were done in a strictly double-blinded manner. At least three independent
1342 biological replicates were performed for each experiment (unless otherwise indicated) and
1343 image quantifications were carried out in a blinded manner. Curves and graphs were made
1344 using GraphPad Prism and Adobe Illustrator software. Data was analyzed using one-sample
1345 two-tailed T-test or two sample unpaired two-tailed T-test (two-group comparison or folds
1346 increase relative to the control, respectively) or one-way ANOVA. A p-value less than 0.05
1347 (typically ≤ 0.05) was considered statistically significant and stars were assigned as follows:
1348 *P < 0.05, **P < 0.01, ***P < 0.001, ****P < 0.0001.
1349

Legends of Supplementary Table 1 and Supplementary Videos 1-10

Supplementary Table 1. List of reagents used for cloning, siRNA, and CRISPR/Cas9 methods

Table summarizes cloning primers, siRNAs and guide RNAs used in this study.

Supplementary Video 1. AL foci cluster following MT depolymerization

2xZFN-mEGFP-Nup107 HeLa cells treated with nocodazole were analyzed by live video spinning disk confocal microscopy. Z-stacks (10 mm range, 0.5 mm step) were acquired every 10 minutes and maximum intensity projection images are shown at speed 5 frames per second. A representative cell is depicted and selected representative frames of the movie are shown in the Fig. S5C.

Supplementary Video 2. AL foci merge with the NE throughout interphase

2xZFN-mEGFP-Nup107 HeLa cells were synchronized by double thymidine block, released and analyzed by live video spinning disc confocal microscopy. Timepoint 0 indicates the mitotic exit and entry into a new cell cycle. Z-stacks (10 mm range, 0.5 mm step) were acquired every 5 minutes and maximum intensity projection images are shown at speed 5 frames per second.

Supplementary Video 3. AL foci are highly dynamic under physiological conditions

2xZFN-mEGFP-Nup107 HeLa cells were analyzed by live video spinning disc confocal microscopy. Z-stacks (10 mm range, 1 mm step) were acquired every 1 second and maximum intensity projection images are shown at speed 5 frames per second. A representative cell is depicted and selected representative frames of the movie are shown in Fig. 2E.

Supplementary Video 4. Smaller AL foci fuse more quickly with the NE than larger AL

2xZFN-mEGFP-Nup107 HeLa cells were analyzed by live video spinning disc confocal microscopy. Z-stacks (10 mm range, 1 mm step) were acquired every 3 seconds and maximum intensity projection images are shown at speed 5 frames per second. Three representative cells are depicted and selected representative frames of the movie are shown in Fig. 2E.

Supplementary Video 5. AL occasionally undergo multiple cycles of detachment and re-attachment before ultimately fusing with the NE

2xZFN-mEGFP-Nup107 HeLa cells were analyzed by live video spinning disc confocal microscopy. Z-stacks (10 mm range, 1 mm step) were acquired every 3 seconds and maximum intensity projection images are shown at speed 5 frames per second. A representative cell is depicted and selected representative frames of the movie are shown in Fig. 2E.

Supplementary Video 6. NE-NPCs do not diffuse from the nuclear envelope into the cytoplasm.

mEos2-Nup133 HeLa cells were analyzed by live video spinning disc confocal microscopy. Nup133 on the nuclear envelope was converted from green fluorescence (left channel) to red fluorescence (right channel) by blue light for 30 seconds. Z-stacks (10 mm range, 1 mm step) were used. A 30-second acquisition pre-sequence with acquisition every 10 seconds in the green and red channels was performed. Two post sequences are carried out after acquisition, the first for 30 seconds with an interval every 10 seconds in order to quickly observe the effect of photoconversion and the second sequence for 12 hours every 15 minutes to see the effect over a longer period. The maximum intensity projection images are shown at 5 frames per second.

Supplementary Video 7. AL-NPCs accumulate at the nuclear envelope over time.

mEos2-Nup133 HeLa cells were analyzed by live video spinning disc confocal microscopy. Nup133 in the cytoplasm was converted from green fluorescence (left channel) to red fluorescence (right channel) by blue light for 30 seconds. Z-stacks (10 mm range, 1 mm step) were used. A 30-second acquisition pre-sequence with acquisition every 10 seconds in the green and red channels was performed. Two post sequences are carried out after acquisition, the first for 30 seconds with an interval every 10 seconds in order to quickly observe the effect

of photoconversion and the second sequence for 12 hours every 15 minutes to see the effect over a longer period. The maximum intensity projection images are shown at speed 5 frames per second.

Supplementary Video 8. AL foci move along ER to merge with the NE

2xZFN-mEGFP-Nup107 HeLa cells expressing ER marker plasmid mScarlet-ER were analyzed by live video spinning disk confocal microscopy. Timepoint 0 indicates the start of the imaging. Frames were acquired every 20s (without Z-stacks) and images are shown at 5 frames per second. A representative cell is depicted in Fig. 3D and a zoomed region of selected representative frames of the video is shown.

Supplementary Video 9. Microtubule depolymerization results in the inhibition of AL foci integration into the NE and their clustering

2xZFN-mEGFP-Nup107 HeLa cells expressing ER marker plasmid mScarlet-ER were analyzed by live video spinning disk confocal microscopy. Timepoint 0 indicates the start of the imaging. Frames were acquired every 120s (without Z-stacks) and images are shown at 5 frames per second. A representative cell is depicted in Fig. 3D and a zoomed region of selected representative frames of the video is shown.

Supplementary Video 10. AL are present on microtubules

2xZFN-mEGFP-Nup107 HeLa cells were analyzed by live video spinning disc confocal microscopy. SiR-tubulin was used to label microtubules. Z-stacks were acquired every 2 seconds and images are shown at 5 frames per second.

1424 **Figures and figure legends**

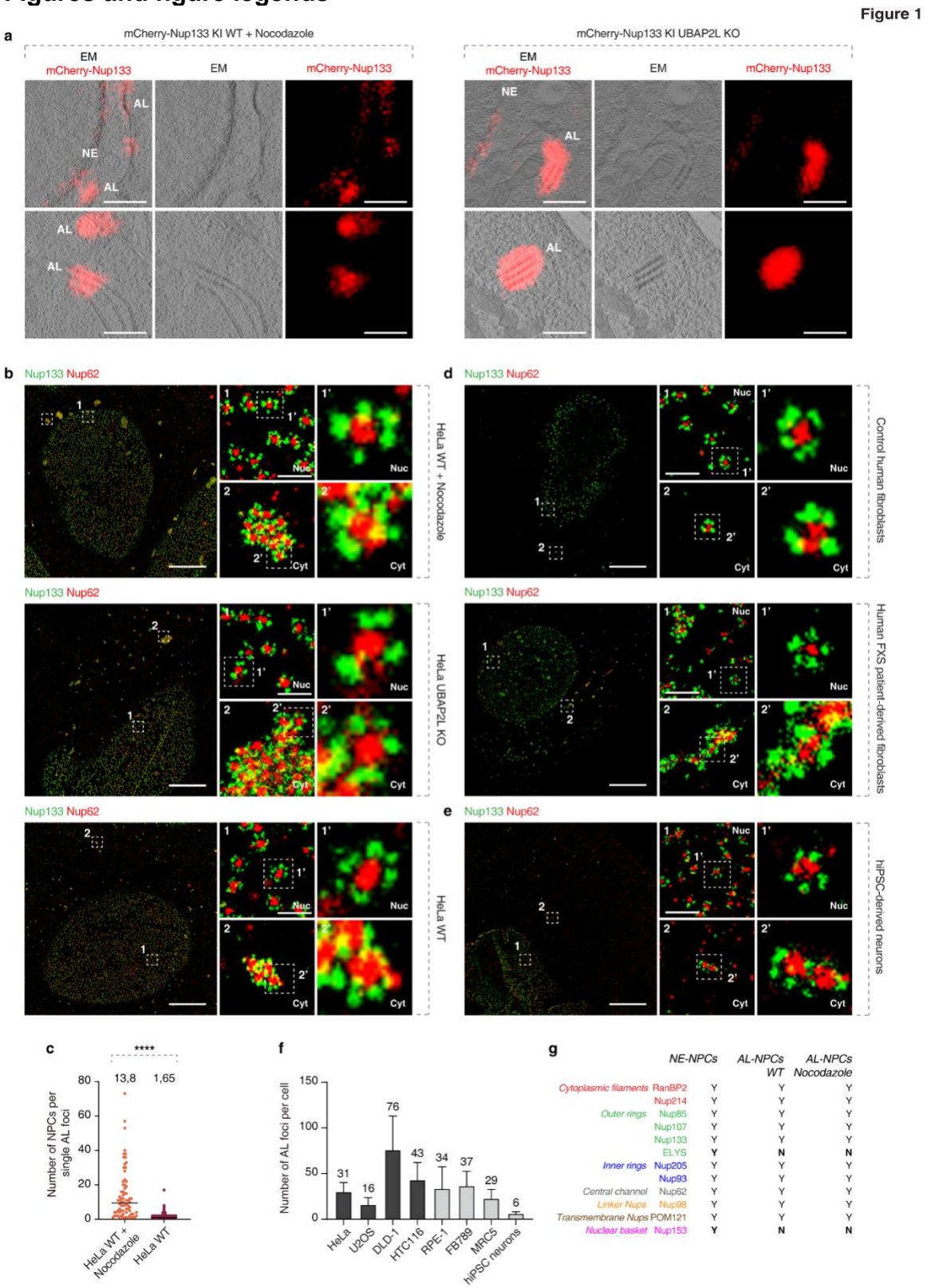

1425
1426 **Fig. 1. Single molecule localization microscopy identifies AL in somatic cells.**

1427 a, Representative correlative light and electron microscopy (CLEM) of HeLa cells. The left and
1428 right graphs represent the conditions of nocodazole treatment (10 μM, 90 min) and UBAP2L
1429 knockout (KO), respectively. mCherry fluorescence is concentrated at densely packed NPCs
1430 on stacked ER sheets in the cytoplasm corresponding to AL, and is also observed at NE. Scale
1431 bars, 1 μm.
1432 b, Representative splitSMLM images depicting NPCs on the nuclear (Nuc) surface and AL-
1433 NPCs located in the cytoplasm (Cyt) in HeLa cells treated with nocodazole (10 μM, 90 min),
1434 UBAP2L KO HeLa cells and in WT HeLa cells. Nup133 signal labels the cytoplasmic and
1435 nuclear rings of the NPC, the localization of the central channel is visualized by Nup62. Note
1436 that clusters of AL-NPCs in WT cells are smaller relative to other conditions. The magnified
1437 framed regions are shown in the corresponding numbered panels. Scale bars, 3 μm (entire
1438 nuclei), 0.3 μm (zoomed regions).
1439 c, The number of single AL-NPC complexes in individual AL foci/cluster were quantified. At
1440 least 6 cells per condition were analyzed (two sample unpaired T-test, mean ± SD, *P < 0.05;
1441 ****P < 0.0001;)
1442 d, Representative splitSMLM images depicting NPCs on the nuclear (Nuc) surface and AL-
1443 NPCs located in the cytoplasm (Cyt) in normal human fibroblasts and in FXS patient-derived
1444 fibroblasts. The magnified framed regions are shown in the corresponding numbered panels.
1445 Scale bars, 3 μm (entire nuclei), 0.3 μm (zoomed regions).
1446 e, Representative splitSMLM images depicting NPCs on the nuclear (Nuc) surface and AL-
1447 NPCs located in the cytoplasm (Cyt) in hiPSC-derived neurons. The magnified framed regions
1448 are shown in the corresponding numbered panels. Scale bars, 3 μm (entire nuclei), 0.3 μm
1449 (zoomed regions).
1450 f, The number of AL-foci in individual cells in representative cancer cell lines (dark gray) and
1451 non-transformed cell lines (light grey) were quantified. At least 25 cells per cell line were
1452 analyzed.
1453 g, Summary of composition of NE-NPCs and AL-NPCs. Different colors represent specific
1454 NPC subcomplexes. “Y” indicates presence and “N” indicates absence of indicated Nups.

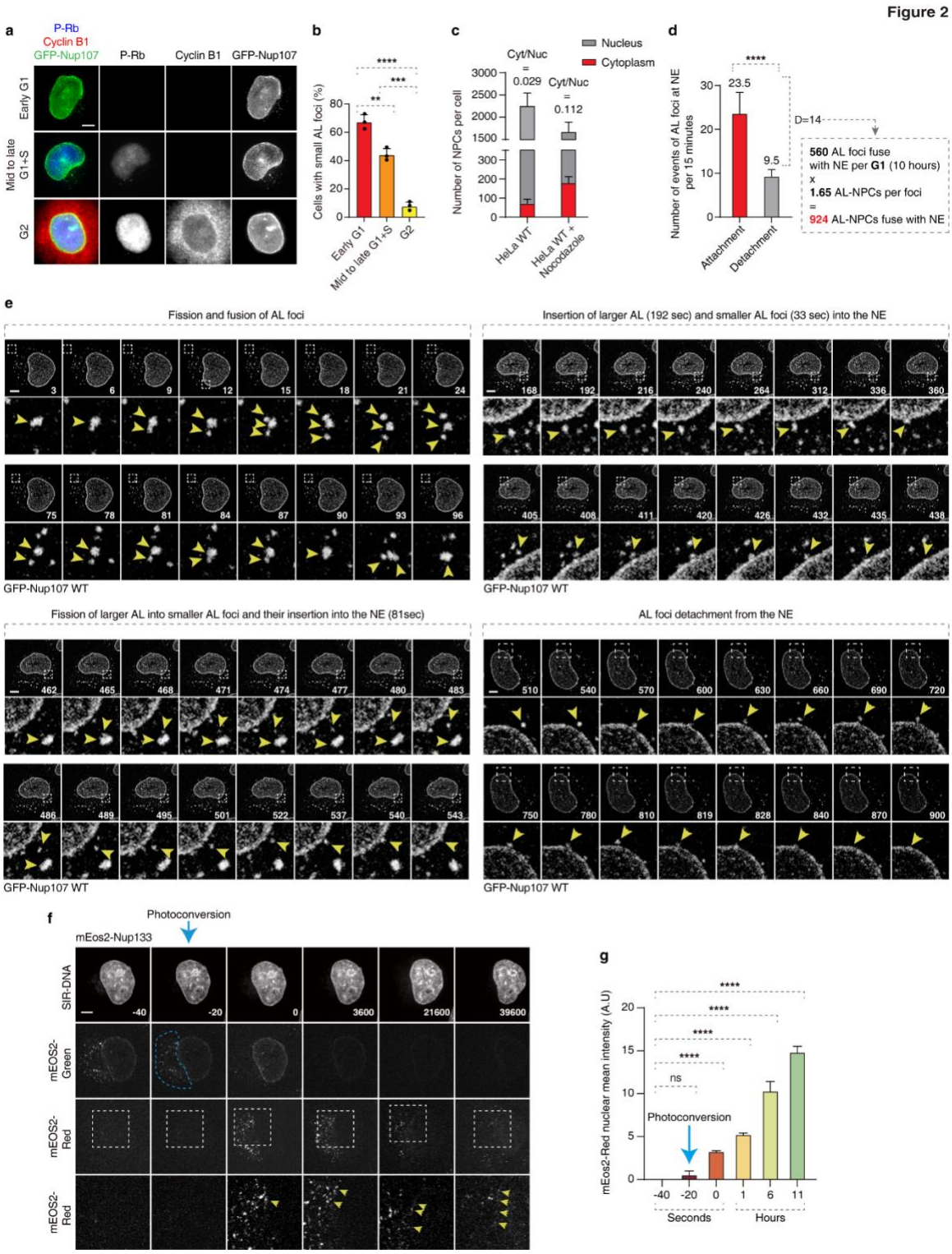

Fig. 2. AL are inserted into NE during G1.

a, b, Representative images of asynchronously proliferating 2xZFN-mEGFP-Nup107 HeLa cells co-labelled with anti-p-Rb (blue) and anti-cyclin B1 (red) antibodies (a). The percentage of cells with Nup foci in p-Rb and cyclin B1 negative cells (early G1), p-Rb positive and cyclin B1 negative cells (mid to late G1+S), and p-Rb and cyclin B1 positive cells (G2) was quantified

in (b), and at least 200 cells per condition were analyzed (one-Way ANOVA test, mean ± SD, **P < 0.01; ***P < 0.001; ****P < 0.0001; N = 3). Scale bars, 5 µm.

c, The number of NPCs in cytoplasm and nucleus of individual cells were quantified. At least 6 cells per condition were analyzed (mean ± SD)

d, e, Dynamics of AL-foci in 2xZFN-mEGFP-Nup107 HeLa cells in G1 phase were analyzed by live video spinning disk confocal microscopy. Selected representative frames of the videos are depicted, and time is shown in seconds. The magnified framed regions are shown in the lower panels. Yellow arrowheads point to the movement of cytosolic AL-NPCs. Scale bars, 5 µm. The attachment and detachment events of AL foci to the NE were quantified in (d). At least 6 cells per condition were analyzed (two sample unpaired T-test, mean ± SD, ****P < 0.0001)

f, g, The photoconversion of Nup foci in mEOS2-Nup133 HeLa cells were analyzed by live video spinning disk confocal microscopy. The selected representative frames of the Videos are depicted, and time is shown in seconds. The magnified framed regions of mEOS2-Red are shown in the lower panels. The blue dashed box indicates the photoconversion region, where mEOS2-Nups convert from a green to a red fluorescent state. Yellow arrowheads point to the accumulation of AL-Nup 133 at the NE. Scale bars, 5 µm. The average intensity of mEos2-Red in the nucleus at the indicated time were quantified in (g). At least 5 cells per condition were analyzed (one-Way ANOVA test, mean ± SD, ns: not significant, ****P < 0.0001)

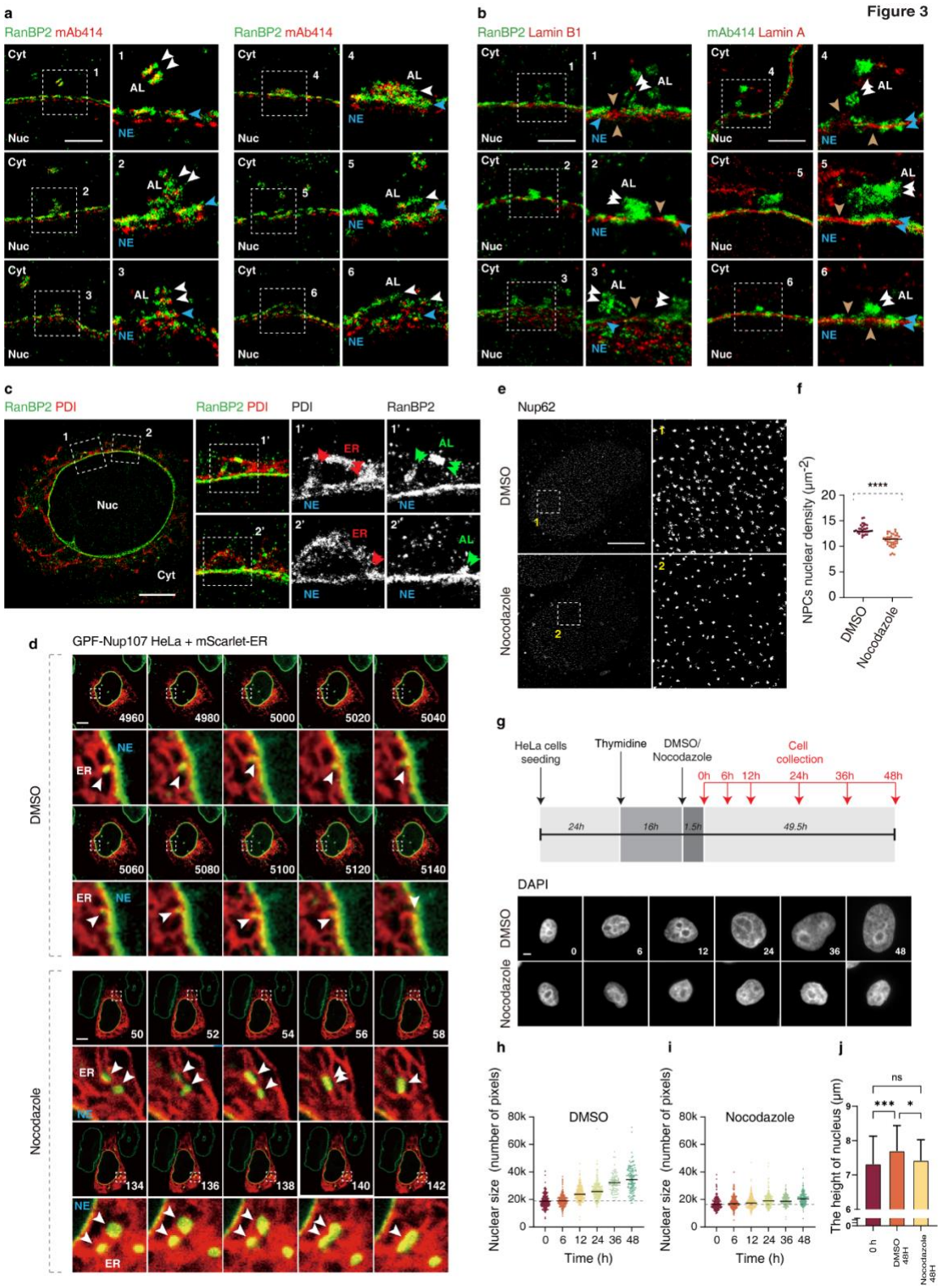

Fig. 3. AL-NPC insertion into the NE through NE-ER contacts supports nuclear expansion and pore formation.

a, Representative splitSMLM images depicting the nuclear (Nuc) surface and cytoplasm (Cyt) from the side view of WT HeLa cells. Central channel, cytoplasmic filaments and Nucleus

1484 basket of NPCs is labelled with mAb414 antibodies and RanBP2 antibody labels NPC
1485 cytoplasmic filaments. The magnified framed regions are shown in the corresponding
1486 numbered panels. White arrowheads point out to AL-NPC structures within AL where NPC
1487 cytoplasmic filaments are located symmetrically and blue arrowheads indicate asymmetric NE-
1488 NPCs on the nuclear envelope (NE) (panel 1). Note lateral fusion events of AL-NPCs with NE-
1489 NPCs from the cytoplasmic side (panels 2-4) and NE-openings where both AL-NPCs and NE-
1490 NPCs can be located (panels 5-6). Scale bars, 1 μm.

1491 b, Representative splitSMLM images depicting the nuclear (Nuc) surface and cytoplasm (Cyt)
1492 from the side view of WT HeLa cells. RanBP2 antibody labels NPC cytoplasmic filaments,
1493 Lamin B1 and Lamin A label NE-associated factors. Central channel, cytoplasmic filaments
1494 and nuclear basket of NPCs are labelled with mAb414 antibodies. The magnified framed
1495 regions are shown in the corresponding numbered panels. White arrowheads point out to AL-
1496 NPC structures within AL where NPC cytoplasmic filaments are located symmetrically and
1497 blue arrowheads indicate asymmetric NE-NPCs on the nuclear envelope (NE). Brown arrows
1498 indicate NE-openings where NE-associated factors remain intact. Scale bars, 1 μm.

1499 c, Representative splitSMLM images depicting the nuclear (Nuc) surface and cytoplasm (Cyt)
1500 from the side view of WT HeLa cells. RanBP2 antibody labels NPC cytoplasmic filaments and
1501 PDI labels ER. The magnified framed regions are shown in the corresponding numbered
1502 panels. Red arrows point out to ER, and green arrows indicate AL-NPCs. Scale bars, 3 μm.

1503 d, 2xZFN-mEGFP-Nup107 HeLa cells expressing ER marker plasmid mScarlet-ER were
1504 analyzed by live video spinning disk confocal microscopy. The selected representative frames
1505 of the Videos are depicted, and time is shown in seconds. The magnified framed regions are
1506 shown in the lower panels. White arrowheads point to the movement of cytosolic AL-NPC foci
1507 along the ER and their incorporation into the NE along the junction of the ER and the NE.
1508 Scale bars, 5 μm.

1509 e, f, Representative SMLM immunofluorescence images of Nup62 at the nuclear surface in
1510 DMSO or nocodazole treated (10 μM, 90 min) HeLa cells. The magnified framed regions are
1511 shown in the right panels (e). The nuclear density of NE-NPCs (Nup62) in cells was quantified
1512 in (f) (two sample unpaired T-test, mean ± SD, ****$P < 0.0001$, unpaired two-tailed t test; 40
1513 cells were counted per cell line). Scale bars, 5 μm

1514 g-j, Scheme of the experimental setup (g). HeLa cells were synchronized and arrested at S
1515 phase by thymidine treatment (16h), treated with nocodazole (10 μM) and fixed and collected
1516 at indicated time points. Representative images of cell nuclei are shown in (g) and the nuclear
1517 size was quantified in (h, i). The height of nucleus was quantified in (h, i). About the nuclear
1518 size, at least 200 cells per condition were analyzed (N = 3). About the height of nucleus, at
1519 least 80 cells per condition were analyzed (N = 3). Scale bars, 5 μm.

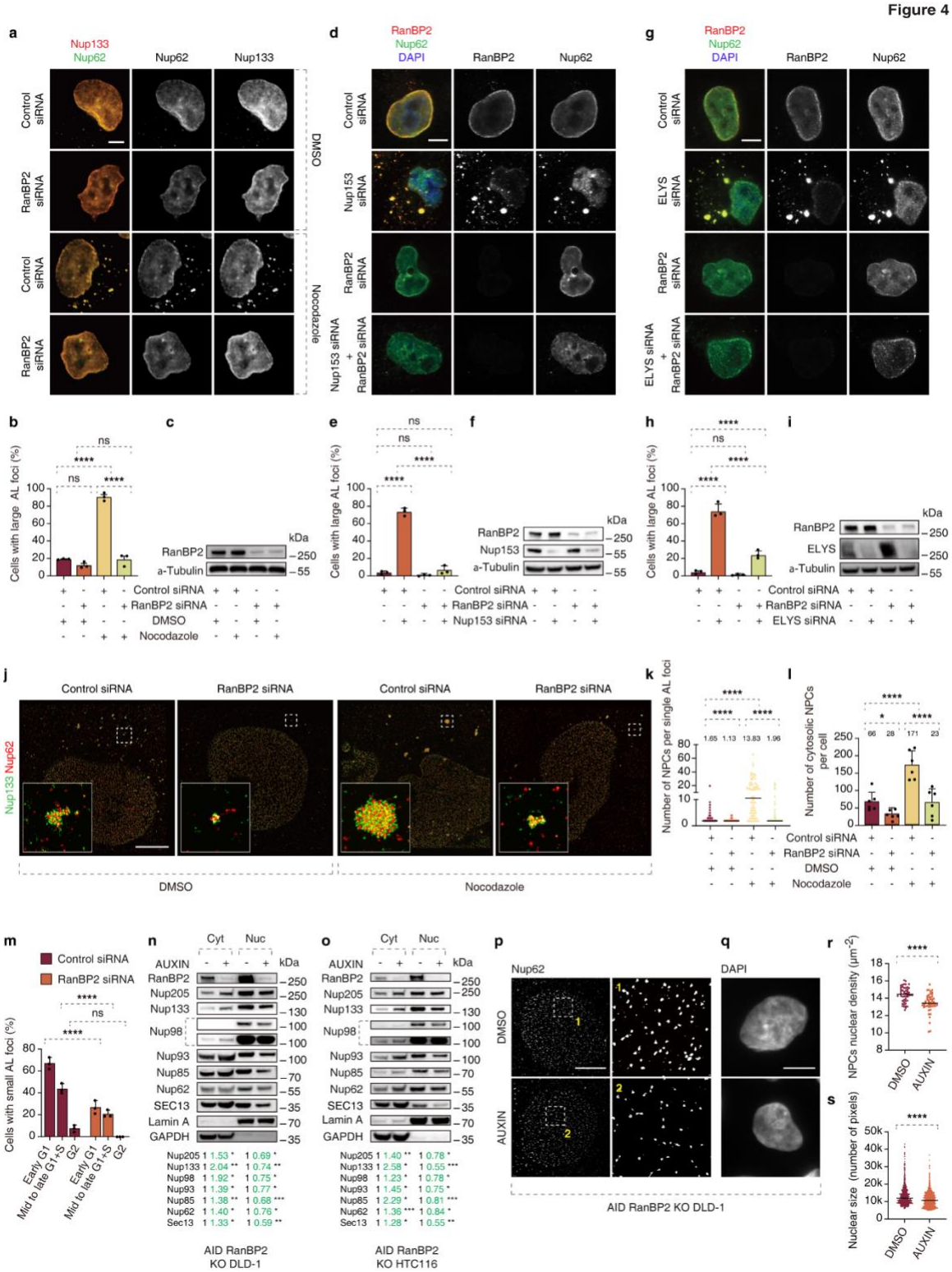

Fig. 4. RanBP2 is required for AL clustering, AL biogenesis and for nuclear pore formation.

a-c, Representative images of HeLa cells treated with the indicated siRNAs (48h) and subsequently by nocodazole (10 μM) or DMSO (90 min). Cells were co-labelled with anti-Nup62 (green) and anti-Nup133 (red) antibodies (a) to detect AL-NPC foci. The number of

1526 cells with big AL foci were quantified in (b), and at least 1000 cells per condition were analyzed
1527 (one-Way ANOVA test, mean ± SD, ns: not significant, ****P < 0.0001; N = 3). Scale bars, 5
1528 μm. (c) shows the Western blot analysis.

1529 d-f, Representative images of HeLa cells treated with the indicated siRNAs (48h). Cells were
1530 co-labelled with anti-Nup62 (green) and anti-RanBP2 (red) antibodies (d) to detect AL-NPC
1531 foci. The percentage of cells with big AL foci was quantified in (e), and at least 300 cells per
1532 condition were analyzed (one-Way ANOVA test, mean ± SD, ns: not significant, **P < 0.01;
1533 ****P < 0.0001; N = 3). Scale bars, 5 μm. (f) shows the Western blot analysis.

1534 g-l, Representative images of HeLa cells treated with the indicated siRNAs (48h). Cells were
1535 co-labelled with anti-Nup62 (green) and anti-RanBP2 (red) antibodies (g) to detect AL-NPC
1536 foci. The percentage of cells with big AL foci were quantified in (h), and at least 300 cells per
1537 condition were analyzed (one-Way ANOVA test, mean ± SD, ns: not significant, **P < 0.01;
1538 ****P < 0.0001; N = 3). Scale bars, 5 μm. (i) shows the Western blot analysis.

1539 j-l, Representative splitSMLM images of HeLa cells treated with the indicated siRNAs (48h)
1540 and subsequently by nocodazole (10 μM) or DMSO (90 min) depicting AL-NPCs in the
1541 cytoplasm. Cells were co-labelled with anti-Nup62 (green) and anti-Nup133 (red) antibodies
1542 (j). The magnified framed regions are shown in the lower left corner. The number of single AL-
1543 NPC complexes per cell and the number of single AL-NPC complexes in individual AL
1544 foci/cluster were quantified in (k, l), respectively. At least 6 cells per condition were analyzed
1545 (one-Way ANOVA test, mean ± SD, *P < 0.05; ****P < 0.0001; N = 3). Scale bars, 3 μm.

1546 m, Asynchronously proliferating 2xZFN-mEGFP-Nup107 HeLa cells treated with the indicated
1547 siRNAs (48h) and co-labelled with anti-P-Rb (blue) and anti-cyclin B1 (red) antibodies. The
1548 percentage of cells with small AL foci in P-Rb and cyclin B1 negative cells (early G1), P-Rb
1549 positive and cyclin B1 negative cells (mid to late G1+S), and P-Rb and cyclin B1 positive cells
1550 (G2) was quantified in (m), and at least 200 cells per condition were analyzed (one-Way
1551 ANOVA test, mean ± SD, ****P < 0.0001; N = 3). Representative images are shown in
1552 Extended Data Fig. 11a.

1553 n, o, Auxin-inducible degron (AID) RanBP2 KO DLD-1 cells (n) and HTC116 cells(o) were
1554 treated with DMSO or auxin for 4h to deplete RanBP2. Cytoplasmic (Cyt) and nuclear (Nuc)
1555 fractions were prepared and levels of Nups were analyzed by Western blot (at least 3
1556 independent experiments). Signal intensities were quantified; signals in the cytoplasm and
1557 nucleus were normalized according to GAPDH and Lamin A. A mean value is shown below
1558 the image (*P < 0.05, **P < 0.01, ***P < 0.001, paired one-tailed t-test; n = 3 independent
1559 experiments).

1560 p, r, Representative SMLM immunofluorescence images of Nup62 at the nuclear surface in
1561 AID RanBP2 KO DLD-1 cells treated with DMSO or auxin for 4h to deplete RanBP2. The
1562 magnified framed regions are shown in the right panels (p). The nuclear density of NPCs
1563 (Nup62) in cells was quantified in (r) (mean ± SD, ****P < 0.0001, unpaired two-tailed t test;
1564 counted 50 cells per cell line). Scale bars, 5 μm

1565 q, s, Representative images of cell nuclei in AID RanBP2 KO DLD-1 cells treated with DMSO
1566 or auxin for 4h to deplete RanBP2 are shown in (q) and the nuclear size was quantified in (s).
1567 At least 700 cells per condition were analyzed (mean ± SD, ****P < 0.0001, unpaired two-tailed
1568 t test; N = 3). Scale bars, 5 μm.

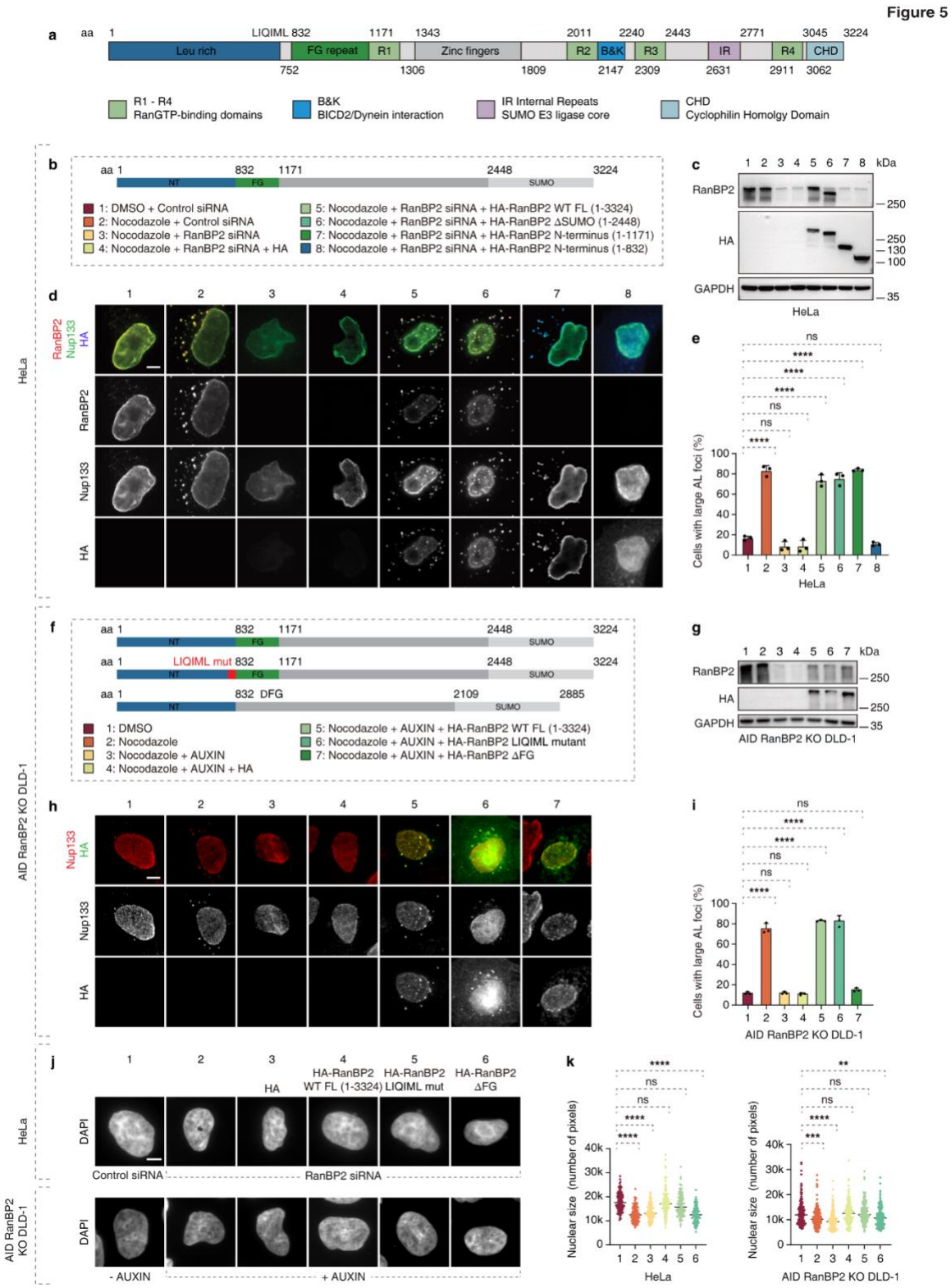

Fig. 5. RanBP2 is specifically required for AL clustering and biogenesis through its N-terminal FG repeat region.

a, shows the scheme of domain organization of RanBP2 protein.

1573 b-e, Rescue experiments using different RanBP2 protein fragments (b). (c) shows the Western
1574 blot analysis and (d) shows representative images of HeLa cells treated with the indicated
1575 siRNAs, transfected with different RanBP2 fragments (indicated by numbers in the schematic
1576 diagram) and treated with nocodazole (10 μM) or DMSO (90 min). Cells were co-labelled with
1577 anti-Nup133 (green), anti-RanBP2 (red) and anti-HA (blue) antibodies. The number of cells
1578 with large AL foci was quantified in (e), and at least 300 cells per condition were analyzed
1579 (one-Way ANOVA test, mean ± SD, ns: not significant, ****P < 0.0001; N = 3). Scale bars, 5
1580 μm.

1581 f-i, Rescue experiments using different FL RanBP2 mutated versions (f). (g) Shows the
1582 Western blot analysis of RanBP2 version under different indicated conditions (numbers in the
1583 schematic diagram). (h) shows representative images of AID-RanBP2 KO DLD-1 cells treated
1584 with DMSO or Auxin, transfected with different RanBP2 versions and treated with nocodazole
1585 (10 μM) or DMSO (90 min). Cells were co-labelled with anti-Nup133 (red) and anti-HA (green)
1586 antibodies. The number of cells with large AL foci was quantified in (i), and at least 300 cells
1587 per condition were analyzed (one-Way ANOVA test, mean ± SD, ns: not significant, *P < 0.05;
1588 **P < 0.01; ****P < 0.0001; N = 3). Scale bars, 5 μm.

1589 j, k, Representative images of cell nuclei in HeLa cells and AID RanBP2 KO DLD-1 cells are
1590 shown in (j). Cells were treated with RanBP2 siRNA or Auxin to deplete RanBP2, and then
1591 rescued using different RanBP2 versions. Schematic diagram of RanBP2 versions and
1592 Western blot analysis are shown in Fig S12J-L. The nuclear size was quantified in (k). At least
1593 120 Cell (HeLa) or 150 cells (DLD-1) per condition were analyzed (one-Way ANOVA test,
1594 mean ± SD, ns: not significant, **P < 0.01; ***P < 0.001, ****P < 0.0001; N = 3). Scale bars, 5
1595 μm.

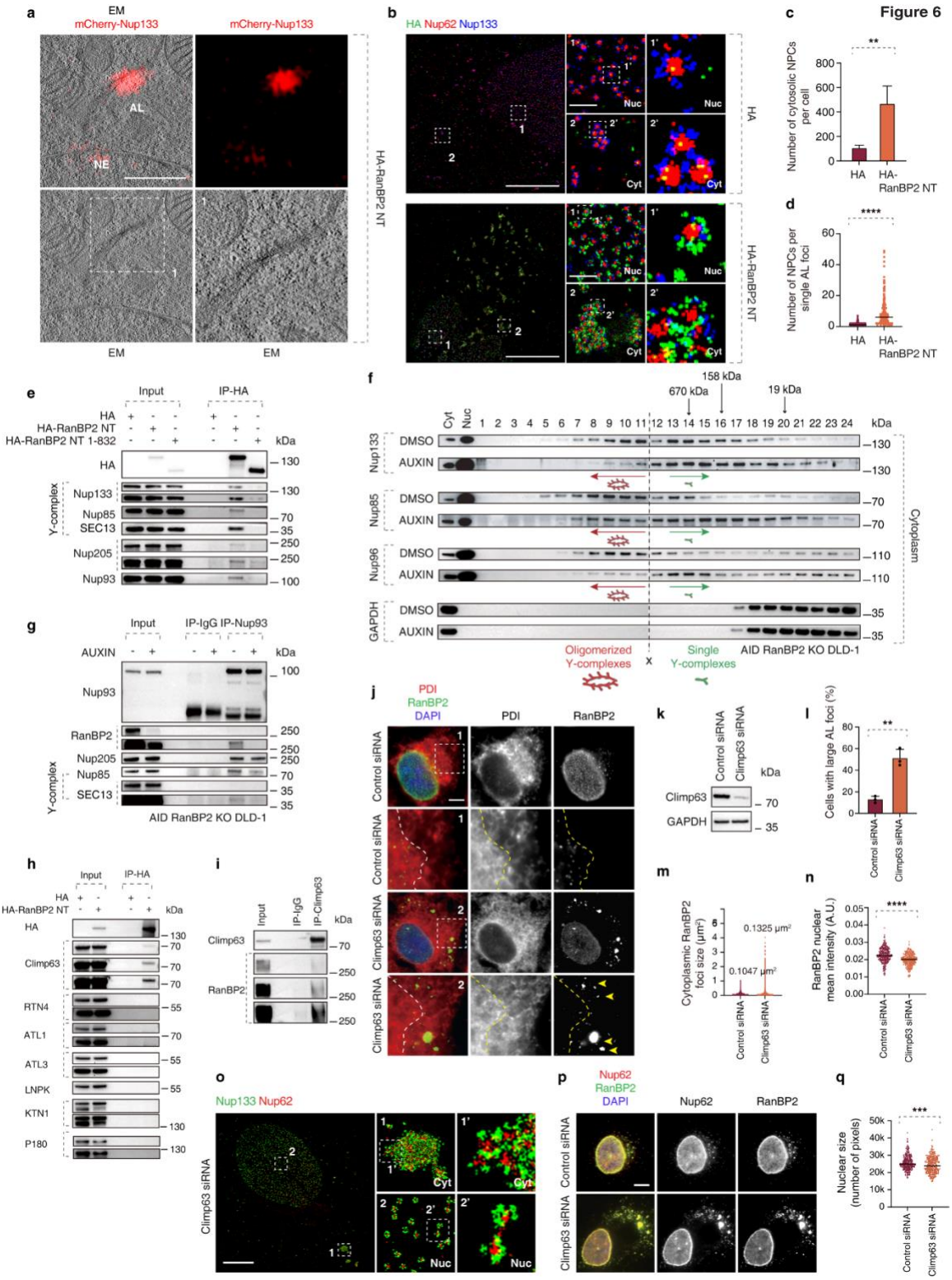

Fig. 6. RanBP2 drives oligomerization of AL-NPCs and interacts with Climp63 that localizes AL-NPCs to ER sheets.

a, Representative correlative light and electron microscopy (CLEM) of mCherry-Nup133-KI HeLa cells transfected with HA-RanBP2-NT fragment. The magnified framed regions are

1601 shown in the corresponding numbered panels. mCherry fluorescence is concentrated at
1602 densely packed AL-NPCs on stacked ER sheets in the cytoplasm, representing AL and is also
1603 observed at the NE. Scale bars, 1 µm.

1604 b-d, Representative splitSMLM images depicting NPCs on the nuclear surface (Nuc) and AL-
1605 NPCs in the cytoplasm (Cyt) in HeLa cells transfected with HA or HA-RanBP2-NT fragment.
1606 Nup133 signal labels the cytoplasmic and nuclear rings of the NPC and the localization of the
1607 central channel is visualized by Nup62. The magnified framed regions are shown in the
1608 corresponding numbered panels (b). The number of single AL-NPC complexes per cell and
1609 the number of single AL-NPC complexes in a single AL foci/cluster were quantified in (c, d),
1610 respectively. At least 6 cells per condition were analyzed (two sample unpaired T-test, mean
1611 ± SD, ***P < 0.001; ****P < 0.0001; N = 3). Scale bars, 3 µm, 0.3 µm (zoomed-in).

1612 e, Lysates of HeLa cells expressing HA, HA-RanBP2-NT or HA-RanBP2-NT ΔFG were
1613 immunoprecipitated using anti-HA magnetic beads (HA-IP) and analyzed by Western blot (at
1614 least 3 independent experiments).

1615 f, Auxin-inducible degron (AID) RanBP2 KO DLD-1 cells were treated with DMSO or Auxin for
1616 4h to deplete RanBP2 and cytoplasmic fractions were prepared, separated on a Superose 6
1617 gel filtration column and analyzed by Western blotting (at least 3 independent experiments).
1618 Fraction 1 corresponds to the void and the elution of thyroglobulin (670 kDa), g-globulin (158
1619 kDa) and myoglobulin markers 19 kDa are indicated. Green arrows point to fractions
1620 preferentially containing single Y-complexes, and red arrows indicate fractions with higher
1621 molecular weight, oligomerized Y-complexes. Note that depletion of RanBP2 reduced the
1622 abundance of oligomerized Y-complexes (at least 3 independent experiments).

1623 g, Auxin-inducible degron (AID) RanBP2 KO DLD-1 cells were treated with Auxin for 4h to
1624 deplete RanBP2 and lysates were immunoprecipitated using Nup93 antibody or IgG and
1625 analyzed by Western blot (at least 3 independent experiments).

1626 h, Lysates of HeLa cells expressing HA or HA-RanBP2-NT were immunoprecipitated using
1627 anti-HA magnetic beads (HA-IP) and analyzed by Western blot (at least 3 independent
1628 experiments).

1629 i, Lysates of HeLa cells were immunoprecipitated using Climp63 antibody or IgG and analyzed
1630 by Western blot (at least 3 independent experiments).

1631 j-n, Representative images of HeLa cells treated with the indicated siRNAs and analyzed by
1632 Western blot (k). Cells were co-labelled with anti-RanBP2 (green) and anti-PDI (red) antibodies
1633 (j). The magnified framed regions are shown in the corresponding numbered panels. The
1634 dotted line separates the cytoplasmic area with ER sheets proximal to the nuclei where AL-
1635 NPCs are enriched in WT cells. Note that AL-NPCs foci enlarge and are localized more distally
1636 upon Climp63 downregulation. The number of cells with large AL foci were quantified in (l)
1637 where at least 400 cells per condition were analyzed (two sample unpaired T-test, mean ± SD,
1638 ns: not significant, ****P < 0.0001; N = 3). The size of cytoplasmic AL foci was quantified in (m)
1639 where at least 3500 foci per condition were analyzed (N = 3). The NE intensity of RanBP2 was
1640 quantified in (n), where at least 280 cells per condition were analyzed (two sample unpaired
1641 T-test, mean ± SD, ns: not significant, ****P < 0.0001; N = 3). Scale bars, 5 µm.

1642 o, Representative splitSMLM images depicting NPCs on the nuclear (Nuc) surface and AL-
1643 NPCs located in the cytoplasm (Cyt) in HeLa cells treated with Climp63 siRNA. Nup133 signal
1644 labels the cytoplasmic and nuclear rings of the NPC, the localization of the central channel is
1645 visualized by Nup62. The magnified framed regions are shown in the corresponding numbered
1646 panels. Scale bars, 3 µm.

1647 p, q, Representative images of HeLa cells treated with the indicated siRNAs. Cells were co-
1648 labelled with anti-RanBP2 (green) anti-Nup62(red) antibodies and DAPI (p). The size of

1649 nucleus was quantified in (q) where at least 300 cells per condition were analyzed (mean ±
1650 SD, ***P < 0.001, unpaired two-tailed t test; N = 3). Scale bars, 5 μm.

1651

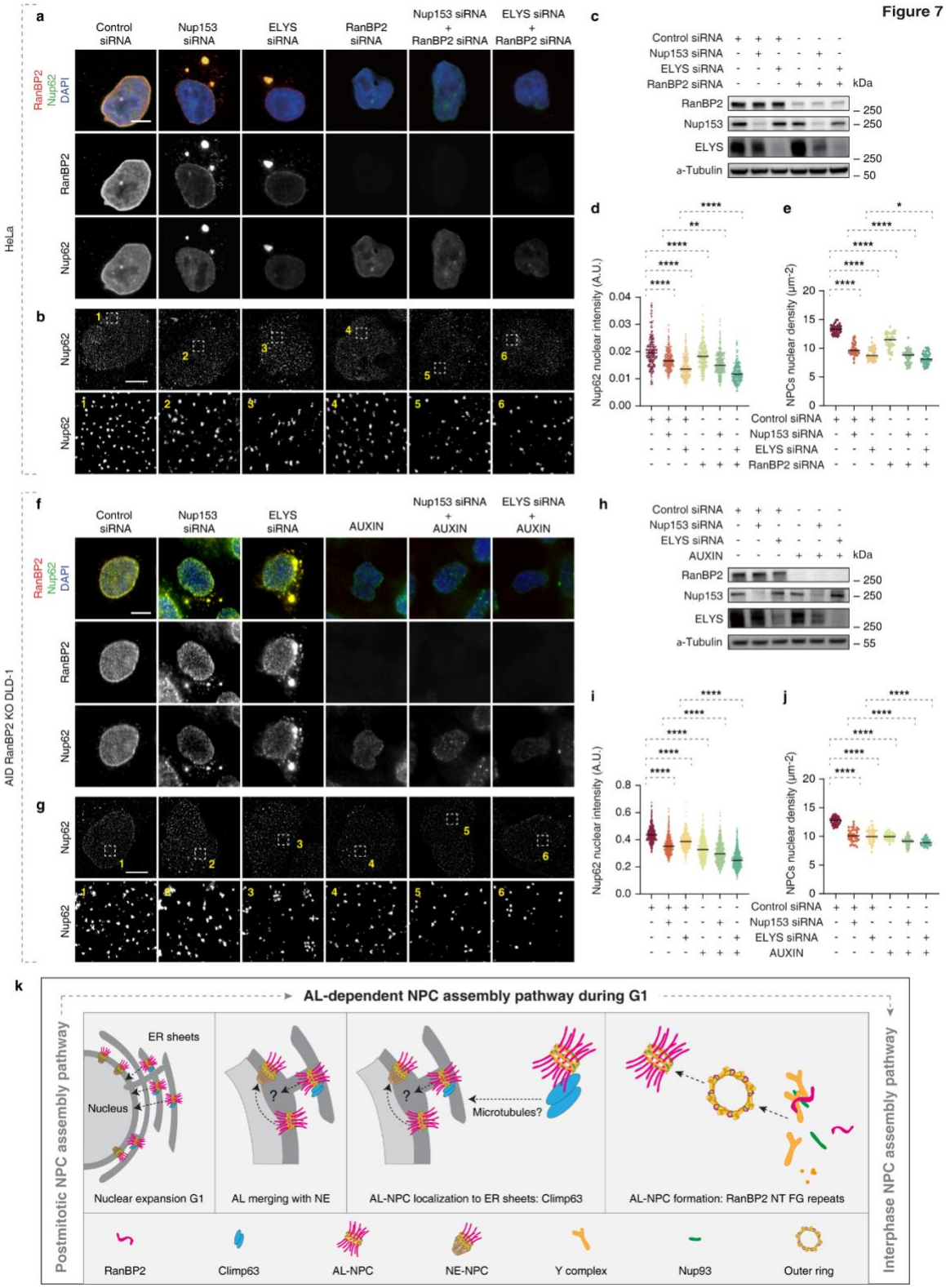

Fig. 7. AL-dependent NPC assembly is additive to canonical nuclear pore assembly pathways.

1656 a-e, Representative images of HeLa cells treated with the indicated siRNAs (48h). Cells were
1657 co-labelled with anti-Nup62 (green) and anti-RanBP2 (red) antibodies (a) for
1658 immunofluorescence microscopy or labelled with anti-Nup62 for SMLM immunofluorescence
1659 (b). (c) Samples from indicated conditions were analyzed by Western blot. The intensity of
1660 Nup62 in the NE was quantified in (d), and at least 200 cell per condition were analyzed (one-
1661 Way ANOVA test, mean ± SD, **P < 0.01; ****P < 0.0001; N = 3). Scale bars, 5 µm. The
1662 nuclear density of NPCs (Nup62) in cells was quantified in (e) (one-Way ANOVA test, mean ±
1663 SD, P < 0.05; ****P < 0.0001; counted 50 cells per cell line). Scale bars, IF, 5 µm; SMLM, 3
1664 µm.

1665 f-j, Representative images of Auxin-inducible degron (AID) RanBP2 KO DLD-1 cells treated
1666 with the Auxin or indicated siRNAs (48h). Cells were co-labelled with anti-Nup62 (green) and
1667 anti-RanBP2 (red) antibodies (f) for immunofluorescence microscopy or labelled with anti-
1668 Nup62 for SMLM immunofluorescence (g). (h) Samples from indicated conditions were
1669 analyzed by Western blot. The intensity of Nup62 in the NE was quantified in (i), and at least
1670 200 cell per condition were analyzed (one-Way ANOVA test, mean ± SD, ****P < 0.0001; N =
1671 3). Scale bars, 5 µm. The nuclear density of NPCs (Nup62) in cells was quantified in (j) (one-
1672 Way ANOVA test, mean ± SD, ****P < 0.0001; counted 50 cells per cell line). Scale bars, IF,
1673 5 µm; SMLM, 3 µm.

1674 k. A hypothetical model depicting the universal function and direct biogenesis mechanisms of
1675 Annulate Lamellae (AL). AL containing few AL-NPCs are present in the cytoplasm in normally
1676 proliferating somatic cells and play a crucial role in supplying the NE with new nuclear pores.
1677 This function is essential for nucleocytoplasmic transport and for nuclear expansion during the
1678 G1 phase of the cell cycle. AL-NPCs on ER membranes can fuse with NE-NPCs to become
1679 incorporated into NE during G1 and possibly remodeled to NE-NPCs. The N-terminal part of
1680 RanBP2 is required for the formation of AL-NPCs in the cytosol across cellular models and
1681 conditions. It ensures oligomerization of NPC scaffold components (Y-complexes) specifically
1682 in the cytoplasm. Climp63 drives the insertion of pre-made AL-NPCs into ER sheets which are
1683 more proximal to the NE. This mechanism is crucial for AL merging with the NE and for nuclear
1684 expansion and constitutes a distinct NPC assembly pathway during G1 phase of normal cell
1685 cycle.

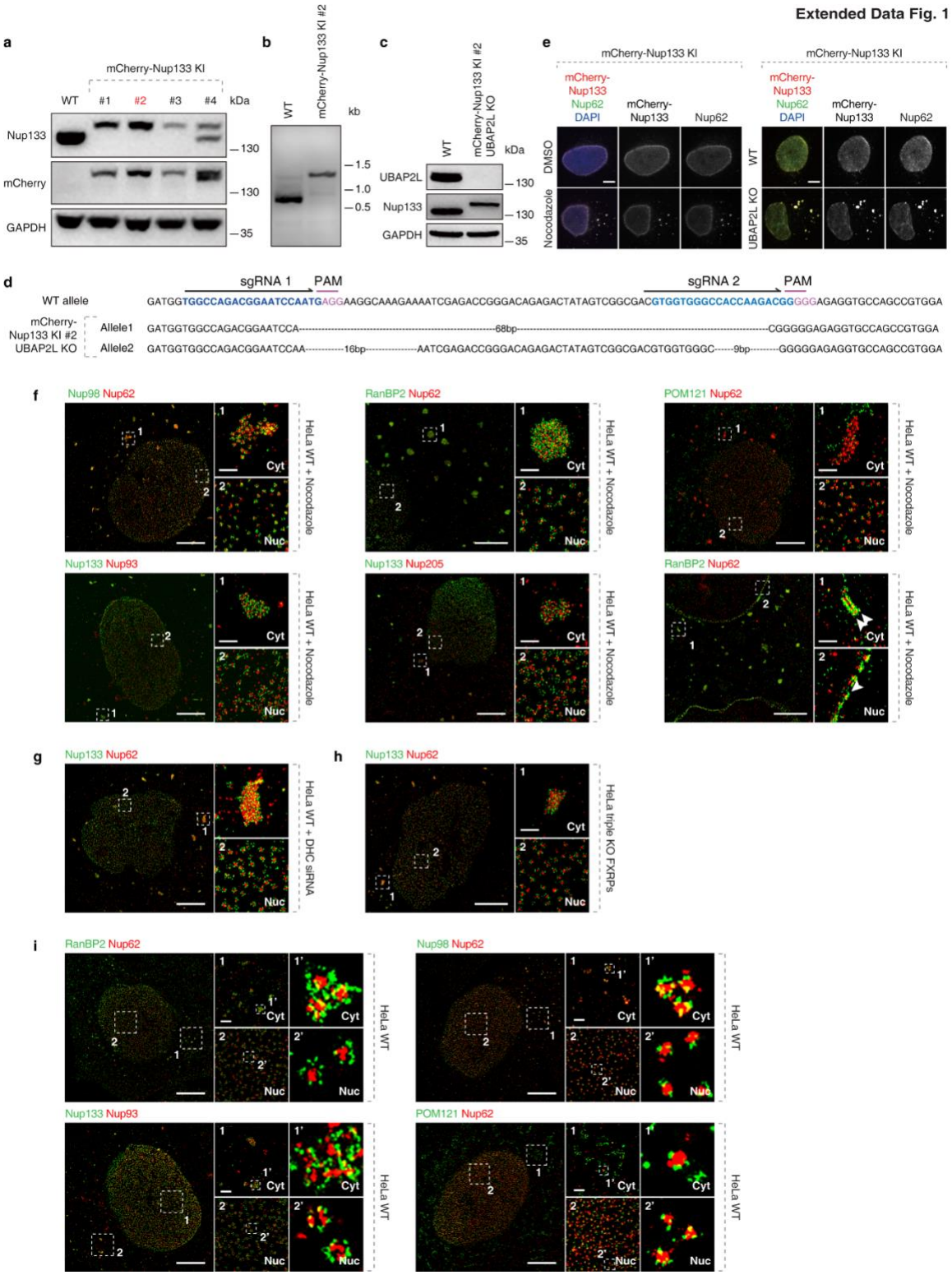

Extended Data Fig.1. Single molecule localization microscopy identifies AL in WT and in challenged HeLa cells.

a, b, Validation of CRISPR/Cas9-mediated mCherry-Nup133 KI Hela cell clones by Western blot (a) and PCR (b).

1692 c,d, Validation of CRISPR/Cas9-mediated UBAP2L KO mCherry-Nup133 KI HeLa cell clones
1693 by Western blot (c) and Sanger sequencing (d).

1694 e, Representative images of mCherry-Nup133 KI HeLa cells treated with DMSO or
1695 Nocodazole (10 μM) and representative images of UBAP2L KO mCherry-Nup133 KI HeLa.
1696 Cells were co-labelled with DAPI (blue), and anti-Nup62 (green) antibody. Scale bars, 5 μm.

1697 f, Representative splitSMLM images depicting NPCs on the nuclear (Nuc) surface and AL-
1698 NPCs in the cytoplasm (Cyt) in nocodazole-treated (10 μM, 90 min) HeLa cells. Analyzed Nups
1699 from different NPC subcomplexes are indicated above each panel. The magnified framed
1700 regions are shown in the corresponding numbered panels. Scale bars, 3 μm (entire nuclei),
1701 0.3 μm (zoomed regions).

1702 g, h, Representative splitSMLM images depicting NPCs on the nuclear (Nuc) surface and AL-
1703 NPCs in the cytoplasm (Cyt) in HeLa cell treated with the dynein heavy chain siRNAs (48h)
1704 and triple knock-out of FXRPs HeLa cells. Nup133 signal labels the cytoplasmic and nuclear
1705 rings of the NPC and the localization of the central channel is visualized by Nup62. The
1706 magnified framed regions are shown in the corresponding numbered panels. Scale bars, 3 μm
1707 (entire nuclei), 0.3 μm (zoomed regions).

1708 i, Representative splitSMLM images depicting NPCs on the nuclear (Nuc) surface and AL-
1709 NPCs in the cytoplasm (Cyt) in WT HeLa cells. Analyzed Nups from different NPC
1710 subcomplexes are indicated above each panel. The magnified framed regions are shown in
1711 the corresponding numbered panels. Scale bars, 3 μm (entire nuclei), 0.3 μm (zoomed
1712 regions).

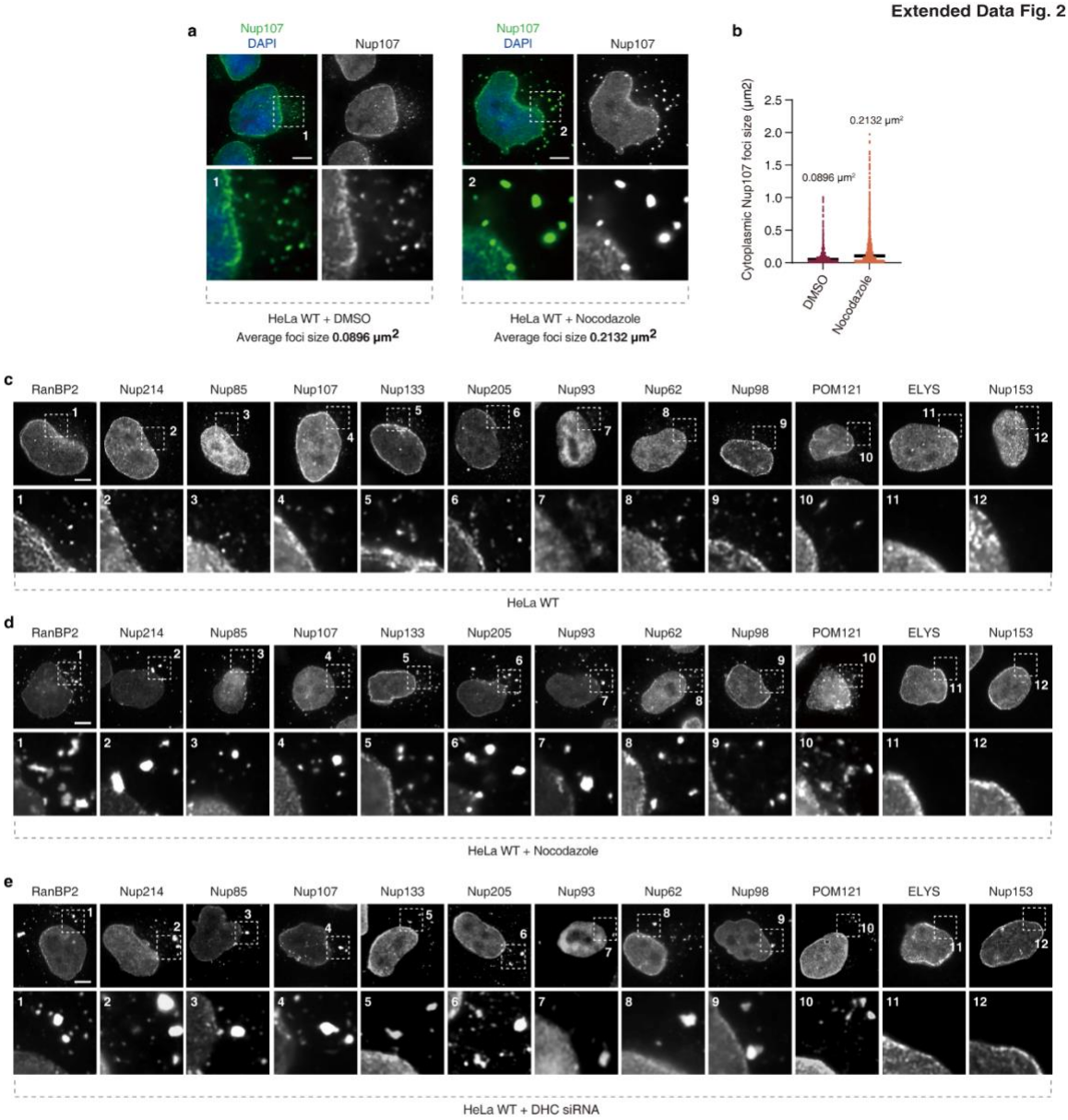

f

		NE-NPCs	AL-NPCs WT	AL-NPCs Nocodazole	AL-NPCs DHC siRNA	AL-NPCs FXR1 siRNA*	AL-NPCs UBAP2L KO*
Cytoplasmic filaments	RanBP2	Y	Y	Y	Y	Y	Y
	Nup214	Y	Y	Y	Y	Y	-
Outer rings	Nup85	Y	Y	Y	Y	Y	Y
	Nup107	Y	Y	Y	Y	Y	Y
	Nup133	Y	Y	Y	Y	Y	Y
	ELYS	**Y**	**N**	**N**	**N**	**N**	**N**
Inner rings	Nup205	Y	Y	Y	Y	-	Y
	Nup93	Y	Y	Y	Y	-	Y
Central channel	Nup62	Y	Y	Y	Y	Y	Y
Linker Nups	Nup98	Y	Y	Y	Y	Y	Y
Transmembrane Nups	POM121	Y	Y	Y	Y	Y	Y
Nuclear basket	Nup153	**Y**	**N**	**N**	**N**	**N**	**N**

Extended Data Fig.2. Systematic analysis of the size and the composition of AL foci. a, b, Representative images of 2xZFN-mEGFP-Nup107 HeLa cells treated with nocodazole (10 µM) or DMSO (90 min) (a). Cells were co-labelled with DAPI (blue). The magnified framed regions are shown in the corresponding numbered panels. The size of Nup107-positive AL

1719 foci in the cytoplasm were quantified in (b), and at least 2000 foci per condition were analyzed
1720 (N=3). Scale bars, 5 μm.

1721 c, Representative images of WT HeLa cells labelled with Nups from different NPC
1722 subcomplexes. Analyzed Nups are indicated above each panel. The magnified framed regions
1723 are shown in the corresponding numbered panels. Scale bars, 5 μm.

1724 d, Representative images of nocodazole-treated (10 μM, 90 min) HeLa cells labelled with Nups
1725 from different NPC subcomplexes. Analyzed Nups are indicated above each panel. The
1726 magnified framed regions are shown in the corresponding numbered panels. Scale bars, 5 μm.

1727 e, Representative images of dynein heavy chain siRNAs-treated (48h) HeLa cells labelled with
1728 Nups from different NPC subcomplexes. Analyzed Nups are indicated above each panel. The
1729 magnified framed regions are shown in the corresponding numbered panels. Scale bars, 5 μm.

1730 f, Summary of composition of NE-NPCs and AL-NPCs under different conditions. Different
1731 colors represent specific NPC subcomplexes. “Y” indicates presence and “N” indicates
1732 absence of indicated Nups. “-” represents no available data. “*” indicates published
1733 results[25,27,28].

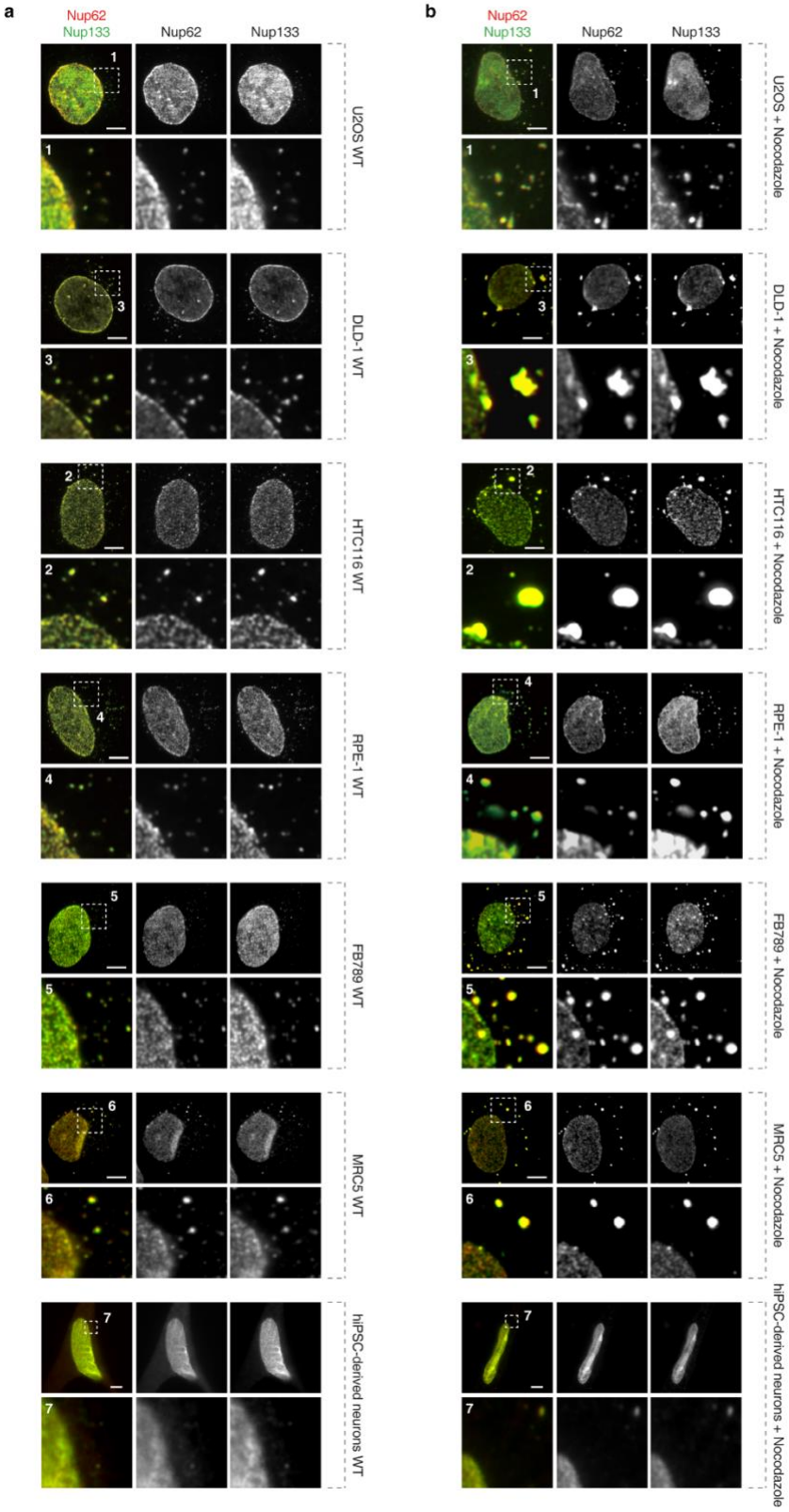

Extended Data Fig.3. AL exist in a variety of somatic mammalian cells.

1736 a, Representative images of WT U2OS, DLD-1, HTC116, RPE-1, FB789, MRC5 and hiPSC-
1737 derived neuron cells showing AL foci. Cells were co-labelled with anti-Nup62 (red) and anti-
1738 Nup133 (green) antibodies to visualize AL-NPCs. Scale bars, 5 μm.

1739 b, Representative images of U2OS, DLD-1, HTC116, RPE-1, FB789, MRC5 and hiPSC-
1740 derived neuron cells treated with nocodazole (10 μM, 90 min). Cells were co-labelled with anti-
1741 Nup62 (red) and anti-Nup133 (green) antibodies to visualize AL-NPCs. Scale bars, 5 μm.

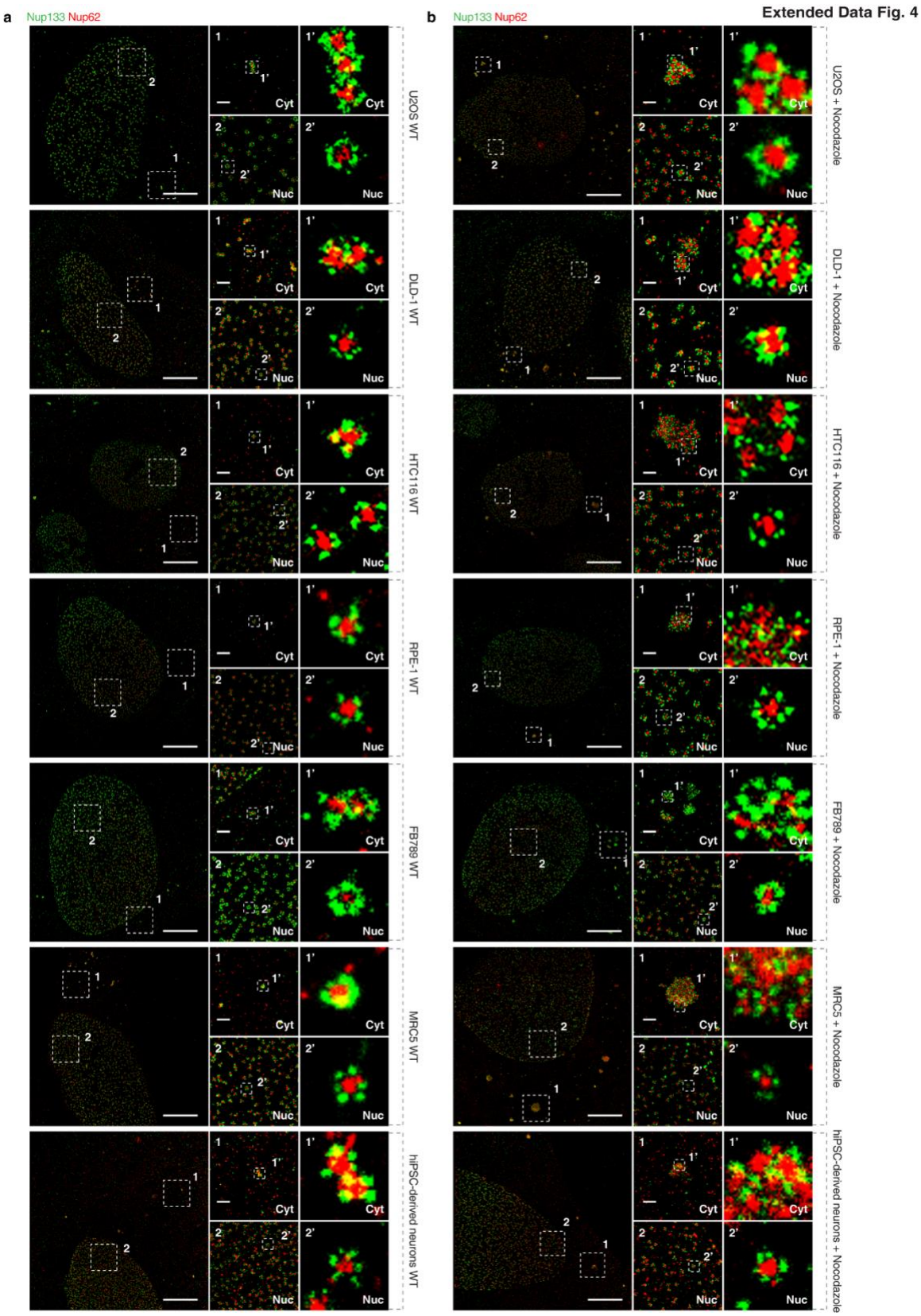

Extended Data Fig.4. AL exist in a variety of somatic mammalian cells.

1744 a, Representative splitSMLM images depicting NPCs on the nuclear (Nuc) surface and AL-
1745 NPCs in the cytoplasm (Cyt) in WT U2OS, DLD-1, HTC116, RPE-1, FB789, MRC5 and hiPSC-
1746 derived neuron cells. Analyzed Nups from different NPC subcomplexes are indicated above
1747 each panel. The magnified framed regions are shown in the corresponding numbered panels.
1748 Scale bars, 3 μm (entire nuclei), 0.3 μm (zoomed regions).

1749 b, Representative splitSMLM images depicting NPCs on the nuclear (Nuc) surface and AL-
1750 NPCs in the cytoplasm (Cyt) in nocodazole-treated (10 μM, 90 min) U2OS, DLD-1, HTC116,
1751 RPE-1, FB789, MRC5 and hiPSC-derived neuron cells. Analyzed Nups from different NPC
1752 subcomplexes are indicated above each panel. The magnified framed regions are shown in
1753 the corresponding numbered panels. Scale bars, 3 μm (entire nuclei), 0.3 μm (zoomed
1754 regions).

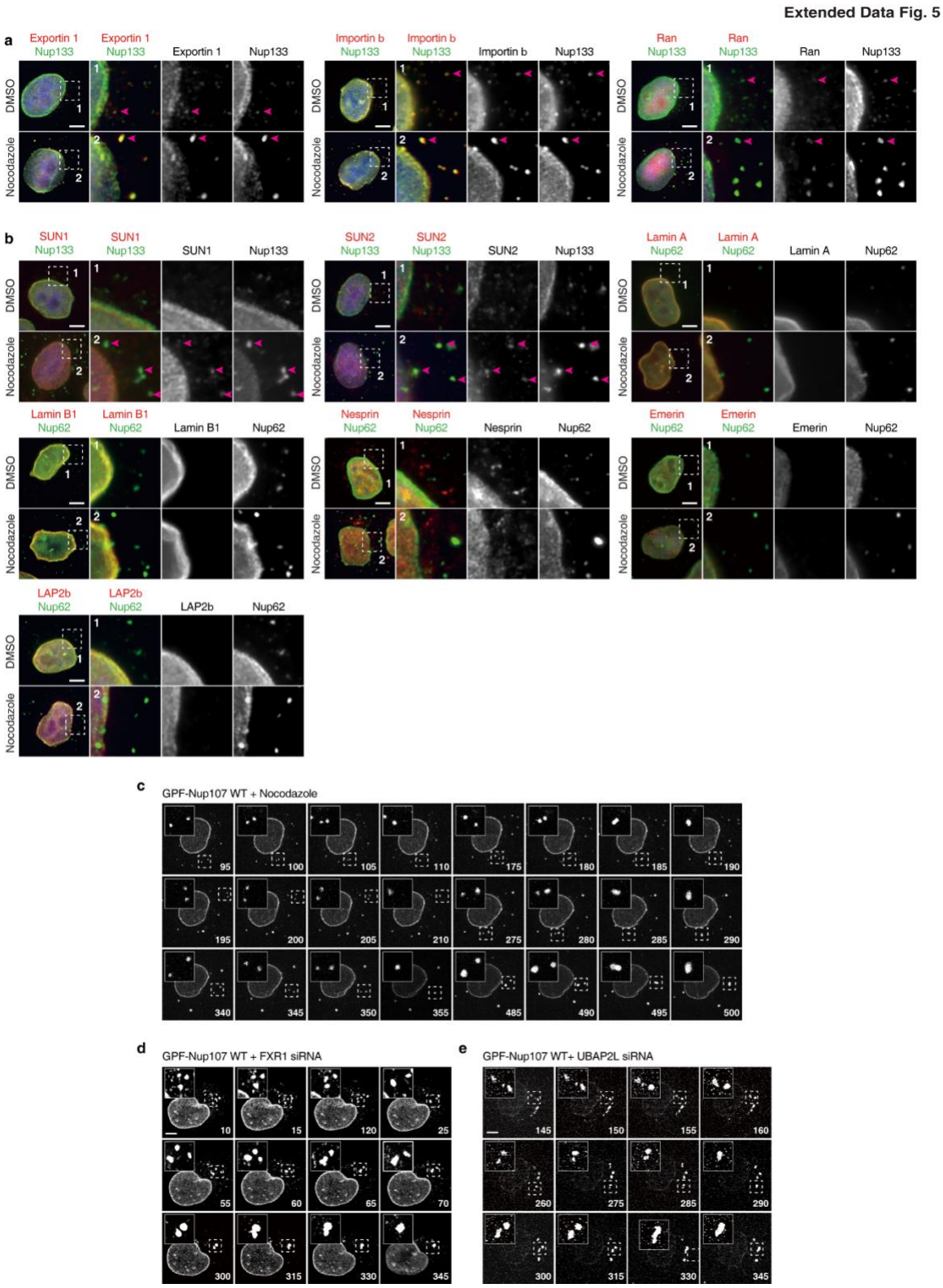

Extended Data Fig.5. Systematic analysis of AL composition and clustering of AL-NPCs. a, Representative images showing co-localization of nucleocytoplasmic transport factors (NTF) with AL-NPC foci in HeLa cells treated with nocodazole (10 μM) or DMSO (90 min). Cells were co-labelled with anti-NTF (Exportin-1, Importin β, and Ran) (red) and anti-Nup133 (green)

1760 antibodies. The magnified framed regions are shown in the corresponding numbered panels.
1761 Magenta arrows point to co-localized AL and NTF foci signals. Scale bars, 5 μm.

1762 b, Representative images showing co-localization of NE-related proteins with AL-NPC foci in
1763 HeLa cells treated with nocodazole (10 μM) or DMSO (90 min). Cells were co-labelled with
1764 anti-NE-related proteins (SUN1, SUN2, Lamin A, Lamin B1, Nesprin, Emerin, and Lap2) (red)
1765 and anti-Nup62 (green) antibodies. The magnified framed regions are shown in the
1766 corresponding numbered panels. Magenta arrows point to co-localized AL and NE-factors foci.
1767 Scale bars, 5 μm.
1768 c, 2xZFN-mEGFP-Nup107 HeLa cells treated with nocodazole were analyzed by live video
1769 spinning disk confocal microscopy. Selected representative frames of the Videos are depicted,
1770 and time is shown in minutes after nocodazole addition at the timepoint 0. The magnified
1771 framed regions are shown in the upper left corner. Scale bars, 5 μm.

1772 d, 2xZFN-mEGFP-Nup107 HeLa cells treated with FXR1 siRNA were analyzed by live video
1773 spinning disk confocal microscopy. The selected representative frames of the Videos are
1774 depicted, and time is shown in minutes. The timepoint 0 of the Video corresponds to a 12h
1775 release time from double thymidine block. The magnified framed regions are shown in the
1776 upper left corner. Scale bars, 5 μm.

1777 e, 2xZFN-mEGFP-Nup107 HeLa cells treated UBAP2L siRNA were analyzed by live video
1778 spinning disk confocal microscopy. The selected representative frames of the Videos are
1779 depicted, and time is shown in minutes. The timepoint 0 of the Video corresponds to a 12h
1780 release time from double thymidine block. The magnified framed regions are shown in the
1781 upper left corner. Scale bars, 5 μm.

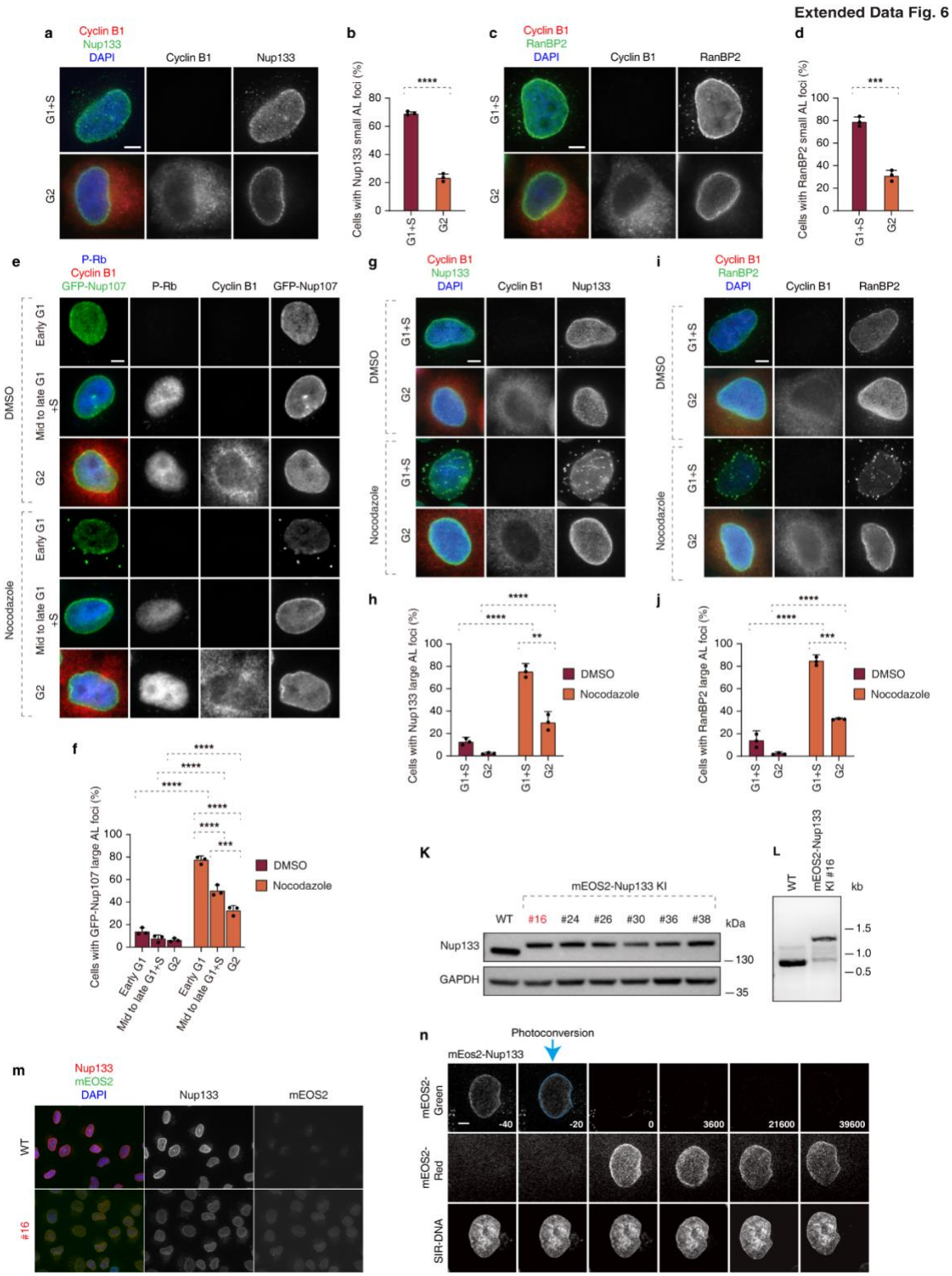

Extended Data Fig.6. AL foci are predominantly present in the G1 and S cell cycle phases.

a, b, Representative images of asynchronously proliferating HeLa cells co-labelled with anti-Nup133 (green) and anti-cyclin B1 (red) (a) antibodies. The percentage of cells with Nup133-positive small AL foci in cyclin B1 negative cells (G1+S), and cyclin B1 positive cells (G2) was

1788 quantified in (b), and at least 200 cells per condition were analyzed (unpaired two-tailed t test,
1789 mean ± SD, ****P < 0.0001; N = 3). Scale bars, 5 μm.

1790 c, d, Representative images of asynchronously proliferating HeLa cells co-labelled with anti-
1791 RanBP2 (green) and anti-cyclin B1 (red) (c) antibodies. The percentage of cells with RanBP2-
1792 positive small AL foci in cyclin B1 negative cells (G1+S), and cyclin B1 positive cells (G2) was
1793 quantified in (d), and at least 200 cells per condition were analyzed (unpaired two-tailed t test,
1794 mean ± SD, ***P < 0.001; N = 3). Scale bars, 5 μm.

1795 e, f, Representative images of asynchronously proliferating 2xZFN-mEGFP-Nup107 HeLa
1796 cells treated with nocodazole (10 μM) or DMSO (90 min) and co-labelled with anti-p-Rb (blue)
1797 and anti-cyclin B1 (red) (e) antibodies. The percentage of cells with large AL foci in p-Rb and
1798 cyclin B1 negative cells (early G1), p-Rb positive and cyclin B1 negative cells (mid to late
1799 G1+S), and p-Rb and cyclin B1 positive cells (G2) was quantified in (f), and at least 200 cells
1800 per condition were analyzed (one-Way ANOVA test, mean ± SD, ***P < 0.001; ****P < 0.0001;
1801 N = 3). Scale bars, 5 μm.

1802 g, h, Representative images of asynchronously proliferating HeLa cells treated with
1803 nocodazole (10 μM) or DMSO (90 min) and co-labelled with anti-Nup133 (green) and anti-
1804 cyclin B1 (red) (g) antibodies. The percentage of cells with large AL foci in cyclin B1 negative
1805 cells (G1+S), and cyclin B1 positive cells (G2) was quantified in (h), and at least 200 cells per
1806 condition were analyzed (one-Way ANOVA test, mean ± SD, **P < 0.01; ****P < 0.0001; N =
1807 3). Scale bars, 5 μm.

1808 i, j, Representative images of asynchronously proliferating HeLa cells treated with nocodazole
1809 (10 μM) or DMSO (90 min) and co-labelled with anti-RanBP2 (green) and anti-cyclin B1 (red)
1810 (i) antibodies. The percentage of cells with large AL foci in cyclin B1 negative cells (G1+S),
1811 and cyclin B1 positive cells (G2) was quantified in (j), and at least 200 cells per condition were
1812 analyzed (one-Way ANOVA test, mean ± SD, ***P < 0.001; ****P < 0.0001; N = 3). Scale bars,
1813 5 μm.

1814 k, l, Validation of CRISPR/Cas9-mediated mEos2-Nup133 KI HeLa cell clones by Western blot
1815 (k) and PCR (l).

1816 m, Representative images of mEos2-Nup133 KI HeLa cells. Cells were co-labelled with DAPI
1817 (blue), and anti-Nup133 (red) antibody. Scale bars, 5 μm.

1818 n, The photoconversion of NE-Nup133 in mEOS2-Nup133 HeLa cells were analyzed by live
1819 video spinning disk confocal microscopy. The selected representative frames of the Videos
1820 are depicted, and time is shown in seconds. The magnified framed regions of mEOS2-Red
1821 signal are shown in the lower panels. The blue dashed box indicates the photoconversion
1822 region, where mEOS2-Nup 133 is converted from a green to a red fluorescent state. Scale
1823 bars, 5 μm.

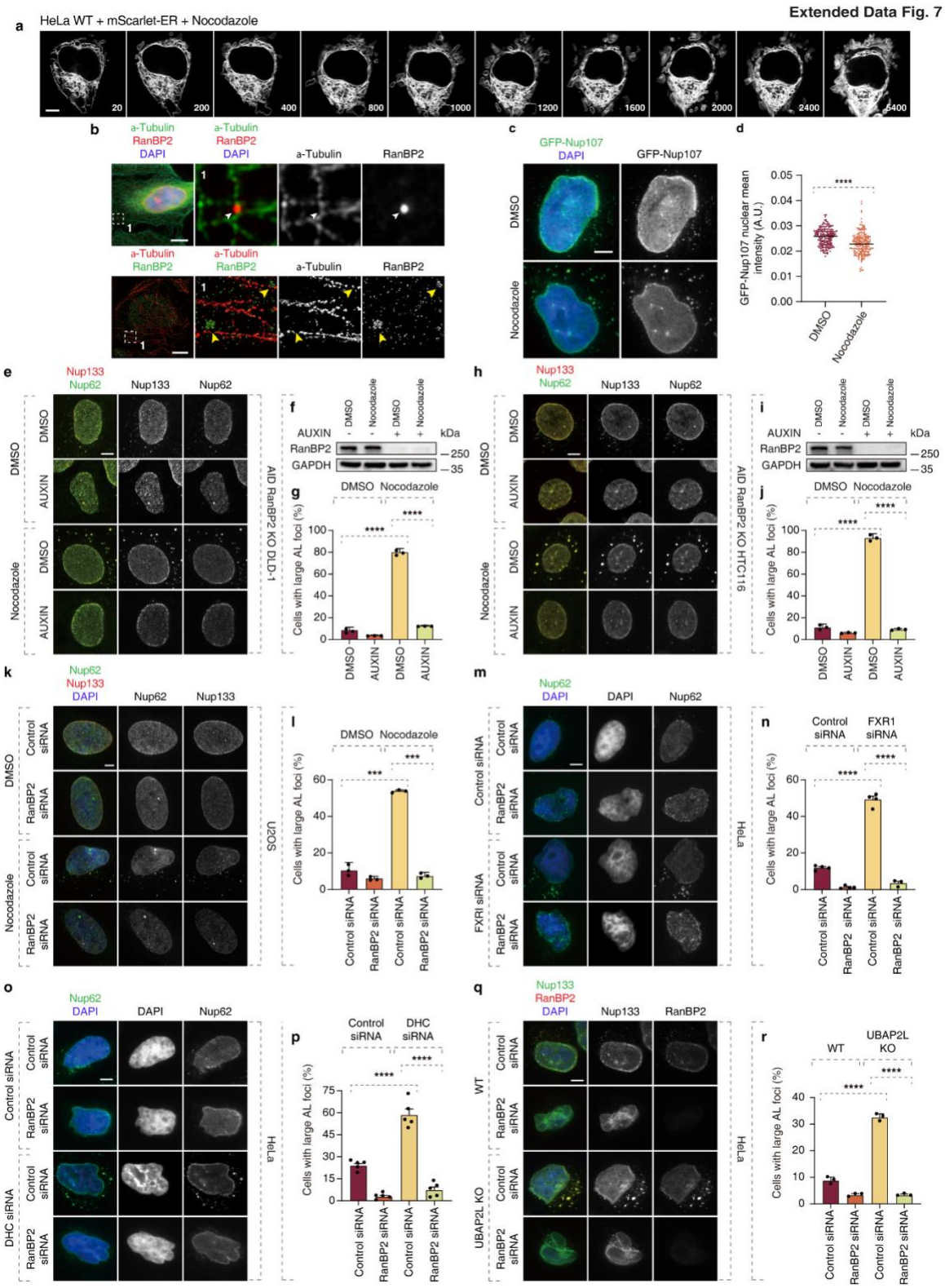

Extended Data Fig.7. RanBP2 is required for the accumulation and clustering of large AL in challenged somatic cells.

1828 a, HeLa cells expressing ER marker plasmid mScarlet-ER were treated with nocodazole (10
1829 μM) and were analyzed by live video spinning disk confocal microscopy. The selected
1830 representative frames of the Videos are depicted, and time is shown in second. The timepoint
1831 0 corresponds to nocodazole addition. The magnified framed regions are shown in the upper
1832 left corner. Scale bars, 5 μm.

1833 b, Representative immunofluorescence (IF) images and splitSMLM analysis depicting co-
1834 localization of AL-NPCs and microtubules in the cytoplasm in WT HeLa cells. For the IF at the
1835 top, cells were co-labelled with anti-alpha tubulin (green), anti-RanBP2 (red) antibodies and
1836 DAPI. For the splitSMLM at the bottom, cells were co-labelled with anti-alpha tubulin (red), and
1837 anti-RanBP2 (green) antibodies. The magnified framed regions are shown in the
1838 corresponding numbered panels. Arrowheads point to AL-NPCs localized near microtubules.
1839 Scale bars, IF, 5 μm; SMLM, 3 μm.

1840 c, d, Representative images of 2xZFN-mEGFP-Nup107 HeLa cells treated with Nocodazole
1841 (10 μM) or DMSO (90 min) (c). Cells were co-labelled with DAPI (blue). The intensity of EGFP-
1842 Nup107 in the NE was quantified in (d), and at least 200 cell per condition were analyzed
1843 (unpaired two-tailed t test, mean ± SD, ****P < 0.0001; N = 3). Scale bars, 5 μm.

1844 e, f, Representative images of auxin-inducible degron (AID)-RanBP2 KO DLD-1 cells treated
1845 with the auxin or DMSO (4h) and subsequently with nocodazole (10 μM) or DMSO (90 min).
1846 Cells were co-labelled with anti-Nup62 (red) and anti-Nup133 (green) (e) antibodies. (B) The
1847 Western blot analysis of RanBP2 under different conditions shown in (f). The number of cells
1848 with large AL foci were quantified in (G), and at least 1000 cells per condition were analyzed
1849 (one-Way ANOVA test, mean ± SD, ****P < 0.0001; N = 3). Scale bars, 5 μm.

1850 h-j, Representative images of AID-RanBP2 KO HTC116 cells treated with auxin or DMSO (4h)
1851 and subsequently with nocodazole (10 μM) or DMSO (90 min). Cells were co-labelled with
1852 anti-Nup62 (red) and anti-Nup133 (green) (h) antibodies. (i) The Western blot analysis of
1853 RanBP2 under different conditions shown in (j). The number of cells with large AL foci were
1854 quantified in (K), and at least 1000 cells per condition were analyzed (one-Way ANOVA test,
1855 mean ± SD, ****P < 0.0001; N = 3). Scale bars, 5 μm.

1856 k, l, Representative images of U2OS cells treated with the indicated siRNAs (48h) and
1857 subsequently with nocodazole (10 μM) or DMSO (90 min). Cells were co-labelled with anti-
1858 Nup62 (green) and anti-Nup133 (red) (k) antibodies. The number of cells with large AL foci
1859 was quantified in (l), and at least 1000 cells per condition were analyzed ((one-Way ANOVA
1860 test, mean ± SD, ***P < 0.001; N = 3). Scale bars, 5 μm.

1861 m, n, Representative images of HeLa cells treated with the indicated siRNAs (48h). Cells were
1862 co-labelled with anti-Nup62 (green) antibodies and DAPI (blue) (m). The number of cells with
1863 large AL foci were quantified in (n), and at least 1000 cells per condition were analyzed (one-
1864 Way ANOVA test, mean ± SD, ****P < 0.0001; N = 3). Scale bars, 5 μm.

1865 o, p, Representative images of HeLa cells treated with the indicated siRNAs (48h). Cells were
1866 co-labelled with anti-Nup62 (green) antibodies and DAPI (blue) (o). The number of cells with
1867 large AL foci were quantified in (p), and at least 1000 cells per condition were analyzed (mean
1868 ± SD, ****P < 0.0001; N = 3). Scale bars, 5 μm.

1869 q, r, Representative images of UBAP2L KO and WT HeLa cells treated with the indicated
1870 siRNAs (48h). Cells were co-labelled with anti-Nup133 (green) and anti-RanBP2 (red) (q)
1871 antibodies. The number of cells with large AL foci were quantified in (r), and at least 1000 cells
1872 per condition were analyzed (one-Way ANOVA test, mean ± SD, ****P < 0.0001; N = 3). Scale
1873 bars, 5 μm.

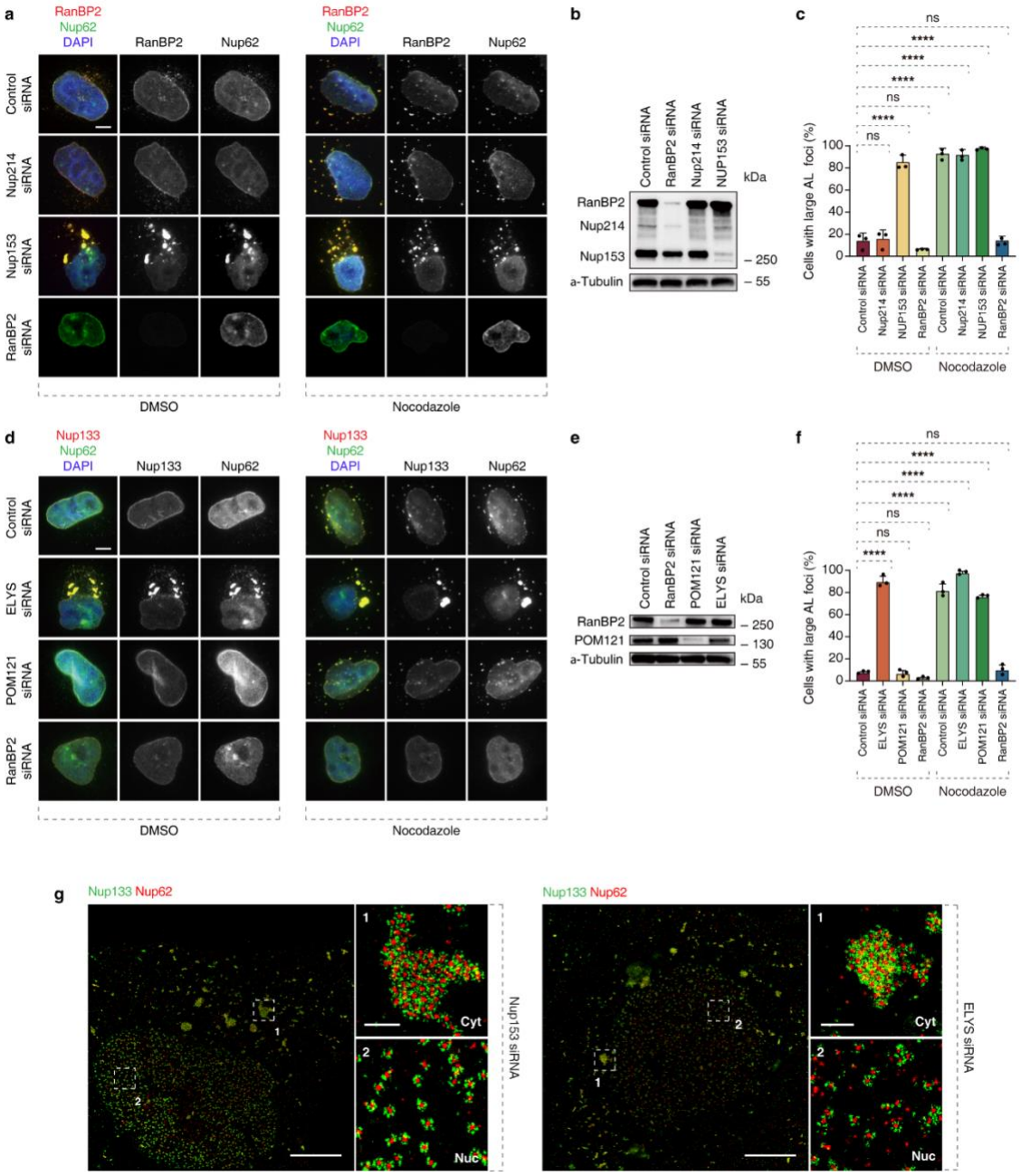

Extended Data Fig. 8. RanBP2, but not Nup153, Nup214, POM121 and ELYS, is required for the formation of large AL in challenged somatic cells.
a-c, Representative images of HeLa cells treated with the indicated siRNAs (48h) and subsequently with nocodazole (10 μM) or DMSO (90 min). Cells were co-labelled with anti-Nup62 (green) and anti-RanBP2 (red) (a) antibodies. (b) Shows the Western blot analysis of RanBP2, Nup214 and Nup153 under different conditions shown in (a). The number of cells with large AL foci was quantified in (c), and at least 1000 cells per condition were analyzed (one-Way ANOVA test, mean ± SD, ns: not significant, ****P < 0.0001; N = 3). Scale bars, 5 μm.

1884 d-f, Representative images of HeLa cells treated with the indicated siRNAs (48h) and
1885 subsequently with nocodazole (10 μM) or DMSO (90 min). Cells were co-labelled with anti-
1886 Nup62 (green) and anti-Nup133 (red) (d) antibodies. (e) Shows the Western blot analysis of
1887 RanBP2, and POM121 under different conditions shown in (d). The number of cells with large
1888 AL foci was quantified in (f), and at least 1000 cells per condition were analyzed (one-Way
1889 ANOVA test, mean ± SD, ns: not significant, ****P < 0.0001; N = 3). Scale bars, 5 μm.

1890 g, Representative splitSMLM images depicting NPCs on the nuclear (Nuc) surface and AL-
1891 NPCs in the cytoplasm (Cyt) in Nup153 siRNA or ELYS siRNA-treated (48h) HeLa cells.
1892 Nup133 signal labels the cytoplasmic and nuclear rings of the NPC, the localization of the
1893 central channel is visualized by Nup62. The magnified framed regions are shown in the
1894 corresponding numbered panels. Scale bars, 3 μm, 0.3 μm (zoomed-in).

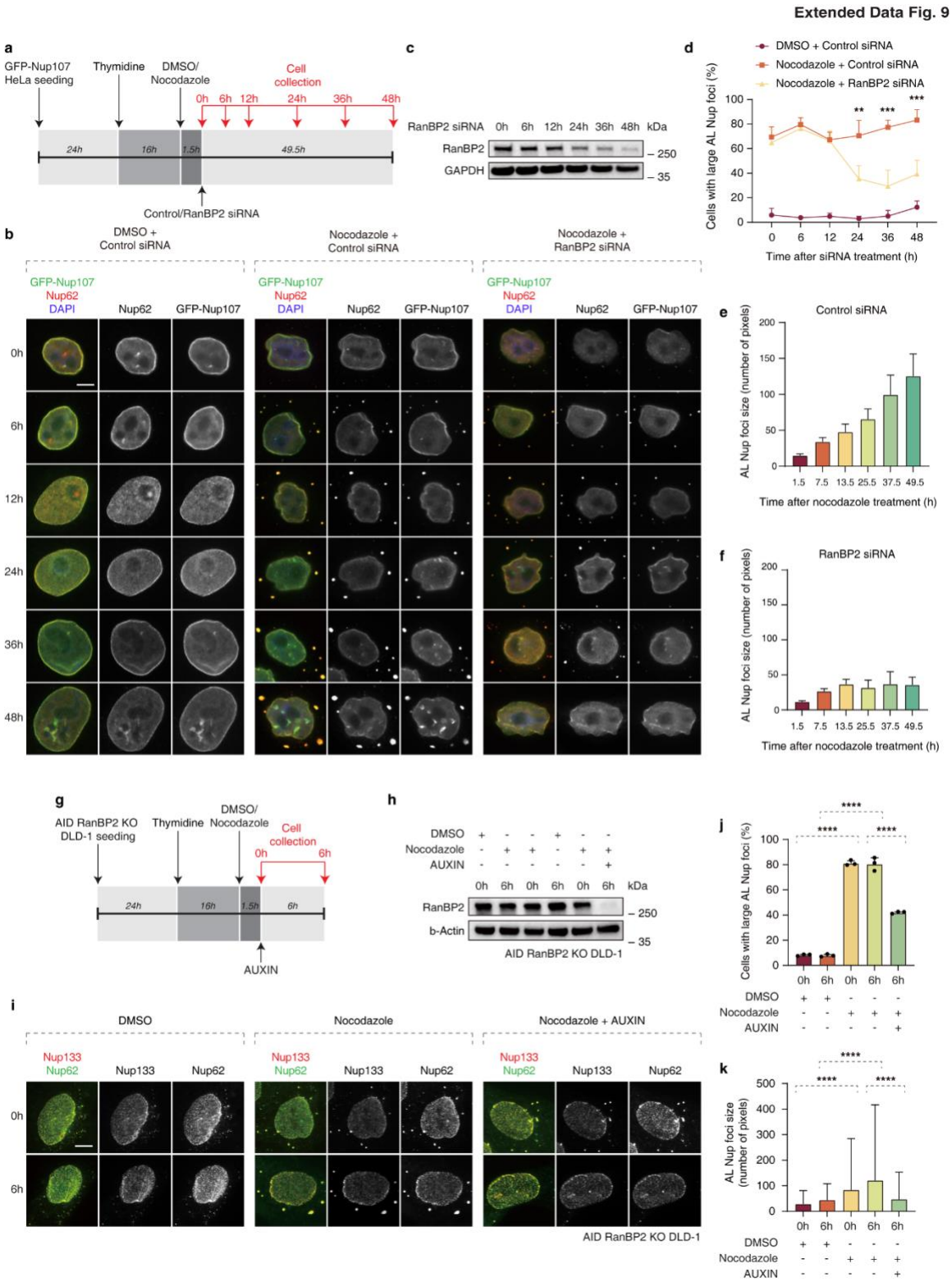

Extended Data Fig. 9. RanBP2 is required for the maintenance of large AL.
a-f, Scheme of the experimental setup (a). HeLa cells were synchronized and arrested in S phase by thymidine treatment (16h), treated with nocodazole (10 μM) and subsequently with the indicated siRNAs, and fixed at indicated timepoints. Representative images of cells are

1900 shown in (b). (c) Shows the Western blot analysis of RanBP2 at indicated timepoints. The
1901 number of cells with large AL foci was quantified in (d) and the size of AL foci was quantified
1902 in (e, f). At least 200 cells and 1500 foci per condition were analyzed (one-Way ANOVA test,
1903 mean ± SD, ****P < 0.0001; N = 3). Scale bars, 5 μm.

1904 g-k, Scheme of the experimental setup (g). AID-RanBP2 KO DLD-1 cells were synchronized
1905 and arrested at S phase by thymidine treatment (16h), treated with nocodazole (10 μM) and
1906 with auxin. Representative images of cells are shown in (i). (h) The Western blot analysis of
1907 RanBP2 under different conditions. The number of cells with large AL foci was quantified in (j)
1908 and the size of AL foci was quantified in (k). At least 200 cells and 1500 foci per condition were
1909 analyzed (one-Way ANOVA test, mean ± SD, ****P < 0.0001; N = 3). Scale bars, 5 μm

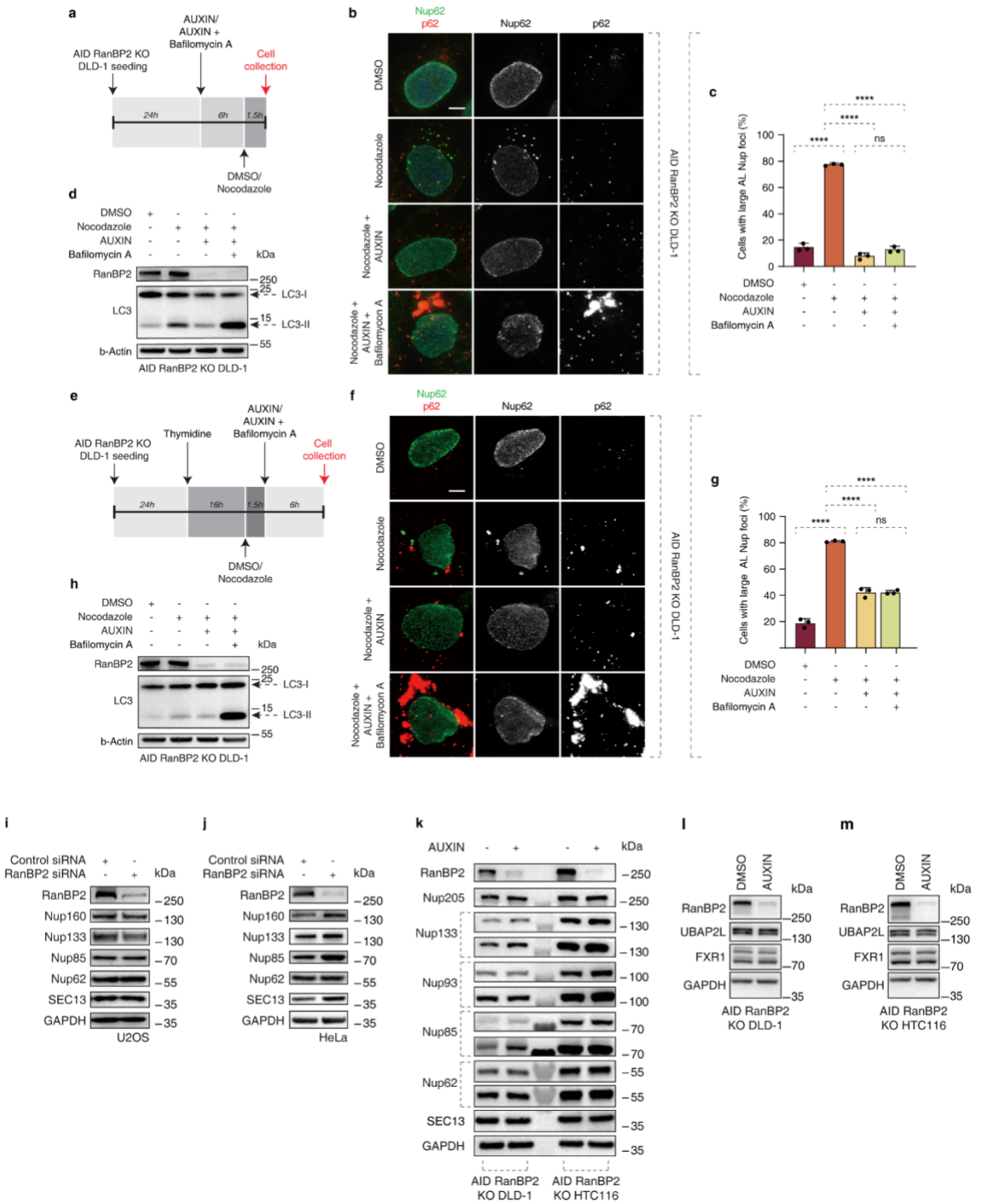

Extended Data Fig. 10. The role of RanBP2 in the formation and maintenance of large AL is independent of autophagy.

a-d, Scheme of the experimental setup (a). AID-RanBP2 KO DLD-1 cells were treated with nocodazole (10 μM), auxin and bafilomycin at indicated timepoints. Cells were co-labelled with anti-Nup62 (green) and anti-p62 (red) antibodies. Representative images of cells are shown in (b). The number of cells with large AL foci was quantified in (c). (d) Shows the Western blot analysis of RanBP2 and LC3 under different conditions shown in (d). At least 200 cells per

1918 condition were analyzed (one-Way ANOVA test, mean ± SD, ns: not significant, ****P < 0.0001;
1919 N = 3). Scale bars, 5 μm.

1920 e-h, Scheme of the experimental setup (e). AID-RanBP3 KO DLD-1 cells were synchronized
1921 and arrested in S phase by thymidine treatment (16h). Subsequently, the cells were treated
1922 with nocodazole (10 μM), auxin and bafilomycin at indicated timepoints. Cells were co-labelled
1923 with anti-Nup62 (green) and anti-p62 (red) antibodies. Representative images of cells are
1924 shown in (f). The number of cells with large AL foci were quantified in (g). The Western blot
1925 analysis of RanBP2 and LC3 under different conditions shown in (h). At least 200 cells per
1926 condition were analyzed (one-Way ANOVA test, mean ± SD, ns: not significant, ****P < 0.0001;
1927 N = 3). Scale bars, 5 μm.

1928 i-k, Protein levels of representative nucleoporins were analyzed by Western blot in U2OS,
1929 HeLa and AID RanBP2 KO DLD-1 or HTC116 cells treated with RanBP2 siRNA or Auxin to
1930 induce depletion of RanBP2.

1931 l, m, Protein levels of FXR1 and UBAP2L were analyzed by Western blot in AID RanBP2 KO
1932 DLD-1 or HTC116 cells treated with DMSO or auxin to induce depletion of RanBP2 (4h) and
1933 synchronized in early interphase.

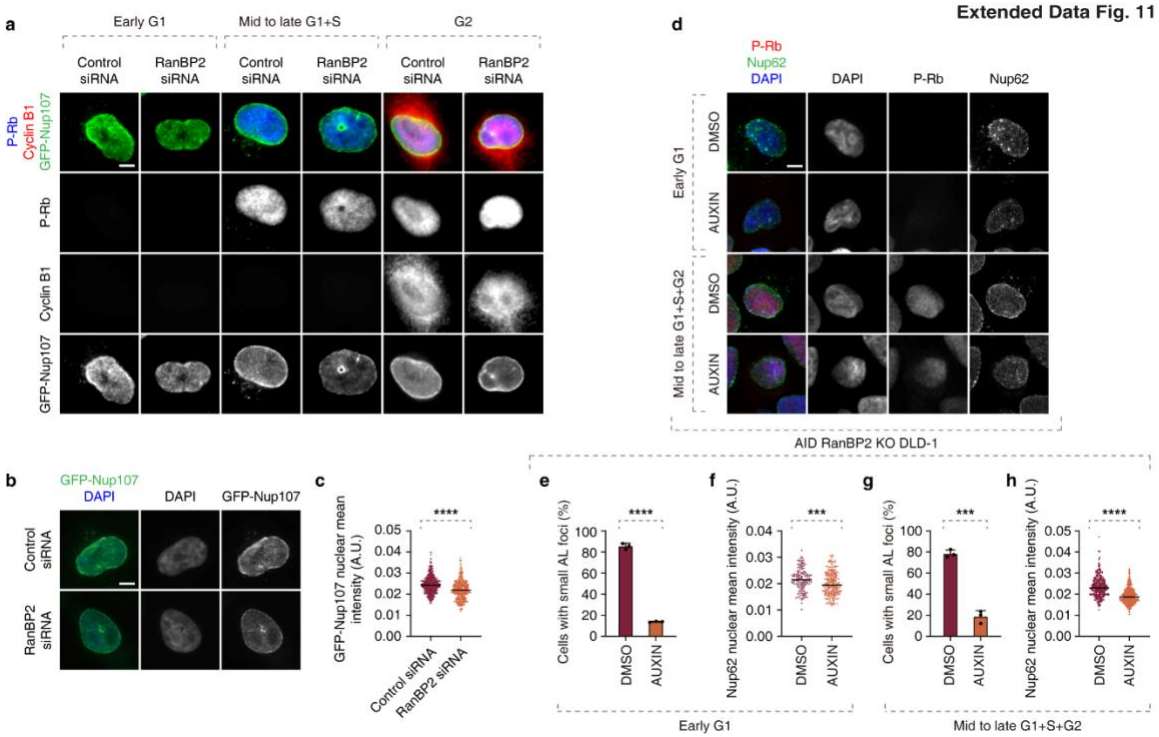

Extended Data Fig. 11. RanBP2 is required for biogenesis of small AL and localization of Nups to the NE in non-stressed interphasic cells.

a, Representative images of asynchronously proliferating 2xZFN-mEGFP-Nup107 HeLa cells treated with the indicated siRNAs (48h) and co-labelled with anti-p-Rb (blue) and anti-cyclin B1 (red) antibodies. The percentage of cells with small AL foci in p-Rb and cyclin B1 negative cells (early G1), p-Rb positive and cyclin B1 negative cells (mid to late G1+S), and p-Rb and cyclin B1 positive cells (G2) was quantified in Fig, 4m. Scale bars, 5 µm.

b, c, Representative images of 2xZFN-mEGFP-Nup107 HeLa cells treated with RanBP2 siRNA (48h) (b). Cells were co-labelled with DAPI (blue). The intensity of GFP-Nup107 at the NE was quantified in (c), and at least 400 cell per condition were analyzed (unpaired two-tailed t test, mean ± SD, ****P < 0.0001; N = 3). Scale bars, 5 µm.

d-h, Representative immunofluorescence images depicting the localization of Nup62 in AID RanBP2 KO DLD-1 cells in different cell cycle stages. p-Rb was used to distinguish cells in early G1 (p-Rb–negative cells) and mid-late G1, S, and G2 (p-Rb–positive cells) stages. Nuclei were stained with DAPI (d). The percentage of cells with small AL foci in early G1 (e), and mid-late G1, S, G2 (g) was quantified. At least 300 cells per condition were analyzed (mean ± SD, ***P < 0.001; ****P < 0.0001; unpaired two-tailed t test, n = 3 independent experiments). The NE intensity of Nup62 in early G1 cells (f), and mid-late G1, S, G2 cells (H) was quantified. At least 150 cells per condition were analyzed (mean ± SD, ***P < 0.001; ****P < 0.0001; unpaired two-tailed t test, n = 3 independent experiments). Scale bars, 5 µm.

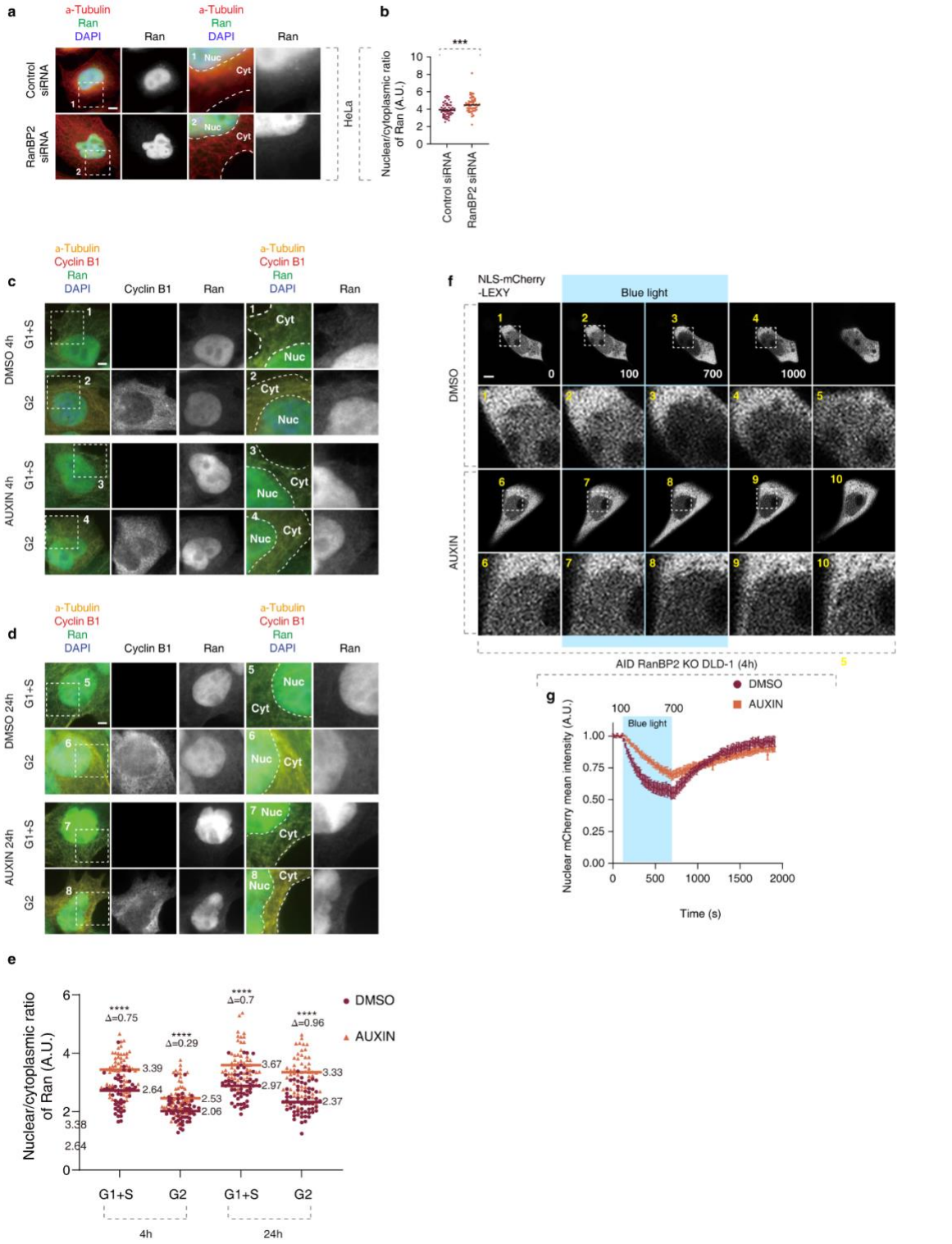

Extended Data Fig. 12. RanBP2 supports nucleocytoplasmic transport.
a, b, Representative immunofluorescence images depicting the nuclear (Nuc) and cytoplasmic (Cyt) localization of Ran in asynchronously proliferating WT and RanBP2 KD (RanBP2 siRNA

48h) HeLa cells. Cells were co-labelled with anti-Ran (green), anti-alpha-Tubulin (red) antibodies and DAPI (a). The magnified framed regions are shown in the corresponding numbered panels. The N/C ratio of Ran was quantified (b). At least 100 cells per condition were analyzed (mean ± SD, ***P < 0.001; unpaired two-tailed t test, n = 3 independent experiments). Scale bar, 5 µm.

c-e, Representative immunofluorescence images depicting the nuclear (Nuc) and cytoplasmic (Cyt) localization of Ran in asynchronously proliferating AID RanBP2 KO DLD-1 cells treated with DMSO or auxin (4h or 24h) to induce depletion of RanPB2. Cells were co-labelled with anti-Ran (green), anti-alpha-Tubulin-647 (yellow), anti-Cyclin B1 antibodies and DAPI (c and e). The magnified framed regions are shown in the corresponding numbered panels. The nuclear/cytoplasmic (N/C) ratio of Ran was quantified in (e). At least 100 cells per condition were analyzed (mean ± SD, ****P < 0.0001; unpaired two-tailed t test, n = 3 independent experiments). Scale bar, 5 µm.

f, g, Representative immunofluorescence images depicting nuclear fluorescence NLS-mCherry-LEXY shuttling reporter expressed in AID RanBP2 KO DLD-1 cells treated with DMSO or auxin (4h) to induce depletion of RanPB2 (f). Cells were incubated in the dark for 100 s before blue light irradiation for 600 s was applied, which was followed by a 1200 s dark-recovery phase. Time is indicated in seconds. Relative nuclear fluorescence was quantified in (g). At least 10 cells per condition were analyzed (mean ± SD, n = 3 independent experiments).

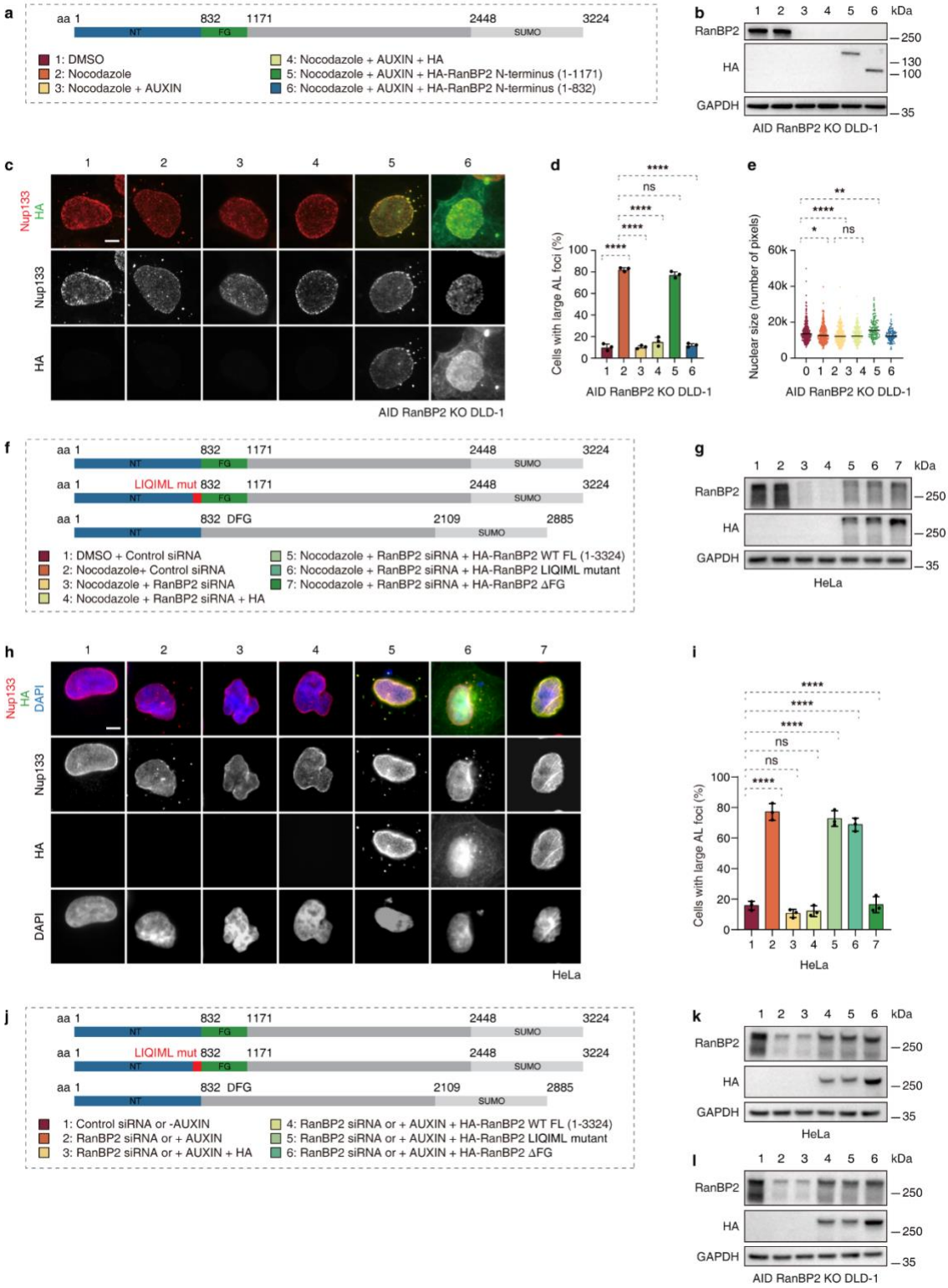

Extended Data Fig. 13. RanBP2 is specifically required for the formation of large AL through its N-terminal FG repeat region.

1984 a-e Rescue experiments using different RanBP2 protein fragments (a). (b) Shows the Western
1985 blot analysis of RanBP2 fragments under different conditions indicated. (c) shows
1986 representative images of AID-RanBP2 KO DLD-1 cells treated with the DMSO or auxin,
1987 transfected with different RanBP2 fragments and treated with nocodazole (10 μM) or DMSO
1988 (90 min). Cells were co-labelled with anti-Nup133 (red) and anti-HA (green) antibodies. The
1989 number of cells with large AL foci was quantified in (d), the nuclear size was quantified in (e),
1990 and at least 300 cells per condition were analyzed (one-Way ANOVA test, mean ± SD, ns: not
1991 significant, *P < 0.05; **P < 0.01; ****P < 0.0001; N = 3). Scale bar, 5 μm.

1992 f-l, Rescue experiments using different RanBP2 protein version (f). (g) Shows the Western blot
1993 analysis of RanBP2 version under different conditions indicated (numbers in the schematic
1994 diagram). (h) shows representative images of HeLa cells treated with the control or RanBP2
1995 siRNAs, transfected with different RanBP2 version and treated with nocodazole (10 μM) or
1996 DMSO (90 min). Cells were co-labelled with anti-Nup133 (red) and anti-HA (green) antibodies.
1997 The number of cells with large AL foci was quantified in (i), and at least 300 cells per condition
1998 were analyzed (one-Way ANOVA test, mean ± SD, ns: not significant, *P < 0.05; **P < 0.01;
1999 ****P < 0.0001; N = 3). Scale bar, 5 μm.

2000 j-l, Rescue experiments using different RanBP2 protein versions (j). (k and l) The Western blot
2001 analysis of RanBP2 fragments under different conditions indicated (numbers in the schematic
2002 diagram). Representative images and analysis are shown in Fig 5J and 5K.

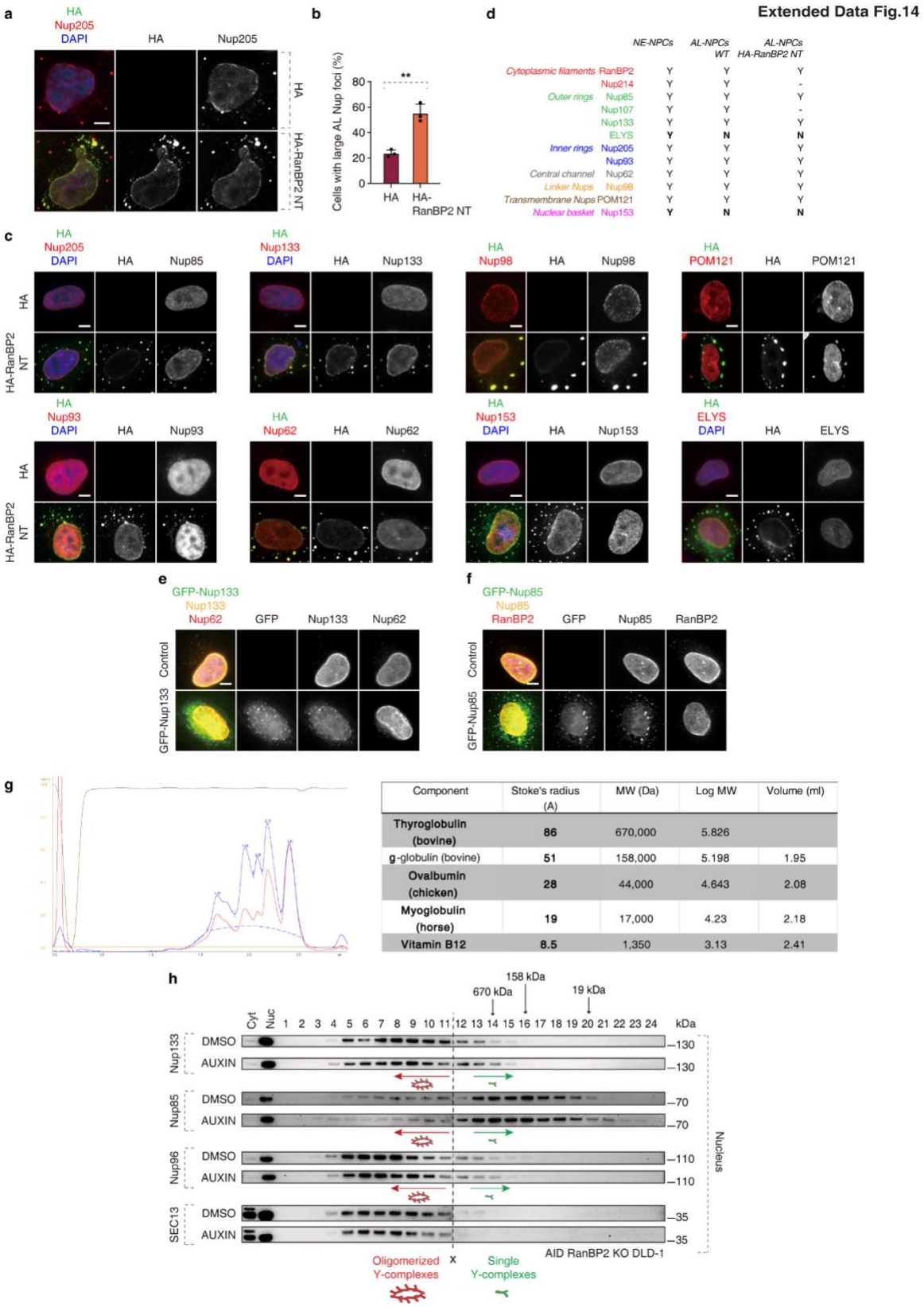

	NE-NPCs	AL-NPCs WT	AL-NPCs HA-RanBP2 NT
Cytoplasmic filaments RanBP2	Y	Y	Y
Nup214	Y	Y	-
Outer rings Nup85	Y	Y	Y
Nup107	Y	Y	-
Nup133	Y	Y	Y
ELYS	**Y**	**N**	**N**
Inner rings Nup205	Y	Y	Y
Nup93	Y	Y	Y
Central channel Nup62	Y	Y	Y
Linker Nups Nup98	Y	Y	Y
Transmembrane Nups POM121	Y	Y	Y
Nuclear basket Nup153	**Y**	**N**	**N**

Component	Stoke's radius (A)	MW (Da)	Log MW	Volume (ml)
Thyroglobulin (bovine)	**86**	670,000	5.826	
g-globulin (bovine)	**51**	158,000	5.198	1.95
Ovalbumin (chicken)	**28**	44,000	4.643	2.08
Myoglobulin (horse)	**19**	17,000	4.23	2.18
Vitamin B12	**8.5**	1,350	3.13	2.41

Extended Data Fig. 14. N-terminal fragment of RanBP2 promotes AL formation.

2005 a, b, Representative images of HeLa cells transfected with HA or HA-RanBP2 N-terminal (NT)
2006 fragment. Cells were co-labelled with DAPI (blue), anti-Nup205 (red) and anti-HA (green)
2007 antibodies (a). The number of cells with large AL foci was quantified in (b), and at least 300
2008 cells per condition were analyzed (unpaired two-tailed t test, mean ± SD, **P < 0.01; N = 3).
2009 Scale bar, 5 μm.

2010 c, Representative images of HeLa cells transfected with HA or HA-RanBP2 N-terminal (NT)
2011 fragment and labelled for Nups from different NPC subcomplexes as indicated. Cells were co-
2012 labelled with DAPI (blue), anti-Nups (red) and anti-HA (green) antibodies. Scale bars, 5 μm.

2013 d, Summary of nucleoporin composition in NE-NPCs, ALC-NPCs and AL-NPCs-induced by
2014 RanBP2-NT expression. Different colors correspond to specific NPC subcomplexes. "Y"
2015 indicates presence and "N" indicates absence of specific Nups and "-" indicates no available
2016 data.

2017 e, Representative images of HeLa cells transfected with GFP-Nup133. Cells were co-labelled
2018 with Nup133 (yellow), and anti-Nup62 (red) antibodies. Scale bars, 5 μm.

2019 f, Representative images of HeLa cells transfected with GFP-Nup85. Cells were co-labelled
2020 with Nup85 (yellow), and anti-RanBP2 (red) antibodies. Scale bars, 5 μm. Note that expression
2021 of RanBP2-NT but not Nup133 or Nup85 induce large AL foci where multiple Nups can co-
2022 localize.

2023 g, Calibration of the Superose 6 column was carried out with thyroglobulin (bovine), g-globulin
2024 (bovine), ovalbumin (chicken), myoglobulin (horse) and vitamin B12. The calibration profile
2025 and the molecular weights of the protein markers are indicated

2026 h, Auxin-inducible degron (AID) RanBP2 KO DLD-1 cells were treated with DMSO or Auxin for
2027 4h to deplete RanBP2 and nuclear fractions were prepared, separated on a Superose 6 gel
2028 filtration column and analyzed by Western blotting (at least 3 independent experiments).
2029 Fraction 1 corresponds to the void and the elution of thyroglobulin (670 kDa), g-globulin (158
2030 kDa) and myoglobulin markers 19 kDa are indicated. Green arrows point to fractions
2031 preferentially containing single Y-complexes, and red arrows indicate fraction with higher
2032 molecular weight, oligomerized Y-complexes. Note that depletion of RanBP2 did not affect the
2033 abundance of oligomerized Y-complexes in the nuclear fractions.

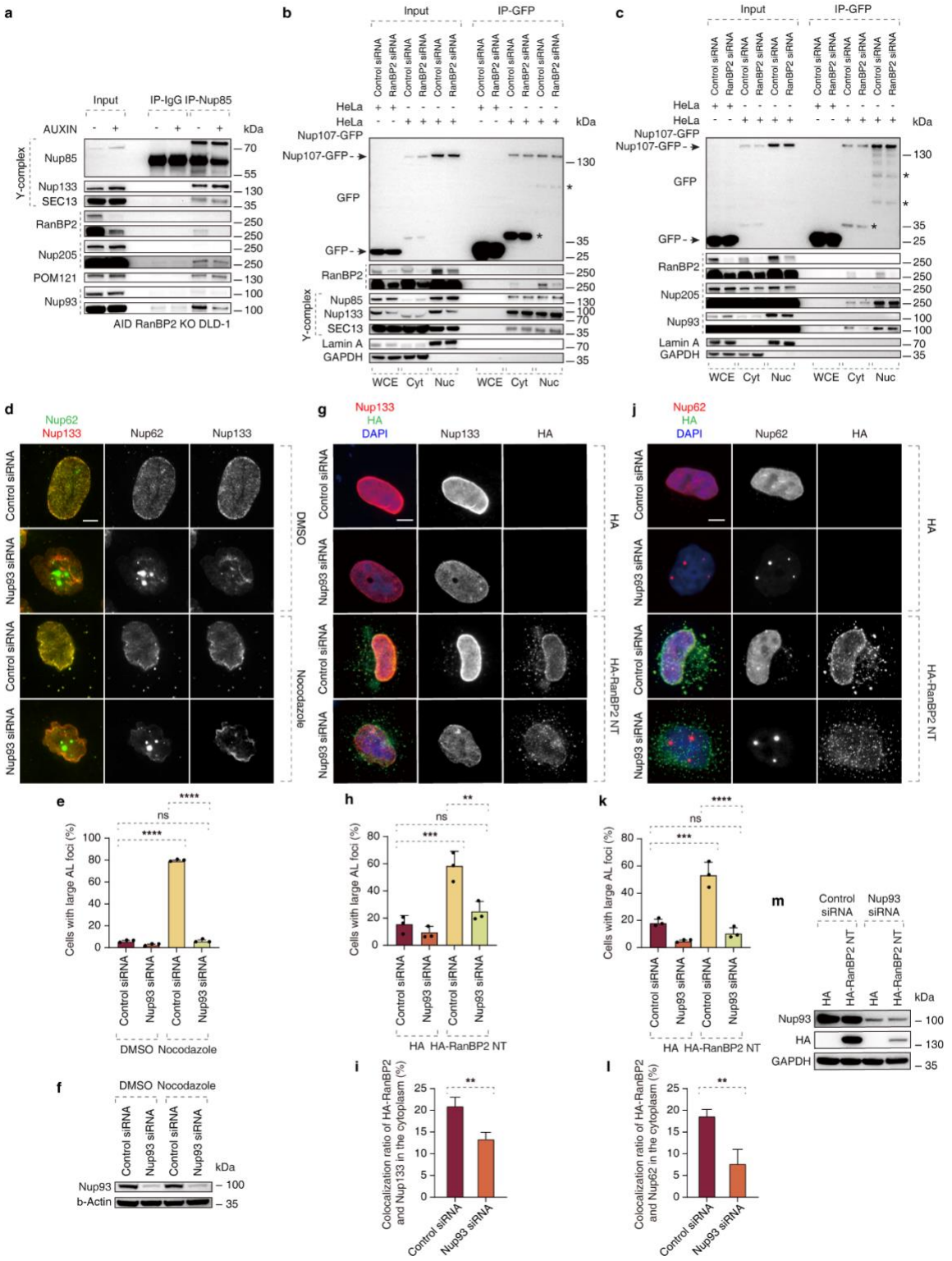

Extended Data Fig. 15. RanBP2 drives the assembly of cytosolic AL-NPCs by promoting the interaction between Nup93 and the Y complex.

2037 a, AID-RanBP2 KO DLD-1 cells were treated with auxin to induce depletion of RanBP2 and
2038 lysates were prepared and immunoprecipitated using Nup85 antibody or IgG and analyzed by
2039 Western blot (at least 3 independent experiments).

2040 b, c, Cytoplasmic or nuclear extracts of Hela cells expressing GFP or 2xZFN-mEGFP-Nup107
2041 were immunoprecipitated using GFP-Trap A beads (GFP-IP) and analyzed by Western blot
2042 (at least 3 independent experiments).

2043 d-f, Representative images of HeLa cells treated with the indicated siRNAs (48h) and
2044 subsequently with nocodazole (10 μM) or DMSO (90 min). Cells were co-labelled with anti-
2045 Nup62 (green) and anti-Nup133 (red) (d) antibodies. The number of cells with large AL foci
2046 was quantified in (e) and at least 1000 cells per condition were analyzed (one-Way ANOVA
2047 test, mean ± SD, ns: not significant, ****P < 0.0001; N = 3). (f) Shows the Western blot analysis
2048 of Nup93 under indicated conditions. Scale bars, 5 μm.

2049 g-m, Representative images of HeLa cells treated with the indicated siRNAs and transfected
2050 with HA or HA-RanBP2-NT fragment. Cells were co-labelled with anti-Nup133 (red), anti-HA
2051 (green) antibodies and DAPI (blue) (g), or co-labelled with anti-Nup62 (red), anti-HA (green)
2052 antibodies and DAPI (blue) (j). Non-AL Nup62 foci, which does not contain Nup133, is
2053 produced in the cell nucleus(g, j). The number of cells with large AL foci was quantified in (h,
2054 k) and the co-localization ratio of HA-RanBP2-NT and Nup62 was quantified in (i, l), and at
2055 least 300 cells per condition were analyzed (unpaired two-tailed t test, or one-Way ANOVA
2056 test, mean ± SD, **P < 0.01; ***P < 0.001; N = 3). Scale bars, 5 μm. (m) Shows the Western
2057 blot analysis of Nup93 and HA-RanBP2-NT under indicated conditions.

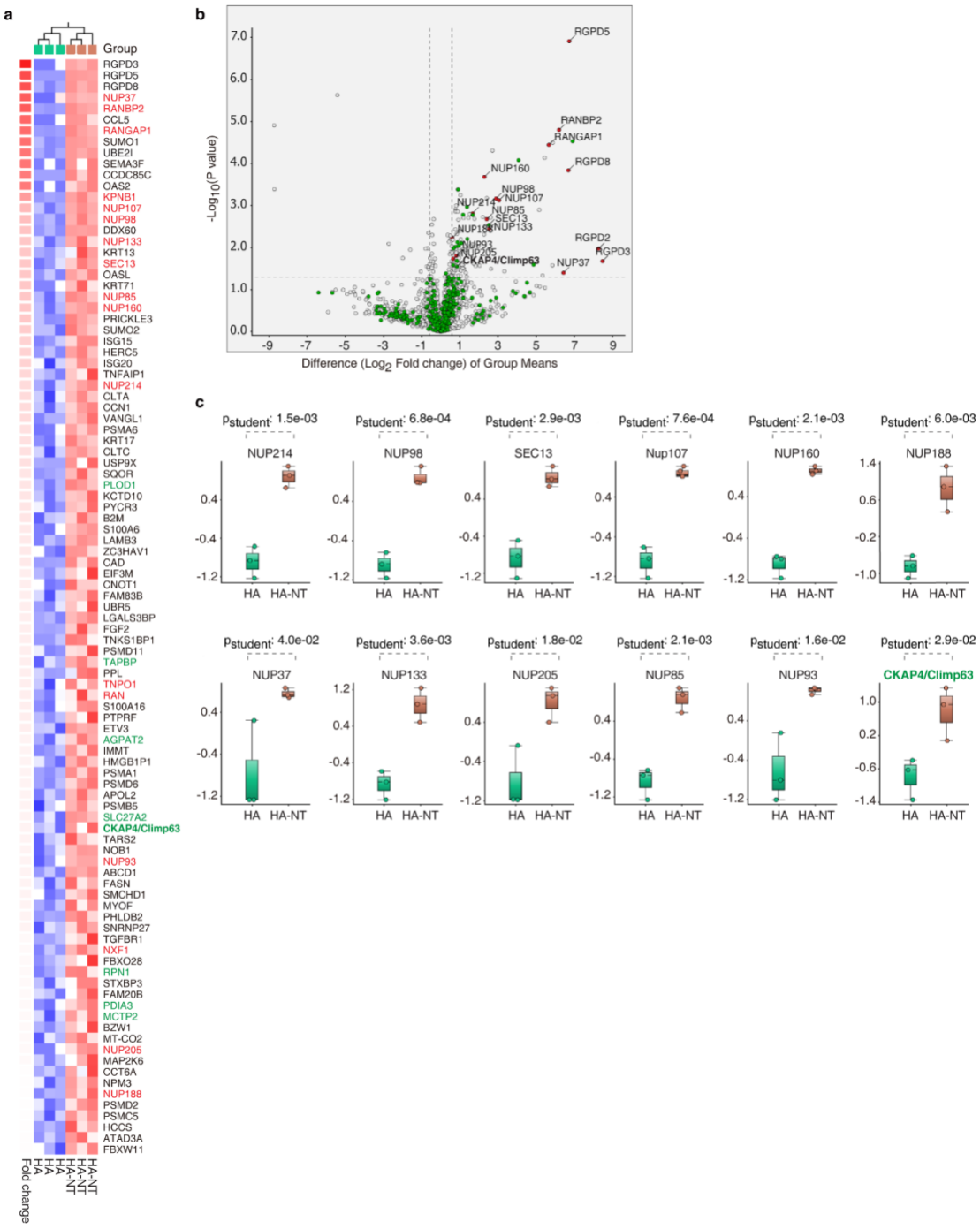

Extended Data Fig. 16. RanBP2-dependent AL interactome.
a-c, Liquid chromatography-mass spectrometry (LC-MS) was used to identify proteins interacting with HA-tagged NT-RanBP2 and the HA-tag as a negative control. A heatmap displays the proteins that showed a change greater than 1.5-fold with a p-value of less than 0.05 between the two groups (a). Volcano plot for the comparison between the two groups (b). The cutoff values fold change >1.5 and FDR < 0.05 were utilized to identify differentially interacting protein. Red represents a group of NPC-related proteins and green depicted ER-related factors. (c) shows the box plots of selected Nups and Climp63 (CKAP4).

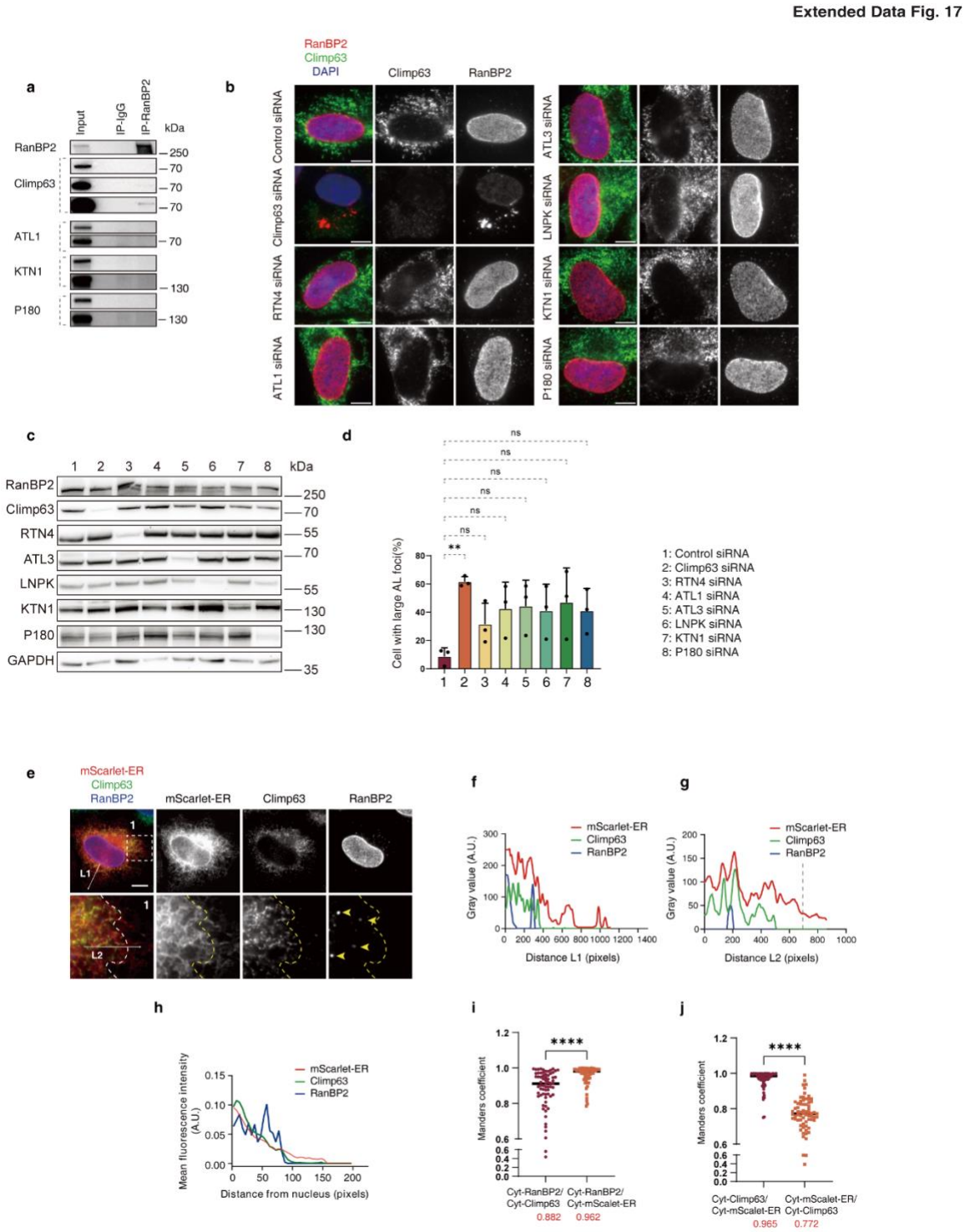

Extended Data Fig. 17. Climp63 facilitates the localization of AL-NPCs to ER sheets. a, Lysates of HeLa cells were immunoprecipitated using RanBP2 antibody or IgG and analyzed by Western blot (at least 3 independent experiments).

2073 b-d, Representative images of MRC5 cells treated with the indicated siRNAs. Cells were co-
2074 labelled with anti-RanBP2 (red), anti-Climp63 (green) antibodies and DAPI (blue) (b). Protein
2075 levels of representative nucleoporins were analyzed by Western blot (c). The number of cells
2076 with large AL foci was quantified in (d) (one-Way ANOVA test, mean ± SD, ns: not significant;
2077 **P < 0.01; N = 3). Scale bars, 5 μm.

2078 e-j, Representative images of HeLa cells expressing ER marker plasmid mScarlet-ER. Cells
2079 were co-labelled with anti-Climp63 (green) and anti-RanBP2 (blue) antibodies (e). The
2080 magnified framed regions are shown in the corresponding numbered panels. The dotted line
2081 represents the boundary between ER sheets labeled by Climp63 and more distal ER tubules.
2082 Intensity profiles along arrows L1 and L2 showing signals from all three fluorescent channels
2083 are shown (f and g). (h) shown the Intensity profiles per distance from the nucleus of three
2084 fluorescent channels. The co-localization of Climp63, mScarlet-ER, and RanBP2 located in
2085 the cytoplasm was measured by in (i, j) (mean ± SD, ****P < 0.0001, unpaired two-tailed t test;
2086 150 cells were counted)

2087

2088

2089